

Copyright  
by  
Barrett C. Worley  
2016

**The Dissertation Committee for Barrett C. Worley certifies that this is the approved  
version of the following dissertation:**

**Investigation of the Mitigation of Charged Impurity and Defect  
Scattering Effects by Polar Molecules on Graphene**

**Committee:**

---

Ananth Dodabalapur, Supervisor

---

Deji Akinwande

---

David Vanden Bout

---

Richard Crooks

---

Graeme Henkelman

**Investigation of the Mitigation of Charged Impurity and Defect  
Scattering Effects by Polar Molecules on Graphene**

**by**

**Barrett C. Worley, B.S.**

**Dissertation**

Presented to the Faculty of the Graduate School of

The University of Texas at Austin

in Partial Fulfillment

of the Requirements

for the Degree of

**Doctor of Philosophy**

**The University of Texas at Austin**

**August 2016**

## **Dedication**

I graciously dedicate this body of work to my incredible parents, inspiring sister, and all my dear friends who have brightened my days during these years in Austin. I also dedicate this work to both one of the finest teachers I have ever known and the man who inspired me to advance my knowledge of chemistry, Mr. Ned Jenne. With triumphant spite, I dedicate this to those fissilingual, morosophic few who sought to darken my days, to see me stumble, and to cast doubt in my heart. Utinam logica falsa tuam philosophiam totam suffodiant.

## Acknowledgements

I would like to express particular gratitude toward my advisor, Dr. Ananth Dodabalapur, for his patience, guidance, and wisdom. Every day spent working with him was a pleasant affirmation that I chose wisely in seeking an engineer advisor. I would also like to acknowledge all Dodabalapur group members whom I had the pleasure of meeting and working alongside: Oleksiy Slobodyan, Kelly Liang, Xin Xu, Dr. Bongjun Kim, Dr. Seonpil Jang, Seohee Kim, Eric Danielson, Michael Rodder, Dr. Davianne Duarte, Dr. Christopher Lombardo, Dr. Leander Schulz, Dr. Tae-Jun Ha, and Dr. Lawrence Dunn. The engineer personality type is truly a well-balanced blend of devoted scientist and practical realist. I would also like to acknowledge Dr. Ryan Haws and Dr. Peter Rossky for their patience and seemingly boundless computational and theoretical chemistry wisdom. Rajarshi Ray also deserves acknowledgement for his inspiring work ethic, positivity, and willingness to help a young scientist advance his career. I would like to acknowledge Karen Shrier, whose fine mentorship and inspirational work ethic went a long way in helping me plan my career ahead. Finally, I acknowledge NSF ECCS Division and NASCENT.

# **Investigation of the Mitigation of Charged Impurity and Defect Scattering Effects by Polar Molecules on Graphene**

Barrett C. Worley, Ph.D.

The University of Texas at Austin, 2016

Supervisor: Ananth Dodabalapur

Graphene is a promising material for use in microelectronics, due to its high mobility, operating frequency, and good stability. These characteristics are governed by charge carrier transport and charged impurity scattering effects, the latter of which are caused by adventitious doping from both the ambient and semiconductor fabrication processes. A variety of chemical interactions between graphene and both its defects and charged impurities influence the electrical properties. This dissertation focuses on the chemical interactions between polar molecules and the impurities and defects on graphene. The monatomic thickness of the graphene monolayer renders interfacial charged impurities located at the graphene/substrate interface susceptible to the dielectric environment surrounding graphene. Our group has shown that the electrical properties of graphene devices are improved upon coating with fluoropolymers or exposure to gas-phase polar organic vapors. These improvements include reduction of the Dirac voltage, increased mobility, and decreased residual carrier density. We attribute these changes to screening by polar molecules of fields induced by charged impurities/defects in or near the active layer. The magnitude of the changes produced in the graphene device parameters scales well with the dipole moment of the delivered vapor molecules. These effects are reversible, a unique advantage of working in the vapor phase. The changes

observed upon polar molecule delivery are analogous to those produced by depositing and annealing fluoropolymer coatings on graphene. We attribute these changes to similar charge screening phenomena. Quantum mechanical modeling showed that polar molecules interacted more strongly with impure or defective graphene than with pristine graphene. Molecular mechanics simulations revealed more insight into how polar molecules interact with two types of charged impurities atop graphene. Polar molecules both displace and electrostatically screen charged impurities to reduce the electrostatic potential profile in the plane of graphene. These computational observations correlate well with our experimental results to support our hypothesis that polar molecules can act to screen charged impurities on or near monolayer graphene. Such screening favorably mitigates charge scattering, improving graphene transistor performance. Our understanding of charged impurity screening methods can further be applied to graphene nanoribbons and other 2D materials.

## Table of Contents

List of Tables .....	x
List of Figures .....	xi
Chapter 1: Introduction .....	1
1.1 Graphene Background .....	2
1.1.1 Electronic Structure .....	3
1.1.2 Transport Physics .....	7
1.1.3 Charged Impurities and Defects .....	9
Chapter 2: Work to Mitigate Charge Scattering .....	14
2.1 Vacuum Sublimated Thin Films .....	14
2.2 Fluoropolymer Coatings .....	16
2.3 SAMs and Other Coatings .....	23
Chapter 3: Vapor-phase Polar Molecules and Charge Scattering on Graphene ...	27
3.1 Introduction .....	27
3.2 Experimental .....	31
3.3 Results and Discussion .....	33
3.4 Summary .....	42
Chapter 4: Computational Modeling of the Interactions of Pristine and Impure/Defective Graphene with Polar Molecules.....	43
4.1 Introduction.....	43
4.2 Quantum Mechanical Studies .....	44
4.3 Molecular Mechanical Studies.....	56
4.3.1 Methods.....	57
4.3.2 Results with Sodium Impurity .....	59
4.3.3 Results with Water Impurity .....	65
4.4 Summary .....	74
Chapter 5: Future Work .....	75
5.1 Experimental .....	75

5.2 Computational.....	77
References.....	79
Vita.....	94

## List of Tables

Table 4.1:	Summary of Leenaerts, <i>et al.</i> DFT results. From Ref. [96].	.....45
Table 4.2:	Summary of Ray DFT Results. From Ref. [133].	.....46

## List of Figures

- Figure 1.1: a) Model of a graphene sheet. b) AFM image of monolayer graphene (red-orange) atop SiO<sub>2</sub> (dark brown), from Ref. [2]. .....3
- Figure 1.2: a) Carbon atom sp<sup>2</sup> orbital hybridization scheme. b) Hybridization of 2p<sub>z</sub> orbitals to form π bonds between two carbon atoms. Adapted from Ref. [68] and Ref. [69]. .....4
- Figure 1.3: Electronic band structure of graphene, showing conduction and valence bands touching at the Dirac points around first Brillouin zone. From Ref. [71]. .....5
- Figure 1.4: Close-up illustration of linear electronic dispersion and electron-hole symmetry of graphene at the K point. From Ref [73]. .....7
- Figure 1.5: Schematic illustration of dielectric layers on either side of a graphene monolayer. The dielectric value of each layer controls the interaction strength. From Ref. [39]. .....10
- Figure 1.6: Conductivity vs gate voltage plots for pristine (black curve) and potassium-doped (color curves) graphene devices at low temperature in vacuum. From Ref. [36]. .....12
- Figure 2.1: Total resistance as a function of gate voltage for a graphene FET before and after capping with F16CuPC, diffusive transport model fitting, and, inset, the basic chemical structure of F16CuPC. From Ref. [23]. ....16

Figure 2.2: a) Reversible effects of a fluoropolymer film on the total resistance as a function of gate voltage for a graphene FET. b) Effects of a fluoropolymer film on the normalized resistance as a function of gate voltage, showing improved on/off ratio. c) Mobility and residual carrier concentration as a function of temperature for a graphene FET. d) Improved mobility and residual carrier concentration as a function of temperature for a fluoropolymer-capped graphene FET. From [43].18

Figure 2.3. Favorable shift in Dirac voltage peak for graphene FETs upon application of a) CYTOP® and b) Teflon-AF fluoropolymers. c) Improvements to on/off ratio for graphene FET upon coating with fluoropolymers. From [44].....20

Figure 2.4. Reversible effects of fluoropolymer in favorably shifting the Dirac voltage for both a) p-doped and b) n-doped graphene FET. c) Improved electrical characteristics of fluoropolymer-capped graphene FET include on/off ratio and Dirac peak voltage. From [26]. .....21

Figure 2.5. a) Mobility values and b) Dirac peak voltages before and after fluoropolymer coating for 30 different graphene FET samples. From [44].....22

Figure 2.6: Drain current ( $I_D$ ) as a function of gate voltage ( $V_G$ ) for graphene FETs on SAM-modified SiO<sub>2</sub>/Si substrates identified by respective end group (CH<sub>3</sub> and NH<sub>2</sub>). SiO<sub>2</sub> label represents untreated SiO<sub>2</sub> surface. From Ref. [95].....24

Figure 2.7: Statistics for graphene devices showing improvements to a) electron mobility, b) hole mobility, c) residual carrier concentration, and d) Dirac voltage upon application of HMDS. From Ref. [49]. .....25

Figure 3.1: Changes in resistivity as a function of time exposed to various polar gases for a graphene sensor device. After initial time in vacuum in region I, the device was exposed to gases in region II. The chamber was evacuated in region III, and the device was annealed in region IV. From Ref. [119]. .....30

Figure 3.2: Resistance as a function of gate voltage for NH<sub>3</sub> exposure–desorption cycles one through three. The solid curves were measured before exposure, the dotted curves were measured after desorption, and the dashed curves were measured after vacuum-degassing at high temperature. From Ref. [120]. .....31

Figure 3.1: a) Schematic cross-section and b) optical image of graphene FET device, showing the channel and introduction of polar vapors. ....32

Figure 3.2: a) Plot of normalized resistance as a function of gate voltage for a graphene FET in ambient under various analyte exposure conditions. Plots of b) Dirac voltage shift, c) electron and hole mobilities, and d) residual carrier concentration as a function of theoretical dipole moment of each polar vapor.....34

Figure 3.3: Plot of normalized resistance as a function of gate voltage for a graphene FET in ambient under exposure to air only, hexane, and acetone vapors. ....35

Figure 3.4: Plot of percent difference in Dirac voltage shifts due to exposure to various vapors, shown as error bars. ....36

Figure 3.5:	a) Plot of normalized resistance as a function of gate voltage showing return of Dirac peak to original position over time after stopping exposure to acetone vapor. Plots of b) Dirac shift magnitude, c) electron and hole mobilities, and d) residual carrier concentration as a function of total elapsed time after acetone vapor flow was stopped.....	38
Figure 3.6:	Plots of resistance as a function of gate voltage for a graphene FET in a) pristine condition and b) with exposure to piperidine. Right side images are SEM images of graphene area, showing darkening upon exposure to piperidine. From Ref. [123]. .....	41
Figure 4.1:	Graphene models used including a) coronene aka GA, b) G70, c) periodic boundary graphene sheet GPBC, d) GA with vacancy aka GAV, and e) GA with Boron dopant, aka GAB. ....	48
Figure 4.2:	GaussView models of CH <sub>3</sub> F on a) GA and b) GAV after optimization. ....	50
Figure 4.3:	GaussView models of NH <sub>3</sub> on a) GA and b) GAB after optimization.	51
Figure 4.4:	Binding energies calculated at PBEPBE/6-31G(d,p) level for various polar molecules and pristine, vacancy defective, and B-doped GA models. ....	52
Figure 4.5:	HOMO/LUMO energy levels for GA, GAV, and GAB. Inset: Respective bandgaps. ....	54
Figure 4.6:	a) HOMO/LUMO energy levels for GA with various polar molecules. b) Plot of the change in HOMO level energy for GA with various polar molecules compared to that of pristine GA alone.....	55
Figure 4.8:	A system containing 50 acetone molecules, a sodium ion impurity, and a graphene sheet.....	57

Figure 4.9: a) A sodium ion atop graphene, with radial electrostatic potential distribution shown by colored circles. b) Electrostatic potential in the plane of the graphene sheet from the sodium ion as a function of distance. c) Potential plots after inclusion of polar molecules in the simulation, showing dramatic reduction of the potential at graphene by polar molecules. ....60

Figure 4.10: Normalized probability distributions of calculated dipole moment values of a) acetone, b) IPA, and c) ethanol molecules in our simulations. 61

Figure 4.11: Potential plot showing the magnitude of potential reduction by acetone molecules (solid line), contribution of displacement mechanism to this potential reduction (dashed line), and contribution of screening mechanism (dot-dot-dashed line). The inset shows the two potential plots of sodium on graphene with (red) and without (black) acetone molecules. b) Percentage contribution of each mechanism to the potential reduction. ....62

Figure 4.12: Snapshots of graphene/sodium ion system a) before and b) after solvation by acetone molecules. ....62

Figure 4.13: Snapshots of graphene/sodium ion system with a) 10, b) 25, and c) 50 acetone molecules. ....63

Figure 4.14: a) Potential plots for sodium both alone and with various numbers of acetone molecules. b) Box plots showing mean displacement (small square) of sodium ion away from graphene as a function of number of acetone molecules, with standard error (larger box boundaries). c) Distributions of values of sodium ion displacement by acetones, revealing formation of a second solvation shell with greater numbers of acetone molecules. ....64

Figure 4.15: a) Electrostatic potential in the plane of the graphene sheet from sodium ion both before and after inclusion of alcohol molecules in the simulation, showing dramatic reduction of the potential at graphene by polar molecules. b) Box plots showing mean displacement (small square) of sodium ion away from graphene as a function of the number of alcohol molecules, with standard error (larger box boundaries). .65

Figure 4.16: Schematics showing potential profile in the plane of the graphene sheet from one water molecule with a) one-leg and b) two-leg water orientations. c) Electrostatic potential as a function of distance on graphene from one-leg and two-leg water orientations. ....66

Figure 4.17: a) A system containing 50 acetone molecules, a water molecule impurity, and a graphene sheet. b) Absolute value of potential from one-leg water orientation both alone and with various polar molecules. c) Change in potential caused by polar molecules for water. ....66

Figure 4.18: Normalized probability distributions of calculated dipole moment values for a) methanol, b) ethanol, and c) IPA molecules. ....67

Figure 4.19: a) Potential plot showing the magnitude of potential reduction for an adsorbed water molecule impurity by acetone molecules (solid line), contribution of displacement mechanism to this potential reduction (dashed line), and contribution of screening mechanism (dot-dot-dashed line). b) Percentage contribution of each mechanism to the potential reduction. ....68

Figure 4.20: a) Potential plots for water alone and with various numbers of acetone molecules. b) Box plots showing mean displacement (small square) of water away from graphene as a function number of acetone molecules, with standard error (larger box boundaries). c) Distributions of values of water displacement by acetone molecules, indicating formation of only one solvation shell around water.....69

Figure 4.21: a) Electrostatic potential in the plane of the graphene sheet from water both alone and with various numbers of ethanol molecules. b) Box plots showing mean displacement (small square) of water away from graphene as a function of the number of ethanol molecules, with standard error (larger box boundaries). c) Distributions of values of water displacement by ethanol molecules, indicating formation of only one solvation shell around water.....70

Figure 4.22: Distributions of values of the angle between water dipole vector and z-axis above graphene sheet in the presence of a) acetone b) ethanol c) IPA molecules. Angle cosine -1: water hydrogens are pointed down toward the graphene. Angle cosine 0: the water hydrogens and oxygen atoms parallel to graphene. Angle cosine +1: hydrogens are pointing away from the graphene.....72

Figure 4.23: a) Absolute value of potential from two-leg water orientation both alone and with various polar molecules. b) Change in potential caused by polar molecules for water. c) Electrostatic potential in the plane of the graphene sheet from water impurity showing the magnitude of potential reduction by acetone molecules (solid line), contribution of displacement mechanism to this potential reduction (dashed line), and contribution of screening mechanism (dot-dot-dashed line). d) Percentage contribution of each mechanism to the potential reduction.....73

## Chapter 1: Introduction

Ever since theoretical descriptions of its band structure in 1947 [1], graphene has captured the attention and imaginations of scientists and engineers due partly to its importance as both a model 2-dimensional (2-D) system [2, 3] and as a model massless Dirac fermion system [4]. Another significant part of graphene's importance lies in its bevy of unique and desirable predicted properties. High mobility, carrier velocity, and operating frequency, atomic-layer thickness, and good stability are among the numerous characteristics which have been studied both theoretically and experimentally after the isolation of graphene by Geim and Novoselov in 2004 [2-12]. These characteristics make graphene very favorable for use in field-effect transistors (FETs) and radio frequency (RF) devices [13-29]. However, much work needs to be done with regard to both scaling up graphene production and integration into existing semiconductor manufacturing processes [28, 30, 31]. Such processing incorporates defects and impurities in graphene, which are charged, resulting in a degradation of electrical characteristics [9, 11, 26, 32-51]. Various groups, including ours, have reported methods that have been successful at mitigating the effects of these impurities and defects [22-27, 43-45, 48, 49, 52-64] in an attempt to restore some of graphene's favorable electrical properties toward their theoretical levels. In-depth study of the chemical processes behind the mitigation of the effects of charged impurities and defects on graphene is important, so that this material may be better employed in microelectronics. Our recent computational studies focused on two of the most prevalent categories of impurities [65]. Additionally, graphene nanoribbons should also be studied both because of their technological promise and because they possess substantially higher concentrations of charged defects and impurities. These studies are also applicable to other 2D materials.

Two-dimensional materials such as graphene are, in many ways, ideal for the study of impurities and defects since these features can be easily accessed. In comparison, the defects/impurities are mostly buried and difficult to access in bulk three-dimensional materials. This aspect of the problem allows a more clear demonstration of the effects of many reversible chemical treatments on graphene device behavior. In turn, demonstration of these effects enables a clearer understanding of impurity/defect-related phenomena. Other groups have also reported on similar experiments.

## **1.1 GRAPHENE BACKGROUND**

Graphene is an atomically-thick, 2-D sheet of carbon atoms which, when stacked with other graphene sheets, comprises the more commonly known material, graphite. Graphite is a crystalline form of carbon which occurs naturally. It has found many uses throughout history as a refractory material in furnaces and high-temperature molds, as a lubricant, and in pencils. The latter two uses exemplify the weak van der Waals bonding between layers of graphene, which allow them to easily slide past and separate from each other. This ease of separation of graphene sheets in graphite lead to the historic exfoliation of few layer, and then monolayer graphene by Geim and Novoselov [2, 3]. Contrary to the bonding between sheets, however, the carbon atoms which make up the honeycomb lattice of monolayer graphene are bonded together in an  $sp^2$  fashion, with average bond lengths of 0.142 nm [1, 6, 31, 66]. Figure 1.1 shows both a model and an AFM image of a monolayer graphene sheet.

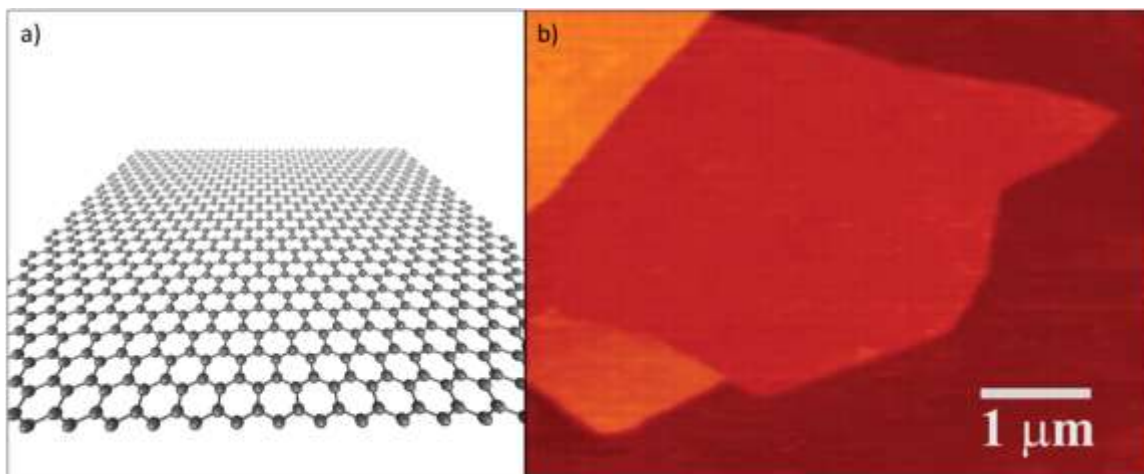


Figure 1.1: a) Model of a graphene sheet. b) AFM image of monolayer graphene (red-orange) atop SiO<sub>2</sub> (dark brown), from Ref. [2].

### 1.1.1 Electronic Structure

In the covalent,  $sp^2$  bonding scheme of graphene, the  $2s$  orbital combines with the  $2p_x$  and  $2p_y$  orbitals of each carbon atom to form three  $sp^2$  hybrid orbitals. The electrons in the planar nodes of these hybrid orbitals allow each carbon atom to directly bond to its three neighbors by strong, in-plane  $\sigma$  bonds, as shown in Figure 1.2a. These bond angles are  $120^\circ$ . The remaining electron in the perpendicular, out-of-plane  $2p_z$  orbitals form a fourth bond between carbon atoms, the  $\pi$  bond [6, 67]. The electrons in  $2p_z$  orbitals of carbon atoms are relatively delocalized, and hybridize together to form bonding  $\pi$  molecular orbitals and antibonding  $\pi^*$  molecular orbitals (Figure 1.2b). The  $\pi$  orbitals are at lower energy, are filled with electrons and form the highest occupied molecular orbital (HOMO). The electron-deficient, higher energy  $\pi^*$  orbitals form the lowest unoccupied molecular orbital (LUMO).

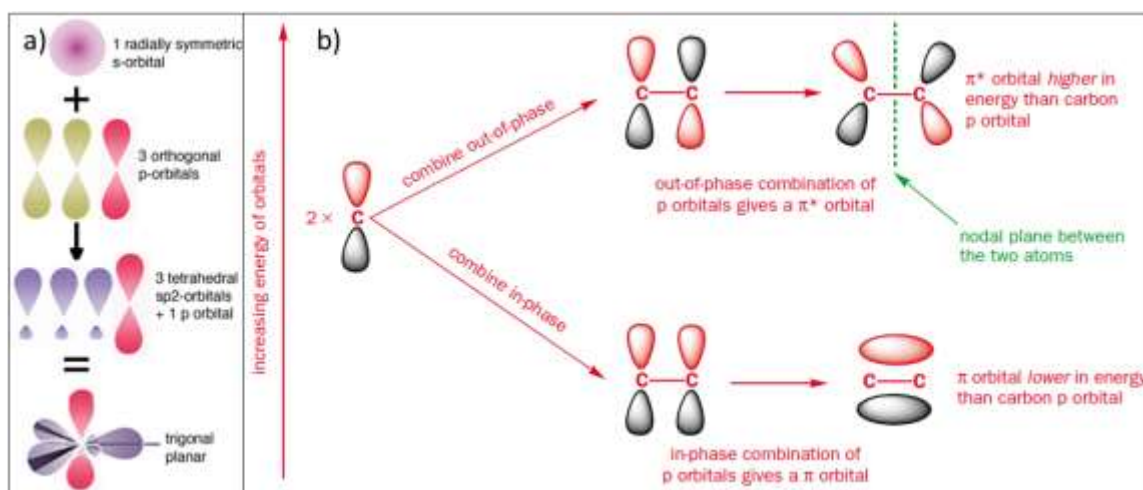


Figure 1.2: a) Carbon atom  $sp^2$  orbital hybridization scheme. b) Hybridization of  $2p_z$  orbitals to form  $\pi$  bonds between two carbon atoms. Adapted from Ref. [68] and Ref. [69].

Popov and others found that graphene is uniquely aromatic when considered in finite molecular sizes. Its  $\pi$ -electrons are pairwise localized to each hexagon ring (63). Zubarev and co-workers expounded on this idea, describing the delocalization of graphene  $\pi$ -electrons as having greater complexity than traditional descriptions of aromaticity, where a finite graphene sheet develops “finite-size domains of perturbed bonds” in response to a perturbation of the  $\pi$ -electron system (64). Nevertheless, graphene’s  $\pi$ -electrons can best be described as delocalized, resulting in excellent electrical conductivity and high mobilities.

As this hybridized molecular orbital model is extended from bonding between adjacent carbon atoms out to a delocalized  $\pi$  cloud of electrons shared amongst the many carbons atoms of a solid material, the HOMO and LUMO nomenclature translates to that of valence and conduction bands, respectively (Figure 1.3). (The author finds that Ishii and coworkers present one of the best and most cohesive general descriptions of electronic structure from the single hydrogen atom up to a molecular solid [70]. Although

their description is not intended to accurately describe a system such as graphene specifically, that paper was a watershed for the author in mentally connecting traditional chemistry models of electronic structure to the band structures common to electrical engineers.)

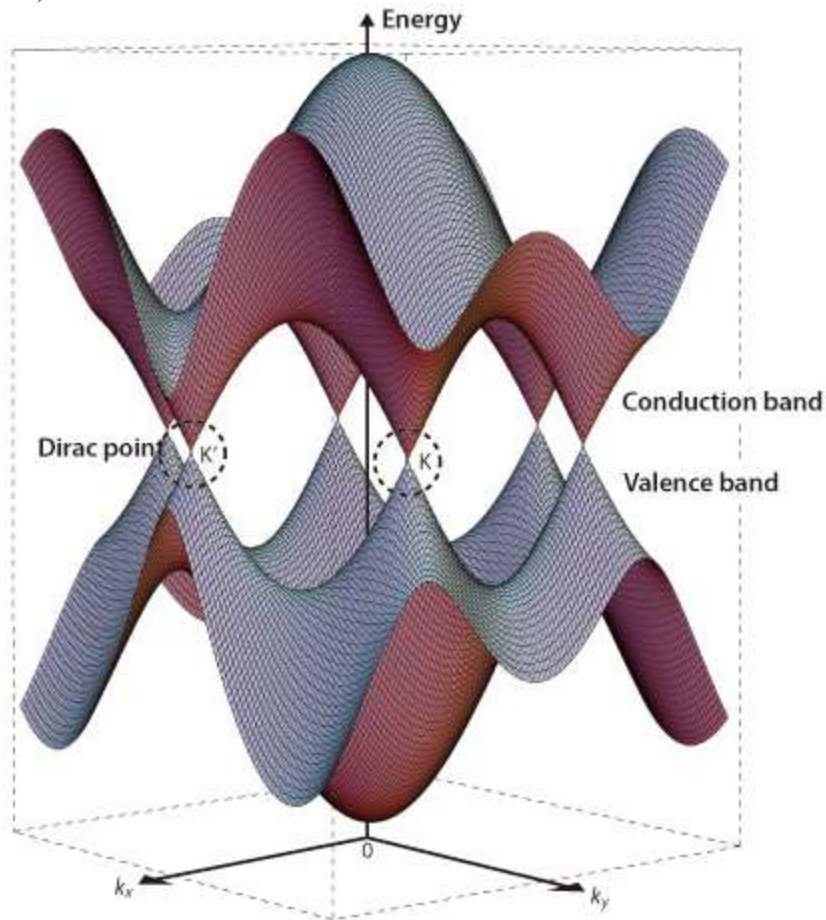


Figure 1.3: Electronic band structure of graphene, showing conduction and valence bands touching at the Dirac points around first Brillouin zone. From Ref. [71].

Electrical conductivity takes place when a perturbation of this system, such as energy input from the surroundings in the form of heat or applied voltage, causes electrons to move from the valence to the conduction band. Where there is energetic

separation between the two bands, this separation is called the bandgap. Materials classified as metals have no bandgap, and are thus highly conductive. Insulators, on the other hand, have such a large bandgap that they are usually not conductive. Materials classified as semiconductors have a bandgap of intermediate size, where addition of energy can promote electrons across the gap to cause conduction. Hence, semiconductor materials are used in transistors and other microelectronic devices, where the additional energy may be supplied in the form of an applied voltage.

Uniquely, the conduction and valence bands of graphene just meet at certain points in reciprocal space, earning graphene the title of zero-gap semiconductor or semi-metal. These points where the bands meet at zero energy are called K- or K'-points, and lie at the corners of the first Brillouin zone in reciprocal space (Figure 1.3) [12, 47, 67, 72]. Being the primitive unit cell of reciprocal space, the Brillouin zone is where the band structure of graphene, aka the electronic dispersion, may be graphed. In contrast to the electron dispersions of other 2-D systems, the band dispersions of graphene on either side of the K- and K'-points, or Dirac points, are linear (Figure 1.4). This figure also illustrates the electron-hole symmetry of graphene.

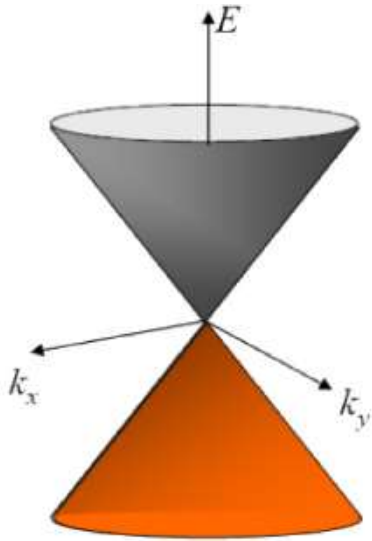


Figure 1.4: Close-up illustration of linear electronic dispersion and electron-hole symmetry of graphene at the K point. From Ref [73].

The linear dependence of electron energy on the wavevector is similar to that of a massless, relativistic particle. Because the electrons traveling through graphene behave as massless quasiparticles best described by the Dirac equation, the charge carriers of graphene, electrons and holes, are called Dirac fermions [4, 74, 75]. The band structure described above is largely responsible for the extraordinary thermal and electrical conductivity of graphene.

### 1.1.2 Transport Physics

The electrical transport properties of graphene are one of its most significant and interesting features. Important properties of graphene physics include its zero-band gap, extraordinarily high charge carrier mobility values, and sub-micrometer ballistic transport [2-4, 6, 67]. As described in the previous section, the band structure of graphene is unique, with conduction and valence bands intersecting at zero energy only at the Dirac points. For this ideal case, the Fermi level ( $E_F$ ) of graphene is found at zero energy as

well, and the density of states disappears [12, 76]. However, experimentally, graphene exhibits a Fermi level shifted from equilibrium and nonzero conductivity at the Dirac point, usually around  $4e^2/h$  [6, 67, 76]. In the context of a graphene field-effect transistor (GFET), this finite minimum conductivity makes the current in the device difficult to completely turn off. Logic devices require that the ratio of *on*-current to *off*-current (*on/off* ratio) be in excess of  $10^4$ - $10^6$  [77]. An alternative use for graphene is in radio frequency (RF) devices, where *on/off* ratio is less important [14, 15, 19, 21, 29, 78-82].

Another extraordinary property of graphene is its high mobility, the speed at which an electron or hole moves through a material under the pull of an electric field, with some theoretical calculations as high as  $10^6 \text{ cm}^2/\text{V}^{-1}\text{s}^{-1}$  [83]. The high mobility of charge carriers is due to their having zero effective mass. Experiments at room temperature with suspended graphene have achieved a mobility value of  $200,000 \text{ cm}^2/\text{V}^{-1}\text{s}^{-1}$  with carrier concentration of  $2 \times 10^{11} \text{ cm}^{-2}$  [10], while more recent experiments using hexagonal boron nitride (hBN) substrates have claimed a record hole mobility of  $350,000 \text{ cm}^2/\text{V}^{-1}\text{s}^{-1}$  below room temperature [84]. However, in most as-fabricated graphene devices, the mobility is limited by scattering sources, such as surface phonons, charged impurities, and defects. Electron-hole puddles have also been cited as the cause of lower than expected mobility values for graphene samples. Yet, it is unlikely that the puddles are the dominant, and certainly not the only source of charge carrier scattering in graphene samples (68). Our group has focused on charged impurities and defects as important sources of charged scattering.

### 1.1.3 Charged Impurities and Defects

Many of the important and favorable qualities of graphene transport physics were discussed above. However, given the vigorous and ongoing debates over exact details of graphene transport in theoretical versus experimental results, low temperature versus high temperature, suspended versus on-substrate, and other specific cases, it is important to qualify the particular situation in which graphene will be described here. The focus here will be on experimental graphene that was produced via a chemical vapor deposition (CVD) growth process on copper substrate [64, 85]. The graphene is transferred onto SiO<sub>2</sub>/Si substrates using a wet transfer process [43, 44, 64, 85-88]. This method is one of the most commonly used in the fabrication of graphene based FET devices, and has seen much improvement in recent years [64, 89-91]. The types of devices discussed here have exposed graphene, which is open to access by capping layers or vapors. Thus, contamination of the sample by charged impurities and defects such as adsorbed or trapped oxygen and water, residue from the transfer, or trapped ions and substrate defects are significant contributions to disorder [32, 37, 41, 53, 55, 57, 63, 92-101]. Specifically, scattering of charge carriers is an important mechanism by which charged impurities and defects degrade electronic transport in graphene.

The fine structure constant  $\alpha$ , as described by Das Sarma and co-workers, provides a good reference point from which to understand how it might be possible to reduce charge scattering in graphene [39]. Figure 1.5 illustrates how increasing the dielectric constant values ( $\kappa_x$ ) for the environments above and below graphene can reduce  $\alpha$ .

$$\alpha = \frac{2e^2}{\hbar v_F (\kappa_1 + \kappa_2)}$$

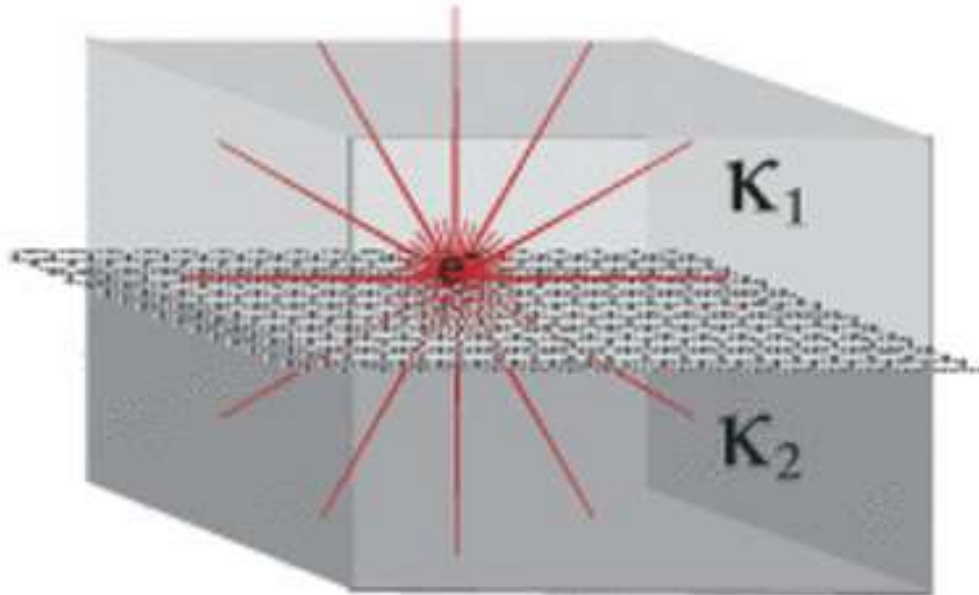


Figure 1.5: Schematic illustration of dielectric layers on either side of a graphene monolayer. The dielectric value of each layer controls the interaction strength. From Ref. [39].

Das Sarma and co-workers reported that a smaller  $\alpha$  value results in increased Coulombic scattering- limited mobility. Their work, and similar work by other groups, offers insight into how to improve graphene's electrical properties. Polar molecules can help in two possible ways. The first way involves partial neutralization of charged impurities by polar molecules, and the second way involves the alignment of the polar molecules into a dipole layer, which increases the  $\kappa$  around graphene, decreasing  $\alpha$  to produce the improvements mentioned above [39, 102, 103]. Such alignment is driven by

the total energy of the system which would be minimized in this configuration, and is aided by the polarizability of graphene [104-107].

While a variety of other scattering sources, such as phonons and surface corrugations, do affect the conductivity ( $\sigma$ ) of graphene, scattering by charged impurities ( $CI$ ) affects the conductivity, dependent on the charge carrier density ( $n$ ), according to the Equation 1 described by Fuhrer and co-workers [36, 37].

$$\sigma_{CI}(n) = C_{CI} e \left| \frac{n}{n_{imp}} \right| \quad [1]$$

$C_{CI}$  is a constant of value  $5 \times 10^{15} \text{ V}^{-1} \text{ s}^{-1}$ . Figure 1.6 shows their experimental results from doping graphene FETs with potassium ions. As the impurity doping concentration increased, the mobility values decreased. Their results also supported theoretical predictions that the conductivity has a linear relation to gate voltage when charged impurity scattering is the dominant scattering mechanism.

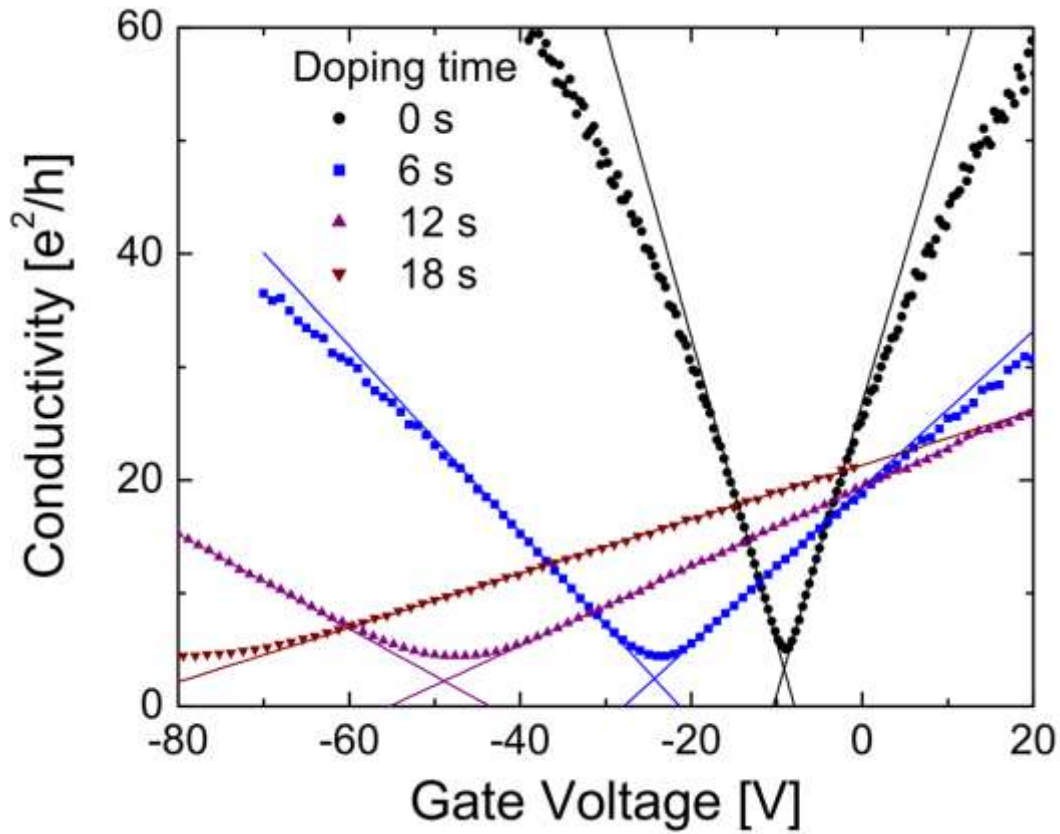


Figure 1.6: Conductivity vs gate voltage plots for pristine (black curve) and potassium-doped (color curves) graphene devices at low temperature in vacuum. From Ref. [36].

Charge carriers in graphene undergo ballistic transport until deflected either by charged impurities (long-range scattering) or by one another (short-range scattering). More specifically, charged impurities and defects act to scatter charge carriers in graphene by influencing the two mechanisms of Coulombic, long-range scattering and short-range scattering. Coulombic, long-range scattering shortens the mean free path for charge carriers, and this is observed in lower-than-predicted mobility values. Scattering by charged impurities and defects may also cause shifts in the Dirac point (charge-neutral point) voltage of measured current versus gate voltage curves ( $I_d$ - $V_g$ ) [32, 34, 45, 108-

110]. Dirac voltage shifts are problematic both in that they represent non-ideal behavior of graphene and in that a device with a significantly shifted Dirac point voltage would be more difficult or less efficient to operate as a normal transistor. Hysteresis in such  $I_d$ - $V_g$  curves is another observable, unfavorable electrical characteristic that indicates charge scattering or changes in charge carrier density due to charged impurities in the form of adsorbed water or other polar molecules [32, 41, 94, 100].

## Chapter 2: Work to Mitigate Charge Scattering

Having recognized the challenges which graphene's susceptibility to charged impurities and defects presented to the future of graphene microelectronics, work on new methods of improving key performance metrics in graphene devices is of great importance. Such methods would need to interface with existing microelectronics industry processes and equipment. Covalent modification chemistry does not adequately meet this condition, and such functionalization may suppress graphene charge carrier mobility by interrupting the  $sp^2$  hybridized bond structure of graphene [55].

### 2.1 VACUUM SUBLIMATED THIN FILMS

Instead, Ha *et al.* used vacuum sublimation to deposit semiconducting organic capping layers onto a bottom-gate, graphene FET [23]. Thin films of both  $\alpha$ -sexithiophene ( $\alpha$ -6T) and hexadecafluorocopperphthalocyanine ( $F_{16}CuPC$ ) were employed as capping layers atop the graphene. The inset of Figure 2.1 shows the basic chemical structure of  $F_{16}CuPC$ . While both organic materials improved the measured electrical characteristics of the graphene device in air, the authors noted that the fluorinated organic material,  $F_{16}CuPC$ , had particularly favorable effects. The authors observed significant improvements to the on/off current ratio, Dirac voltage point, and field-effect mobility of the graphene device treated with the  $F_{16}CuPC$ . These improvements to electrical characteristics stand in stark contrast with other prior attempts to place additional layers atop a graphene device. Figure 2.1 shows the results of testing a graphene FET with  $F_{16}CuPC$  capping layer in air. The fluorinated organic material significantly improved the on/off current ratio, a key metric for transistor performance in terms of high speed and low leakage current. The Dirac peak voltage, where resistance is

a maximum and conductivity is a minimum, is also shown in Figure 2.1 as significantly positive when measured on the initial bare graphene device. This indicates some residual doping of the graphene by impurities and defects. However, upon capping with  $F_{16}CuPC$ , the Dirac peak shifts back toward the ideal graphene Dirac voltage of zero gate voltage. Ideally, the Dirac voltage should be at zero volts and the minimum conductivity (at the Dirac point) should be as small as possible. The diffusive transport model used to extract values for both field-effect mobility and residual carrier density at the minimum conductivity point is also plotted in Figure 2.1, and gives a good fit to the experimental data. In addition to the improvements to electrical characteristics listed above, the authors also calculated that  $F_{16}CuPC$  both significantly increased the mobility and reduced the residual carrier density at the minimum conductivity point.

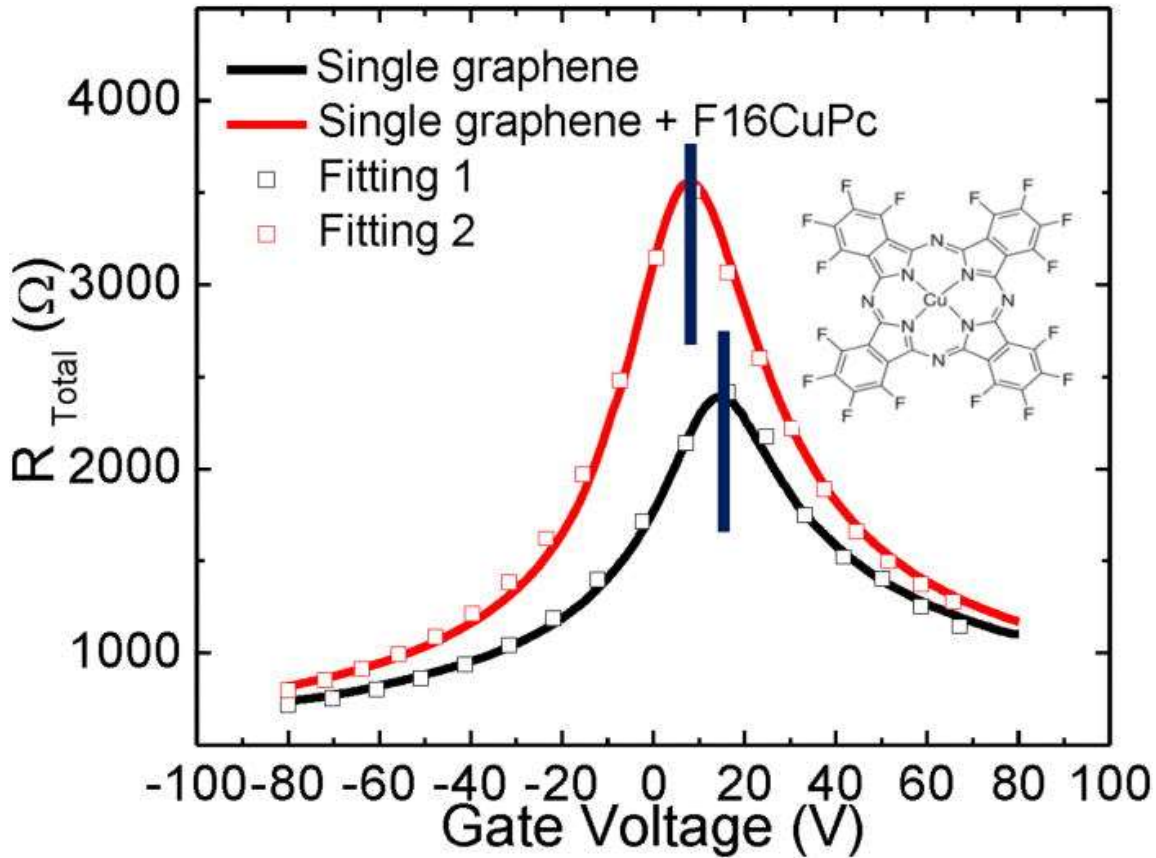


Figure 2.1: Total resistance as a function of gate voltage for a graphene FET before and after capping with F16CuPC, diffusive transport model fitting, and, inset, the basic chemical structure of F16CuPC. From Ref. [23].

## 2.2 FLUOROPOLYMER COATINGS

Ha and co-workers' work with F<sub>16</sub>CuPC led to further study the effect of other fluorinated materials on graphene, as described in work published in References [26, 43, 44]. The authors chose to employ the fluoropolymers CYTOP<sup>®</sup> and Teflon-AF. The fluoropolymers were deposited as a thin film directly on top of the graphene layer of a FET via spin-coating methods, with subsequent annealing. Figure 2.2 shows the effect of a spin-coated thin film of the CYTOP<sup>®</sup> on the transfer characteristics of a graphene FET, with improvements to electrical characteristics similar to those previously observed with a capping layer of the fluorinated organic molecule F<sub>16</sub>CuPC. The CYTOP<sup>®</sup>

fluoropolymer capping layer significantly reduced the off-state current at the Dirac voltage point (red curve), seen as a large increase in maximum measured resistance compared to that of the bare graphene device (black curve). Remarkably, after removal of the CYTOP<sup>®</sup> layer, the measured characteristics of the graphene device appear to return toward their initial values (blue curve, Figure 2.2a). In the experiments, the authors did not achieve complete removal of the fluoropolymer from the graphene, which may account for the incomplete reversion of the characteristics. More importantly, this degradative reversion in electrical characteristics indicates that the impact of the CYTOP<sup>®</sup> layer upon graphene is caused by a reversible interaction. The *on/off* ratio is critical for graphene FET operation, and significant improvement in the ratio is shown more clearly as a sharpening of the graphene+ CYTOP<sup>®</sup> peak versus the peak for graphene alone in Figure 2.2b, a plot of normalized resistance versus gate voltage. Additionally, the improvements caused by CYTOP<sup>®</sup> are much better than those caused by capping with pentacene, and sharply contrast the degradative effects of a SiO<sub>2</sub> capping layer.

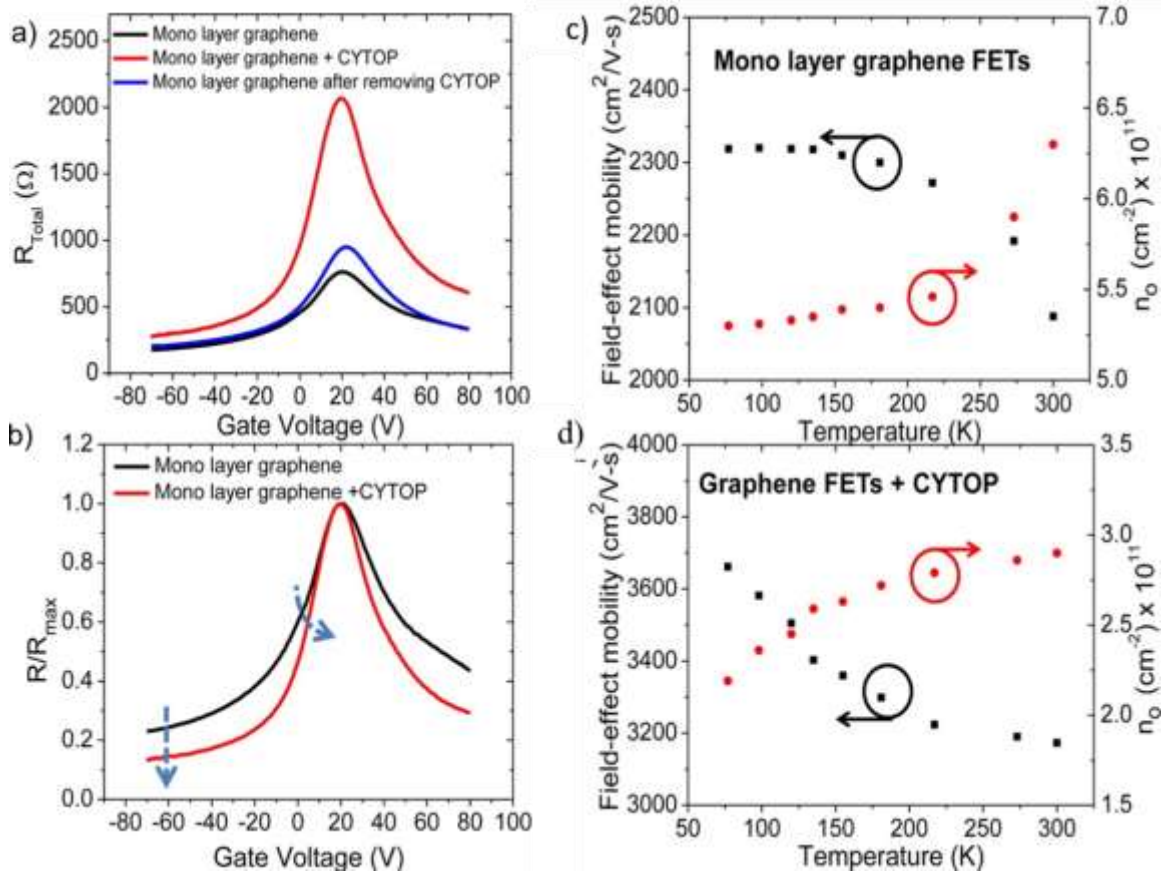


Figure 2.2: a) Reversible effects of a fluoropolymer film on the total resistance as a function of gate voltage for a graphene FET. b) Effects of a fluoropolymer film on the normalized resistance as a function of gate voltage, showing improved on/off ratio. c) Mobility and residual carrier concentration as a function of temperature for a graphene FET. d) Improved mobility and residual carrier concentration as a function of temperature for a fluoropolymer-capped graphene FET. From [43].

CYTOP® also caused great improvement in graphene’s temperature-dependent charge carrier mobility. In comparing Figure 2.2d (CYTOP®-coated graphene FET) with Figure 2.2c (bare graphene FET), note that the scattering-limited mobility with CYTOP®-coating is higher than that of the bare graphene device at all measured points. Further, the mobility in Figure 2.2d is shown to continuously increase as temperature decreases, instead of plateauing as in Figure 2.2c. Concurrent with improvements to

mobility, CYTOP® caused significant temperature-dependent reduction in residual carrier concentration, also shown in Figures 2.2c and 2.2d. Ha *et al.* attributed these improvements to a reduction in short range scattering, which lowers the value of the residual carrier concentration [39]. Residual carrier concentration is a metric related to the concentration of impurities in or around the graphene. Additionally, the authors observed that increased annealing temperatures gave greater impact of the fluoropolymer to device characteristics, and they attributed that effect to a reorganization of the C-F bond dipoles atop the graphene. Finally, the apparent return of the pre-fluoropolymer electrical characteristics of graphene further indicate that the actions of the fluoropolymer upon graphene are of a noncovalent, reversible nature [43].

Continuing the work of employing polar fluoropolymers to improve graphene device electrical characteristics, Ha *et al.* observed the significant favorable shift in the Dirac voltage peak for graphene FET devices upon capping and annealing with CYTOP® and Teflon-AF fluoropolymer layers shown in Figures 2.3a and 2.3b. Before fluoropolymer deposition, the bare graphene devices exhibited a very positively-shifted Dirac voltage peak position, due to doping effects from charged impurities and defects which incorporate in and around the graphene from both the wet transfer process and the substrate. Asymmetry between electron and hole transport is also evident. Upon coating with CYTOP® and gradual annealing in nitrogen atmosphere from 30°C to 180°C, or coating with Teflon-AF and gradual annealing in nitrogen atmosphere from 30°C to 300°C, the authors observed dramatic, favorable shifts in the Dirac voltage peak position from the very positively-shifted initial state toward nearly zero gate voltage. Having now observed such movement of the Dirac voltage peak by several different fluorinated organic molecule/polymer capping layers, the authors attributed the favorable Dirac voltage shifts to mitigation by the polar C-F bonds of the molecules/polymers of the

Coulombic charge scattering effects of charged impurities and defects around graphene. Electron and hole transport became more symmetric. Again, they reported improvement in mobility concurrent with decrease in residual carrier concentration, and Figure 2.3c shows significant improvement to the *on/off* ratio for fluoropolymer-coated graphene FETs.

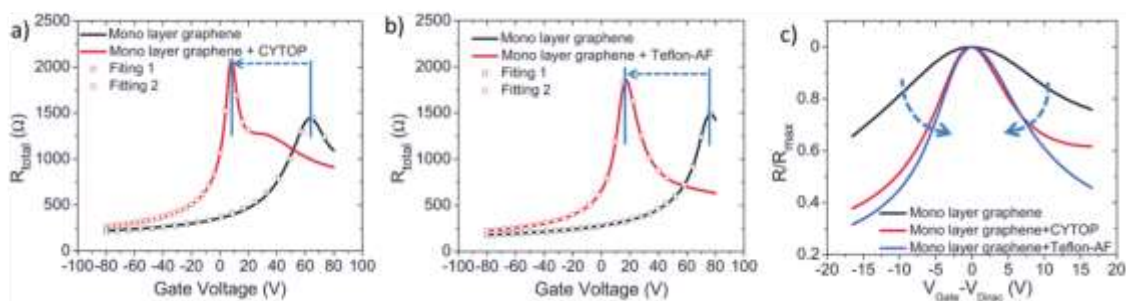


Figure 2.3. Favorable shift in Dirac voltage peak for graphene FETs upon application of a) CYTOP® and b) Teflon-AF fluoropolymers. c) Improvements to on/off ratio for graphene FET upon coating with fluoropolymers. From [44].

In further studies with fluoropolymers on graphene devices, Ha *et al.* observed changes to a greater variety of devices that indicate the favorable effects of polar, C-F bonded materials are of a widely applicable nature [26]. As shown in Figures 2.4a and 2.4b, treatment with fluoropolymers can significantly improve the Dirac peak of a graphene FET, regardless of p- or n-doping from charged impurities and defects (red curves). The authors attributed the adaptability of the fluoropolymer's interactions with either p-type or n-type charged impurities and defects to self-organization of the dipolar C-F bonds upon heat treatment (annealing). Again, the improvements to the device electrical characteristics exhibit reversible behavior upon removal of the fluoropolymer (blue curves), indicating a noncovalent, reversible interaction. They also reported the highest *on/off* ratio at room temperature for CVD-grown graphene at the time, indicated

in Figure 2.4c. The greatest improvements to electrical characteristics were observed for devices where the graphene was capped on both sides by fluoropolymer further. This observation supports the assessment that charged impurities and surface defects of the substrate are significant causes of scattering for charge carriers in graphene. The results also support the assessment that the polar nature of fluoropolymers mitigates that scattering to improve charge transport in graphene, which manifests as measurable improvements to electrical characteristics. Additionally, the authors observed that the hydrophobic nature of the fluoropolymers used in the experiments serves to protect the capped graphene devices from water, another common contaminant known to frequently degrade device characteristics [26, 32, 41, 94, 100].

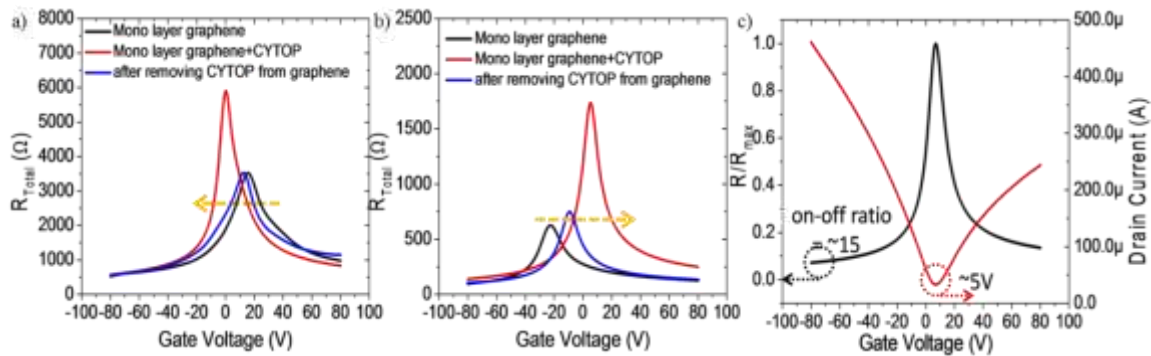


Figure 2.4. Reversible effects of fluoropolymer in favorably shifting the Dirac voltage for both a) p-doped and b) n-doped graphene FET. c) Improved electrical characteristics of fluoropolymer-capped graphene FET include on/off ratio and Dirac peak voltage. From [26].

It is also important to note that, as shown in Figure 2.5, Ha *et al.* have observed these improvements for 30 different graphene FET samples [44]. While these devices were fabricated at different times in different batches, they all exhibit improved mobility and favorable Dirac voltage shifts toward zero gate voltage upon capping with the fluoropolymer CYTOP<sup>®</sup>. Such statistical analysis is important because measured results

can quantitatively vary from device to device, so it is best to check for repeatable results over a large number of devices. Figure 2.5 shows that, while the quantitative results do vary from sample to sample, the qualitative effects of the fluoropolymer on the graphene FETs' electrical characteristics are uniform.

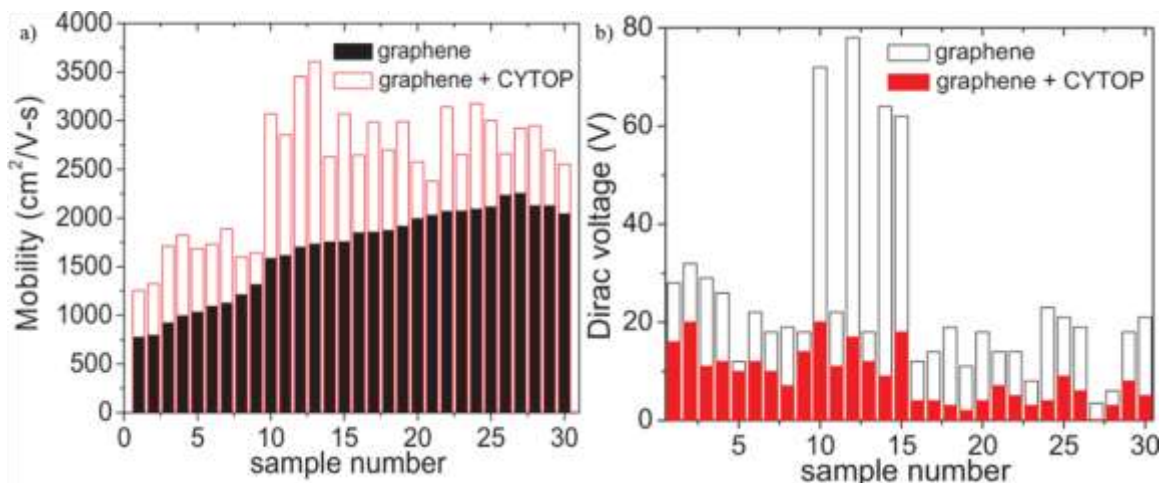


Figure 2.5. a) Mobility values and b) Dirac peak voltages before and after fluoropolymer coating for 30 different graphene FET samples. From [44].

In addition to the work on graphene, Ha *et al.* also observed improvements to other 2-D materials by treatment with fluoropolymers, such as increased drain current, mobility, and transconductance in reduced graphene oxide, and improved *on/off* current ratio in  $\text{MoS}_2$  [26]. Kim and co-workers reported significantly increased air-stability over time with black phosphorous [111]. These results with fluoropolymers and a variety of 2-D materials hold great promise for this method to be both practical and impactful in developing the full potential of graphene and other 2-D materials in the microelectronics industry.

### 2.3 SAMs AND OTHER COATINGS

Other groups have achieved improvements to graphene device characteristics via coating methods such as treatment with various self-assembled monolayers (SAMs). Park, *et al.* fabricated graphene FETs on SiO<sub>2</sub>/Si substrates, with and without SAM layers between the graphene and SiO<sub>2</sub> [95]. They used two types of SAMs:  $\gamma$ -aminopropyltriethoxysilane (APS), having -NH<sub>2</sub> end groups, and octadecyltrichlorosilane (OTS), with -CH<sub>3</sub> end groups. Figure 2.6 shows the transfer characteristics of graphene FETs measured with graphene on bare SiO<sub>2</sub>, where the position of the Dirac point voltage (point of minimum conductivity) indicates p-doping from charged impurities and defects at the graphene/SiO<sub>2</sub> interface. In contrast, placing an OTS layer between the graphene and substrate resulted in a significant negative shift of the Dirac peak position. This is indicative of reduced p-doping, which can be attributed to separation of the graphene from the p-doping SiO<sub>2</sub> surface impurities and defects. Further, the authors mention the lack of electronic interaction between graphene and the -CH<sub>3</sub> end groups. Finally, the APS layer separating graphene and the substrate caused a dramatic negative shift of the Dirac point position, due to a combination of separation from p-doping impurities on the SiO<sub>2</sub> surface and the n-doping behavior of -NH<sub>2</sub> end groups. These results are comparable to our groups' results with fluoropolymer coatings on graphene FETs.

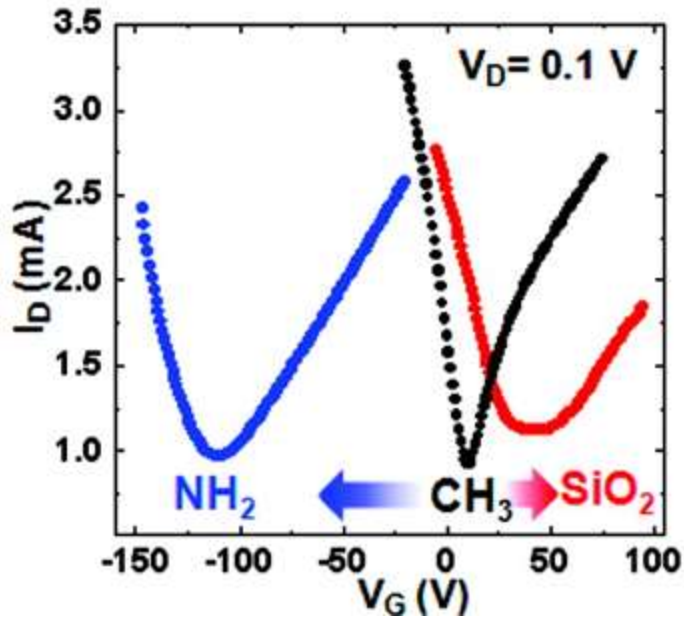


Figure 2.6: Drain current ( $I_D$ ) as a function of gate voltage ( $V_G$ ) for graphene FETs on SAM-modified SiO<sub>2</sub>/Si substrates identified by respective end group (CH<sub>3</sub> and NH<sub>2</sub>). SiO<sub>2</sub> label represents untreated SiO<sub>2</sub> surface. From Ref. [95].

Similarly, Akinwande and co-workers coated both graphene alone and graphene and underlying substrate with HMDS [49]. Upon comparison with graphene-on-SiO<sub>2</sub> device characteristics, they found significant improvement to graphene device mobility values, reduction in residual carrier concentration, and favorable shifts in Dirac voltage peak (Figure 2.7). The authors also attributed the observed improvements to the polar nature of the HMDS molecules acting to both enhance the dielectric screening and mitigation of charged impurities via a reduction of the dimensionless fine structure constant. It is also important to note that the hydrophobic methyl groups of the HMDS molecules which contact the graphene separate or block the graphene from any adsorbed impurities on the substrate or in the air.

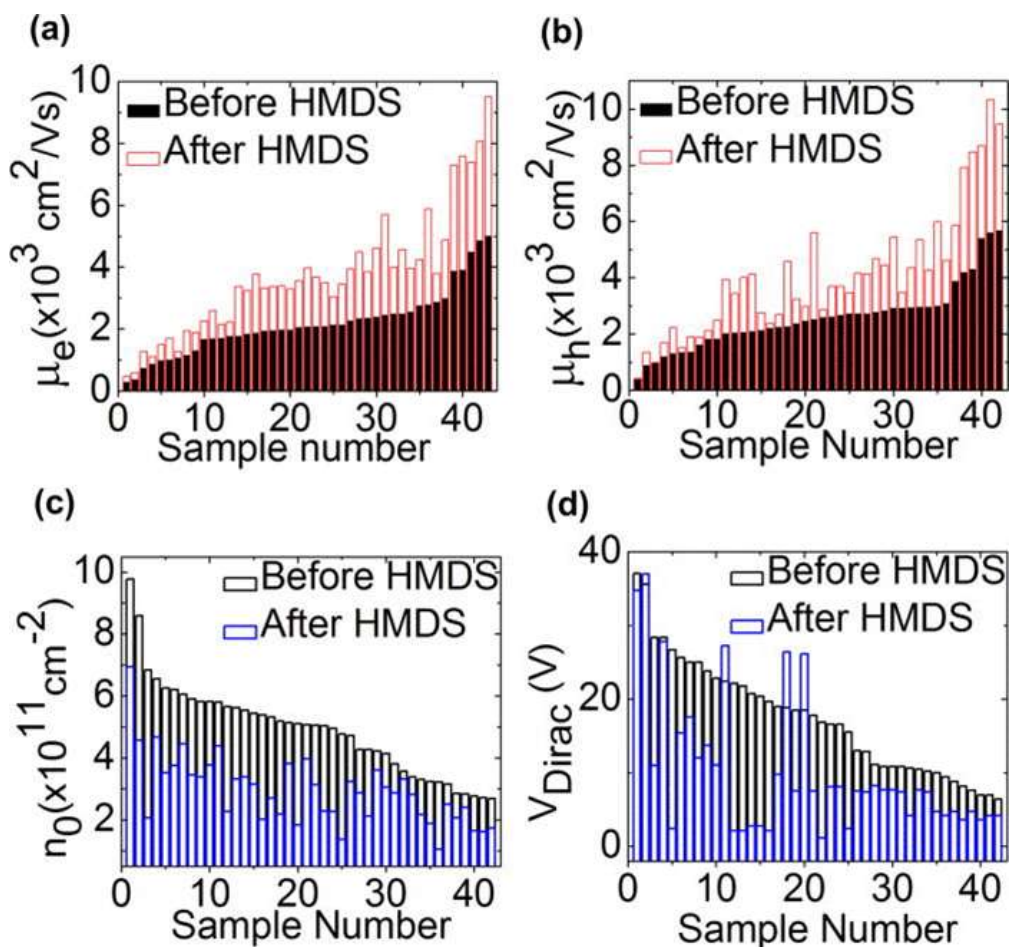


Figure 2.7: Statistics for graphene devices showing improvements to a) electron mobility, b) hole mobility, c) residual carrier concentration, and d) Dirac voltage upon application of HMDS. From Ref. [49].

In their studies on alkyl phosphonic acid-based self-assembled monolayers, Cernetic and co-workers reported improvement to graphene device mobility, favorable shifts in Dirac voltage peak, and reduction in hysteresis [57]. They partly attributed these improvements to reduction of defects/charge trap states in the layer immediately underneath graphene. Many other groups using SAMs report similar improvement to graphene device electrical characteristics, where the dipole moments of a variety of SAM molecules cause shifts in the Dirac voltage peak position and improve the mobility

relative to those of graphene-on-SiO<sub>2</sub> devices [53, 55, 58, 61, 62, 112] All of these groups also acknowledge the significant detriment to graphene transport caused by scattering from charged impurities and defects at the substrate.

## Chapter 3: Vapor-phase Polar Molecules and Charge Scattering on Graphene

### 3.1 INTRODUCTION

Graphene, a 2-D hexagonal lattice of sp<sup>2</sup>-bonded carbon atoms, is an attractive material for microelectronics applications, given such favorable electrical characteristics as high mobility, operating frequency and good stability [6, 10, 12, 19, 24, 30, 46, 85, 86, 113-115]. The characteristics are governed by graphene transport physics, of which electron-hole transport symmetry, Dirac point voltage, and charged impurity effects are key factors [10, 36, 39, 43, 44, 46, 47, 113].

Theoretical calculations predict extremely high carrier mobility for pristine, intrinsic graphene, which is, when ungated, free of doping. Graphene has no band gap, and, instead, the bands meet at the charge neutral Dirac point [47, 72]. In reality, adventitious doping is very difficult to avoid during normal semiconductor fabrication processes [4, 47]. Generally, experimentally realized graphene is deemed extrinsic, having some amount of free carriers induced by doping from charged impurities and defects, which are present either at the graphene/substrate interfaces or within close proximity to the interfaces [4, 28, 33, 42, 47, 113]. Such impurities can include, among others, adsorbed water or oxygen, residues left over from the wet transfer of graphene to the substrate, ions trapped between the graphene and substrate, and dangling bonds from the SiO<sub>2</sub>. Impurities affect the electronic transport of graphene by the two principal mechanisms: short-range scattering and Coulombic, long-range scattering [11, 39, 47, 72, 74]. It is widely agreed that long-range scattering by impurities plays the dominant role in graphene transport for most experimental conditions, given that many as-fabricated samples possess a high concentration of charged impurities [10, 28, 33, 40, 42-44, 46, 47, 116]. Thus, it is imperative for the advancement of graphene microelectronics technology

that methods be developed for mitigating the charge scattering effects of any possible charged impurities and defects.

Previous work has shown that the dielectric environment surrounding the graphene is an important determinant of the transport properties. The prior work included solid dielectrics and liquid dielectrics, which were both shown to have a major influence on transport properties [39, 40, 43, 44, 116]. In working towards improvement of graphene electronics by mitigating charged impurity effects, our group has shown that the use of a fluoropolymer thin film atop a graphene monolayer favorably altered the electrical properties of the graphene field-effect transistor (FET), enhancing mobility while reducing both carrier concentration and the magnitude of the Dirac voltage [43, 44]. It was hypothesized that a possible cause of such electrical property improvements is the neutralization or screening of charged impurities and defects by electrostatic- or van Der Waals-type interaction with the dipoles of fluoropolymer C-F bonds. Upon observing that higher annealing temperatures lead to both better molecular ordering in thin films and improved electrical properties, it was also suggested that the self-organization of the fluoropolymer C-F bonds atop the graphene alters the local dielectric environment [43, 64, 117, 118]. It is expected that modification of the dielectric environment adjacent to graphene will alter the dimensionless coupling constant (also known as the effective fine-structure constant),  $a$ , of the graphene system [36, 39]. While the discussion by Newaz, *et. al.* of various dielectrics surrounding graphene included various effects unique to the liquid phase, including the formation of an electrical double layer and the ever-present charged ions in solution, we emphasize that our experiments do not involve device measurements in liquid media [40]. Indeed, in contrast to liquid-phase experiments, our group was able to exert greater control over the extent to which the polar molecules and bonds of the fluoropolymer thin films organize atop the graphene via annealing

experiments. Both the charged impurity neutralization by molecular dipoles and dielectric environment modification aspects of our hypothesis directly influence the aforementioned electrical characteristics of a graphene FET, and will be discussed in this work. However, the chemical and structural complexities of the fluoropolymer film/graphene system, which include variables such as the degree and orientation of polarization interactions between graphene and the C-F fluoropolymer bonds, complicate the precise identification of the physical phenomena involved in the observed electrical improvements. Polar small molecules such as ethanol, with well-defined dipole moments, are excellent model systems to help study the effect of such materials on graphene properties. The experimental advantages of using vapor-phase polar molecules as opposed to applying thin films of polar molecules/polymers include easy application, easier removal in the form of simple evaporation in ambient, and in situ reorientation of the vapor molecules' dipoles around charged impurities and defects (as opposed to annealing of thin films). As early as 2007, Schedin and co-workers were able to detect a variety of polar vapor molecules adsorbed on graphene [119]. As shown in Figure 3.1, they measured changes in resistivity of a graphene device upon separate adsorptions of ammonia ( $\text{NH}_3$ ), carbon monoxide ( $\text{CO}$ ), water ( $\text{H}_2\text{O}$ ), and nitrogen dioxide ( $\text{NO}_2$ ) molecules.  $\text{NH}_3$  and  $\text{CO}$  caused positive changes to resistivity, while  $\text{H}_2\text{O}$ , and  $\text{NO}_2$  caused negative changes. The authors attributed these positive and negative valued changes to electron and hole doping, respectively, of graphene from the molecules.

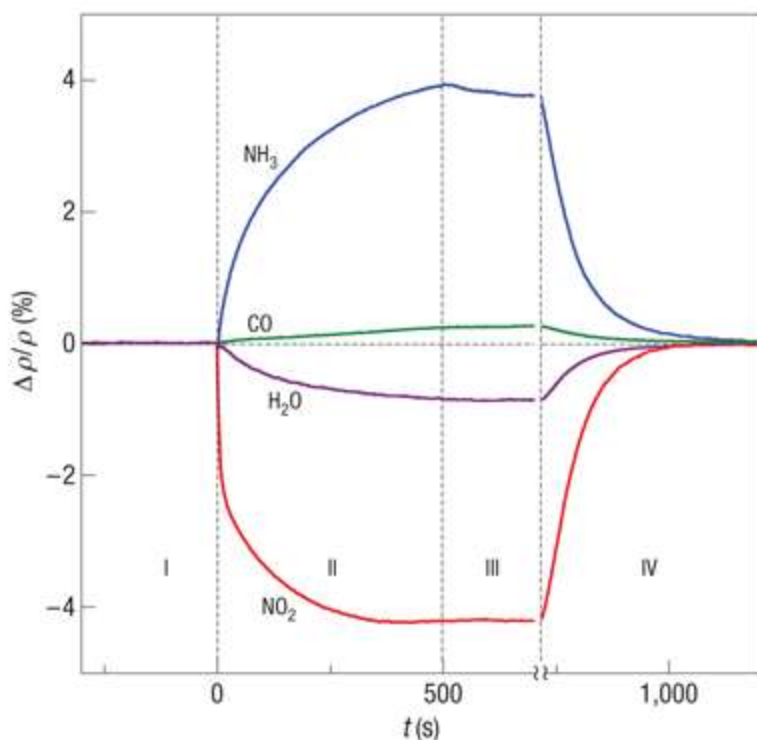


Figure 3.1: Changes in resistivity as a function of time exposed to various polar gases for a graphene sensor device. After initial time in vacuum in region I, the device was exposed to gases in region II. The chamber was evacuated in region III, and the device was annealed in region IV. From Ref. [119].

Romero *et al.* studied adsorption and desorption of  $\text{NH}_3$  on a graphene device in great detail [120]. Instead of measuring changes in resistivity, they observed shifts in the Dirac voltage peak upon exposure of the graphene device to ammonia. They reported significant p-doped device behavior in ambient, which was reversed by high-temperature annealing in vacuum. They attributed the prior p-doped behavior to adsorption of  $\text{O}_2$  molecules from ambient. Figure 3.2 shows how  $\text{NH}_3$  adsorption and desorption cycles affect the position of the Dirac peak. Upon exposure of the vacuum-annealed graphene device to  $\text{NH}_3$ , the device exhibited a negative shift in Dirac peak position. The Dirac peak position shifted back positively after vacuum-annealing.

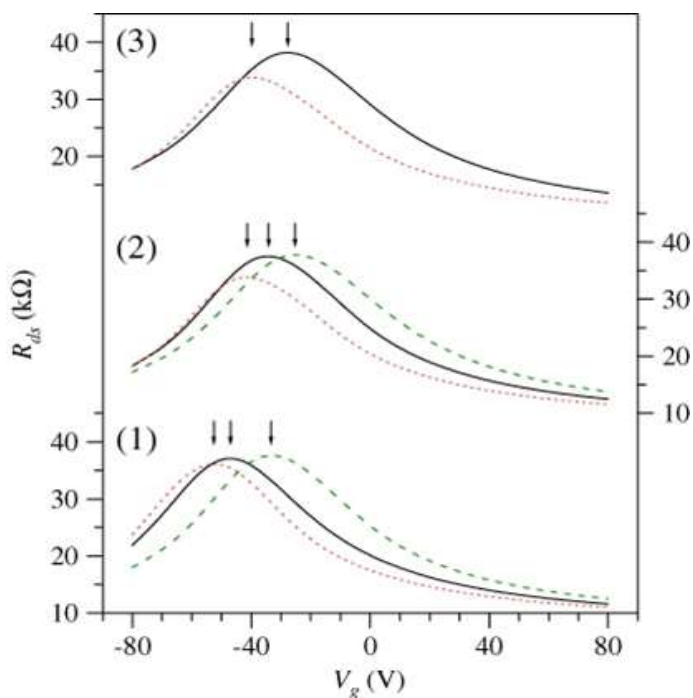


Figure 3.2: Resistance as a function of gate voltage for  $\text{NH}_3$  exposure–desorption cycles one through three. The solid curves were measured before exposure, the dotted curves were measured after desorption, and the dashed curves were measured after vacuum-degassing at high temperature. From Ref. [120].

Thus, vapor phase molecules are very helpful in studying trapping and transport phenomena and help clarify the chemical physics of a graphene system.

### 3.2 EXPERIMENTAL

Our graphene device fabrication begins with monolayer graphene grown via chemical vapor deposition on copper foil [86]. Next, poly(methyl methacrylate) is used to transfer a square centimeter-sized piece of graphene onto thermally-grown  $\text{SiO}_2$  (285 nm thick, on heavily-doped Si wafer) via a wet transfer method described in previous work [43, 44, 86]. Oxygen plasma reactive ion etching was used to define the active channel region to ensure device isolation as shown in Figure 3.1. Source and drain contacts are

patterned by e-beam lithography to give a channel W/L of 60/1  $\mu\text{m}$ . Ti/Pd (3/50 nm) contacts are e-beam evaporated to complete the top contact, bottom gate graphene FET.

Figure 3.1a shows a cross-sectional schematic of the completed graphene FET. Our basic experimental setup for ambient, room temperature testing of graphene FET devices under exposure to various polar solvent vapors is shown in Figure 3.1b. After saturating a piece of filter paper with a few drops of the desired reagent-grade liquid solvent, we roll the paper into a cylindrical shape and place it in a syringe. This syringe is connected to a nitrogen gas line, and pressure is supplied by a Manostat Vera peristaltic pump with variable flow rates. The tip of the syringe is placed within close proximity to the graphene FET channel surface, where the graphene FET is secured atop the vacuum chuck of a Cascade Microtech probe station, which is open to the air. Electrical characterization is carried out with an Agilent 4155C semiconductor parameter analyzer and Agilent EasyEXPERT software. Additional details of the measurement setup can be found in prior published work by our group [121].

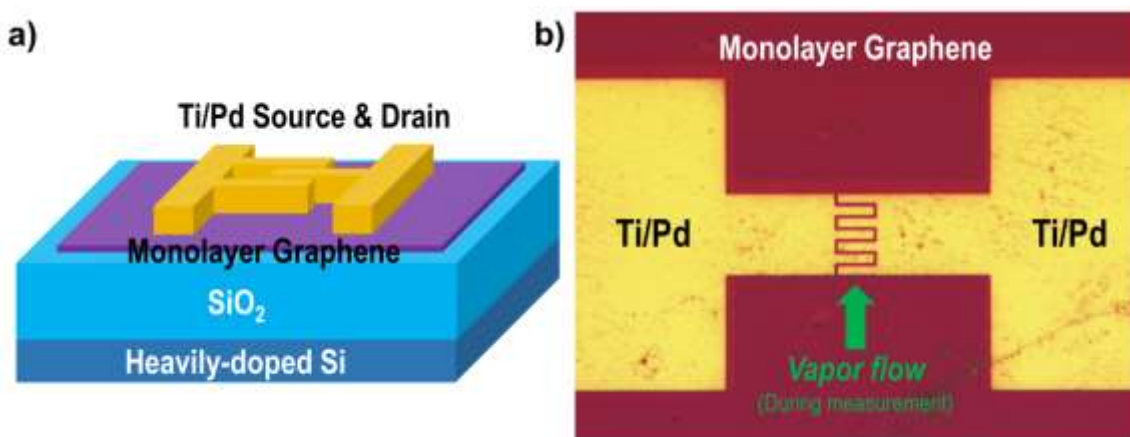


Figure 3.1: a) Schematic cross-section and b) optical image of graphene FET device, showing the channel and introduction of polar vapors.

### 3.3 RESULTS AND DISCUSSION

The electrical characteristics of our graphene FET in ambient, along with normalized results for exposure to nitrogen, isopropyl alcohol (IPA), ethanol, and acetone vapors are shown in Figure 3.2a. Initially, the Dirac peak of the as-fabricated graphene FET is observed at around +40 V, primarily due to adventitious doping of graphene by charged impurities and defects [4]. Figure 3.2b shows a clear relation between dipole moment of impinging polar vapor molecule and resultant Dirac voltage shift. Dipole moment data for the vapors used in the experiment were obtained from “Selected Values of Electric Dipole Moments for Molecules in the Gas Phase” [122]. It was determined that the chemical property which best explains the results of our experiments is dipole moment. Figure 3.2c displays initial graphene FET values of both hole (a) and electron (b) mobility of 748 and 649 cm<sup>2</sup>/Vs, respectively. Note that the initial mobility values are rather low due to the significant presence and large possible variety of charged impurities and defects present in and around the graphene layer of our samples. Also shown is the initial carrier concentration of 6.21x10<sup>11</sup> cm<sup>-2</sup> (Figure 3.2d). We used the fitting model described by Kim et al. to calculate both  $\mu$  and  $N_0$  [114]. Figure 3.2a shows that the exposure of our graphene FET to various polar analyte vapors results in a significant shift in the Dirac voltage toward zero. Figure 3.2b illustrates the dependence of the downshift in the Dirac voltage on the magnitude of the dipole moment of impinging analyte type. Both IPA and ethanol have roughly the same dipole moment, while acetone is significantly more polar. These changes are consistent with nearly complete neutralization or screening of charged impurities and defects by electrostatic or van der Waals interaction with the polar analytes used.

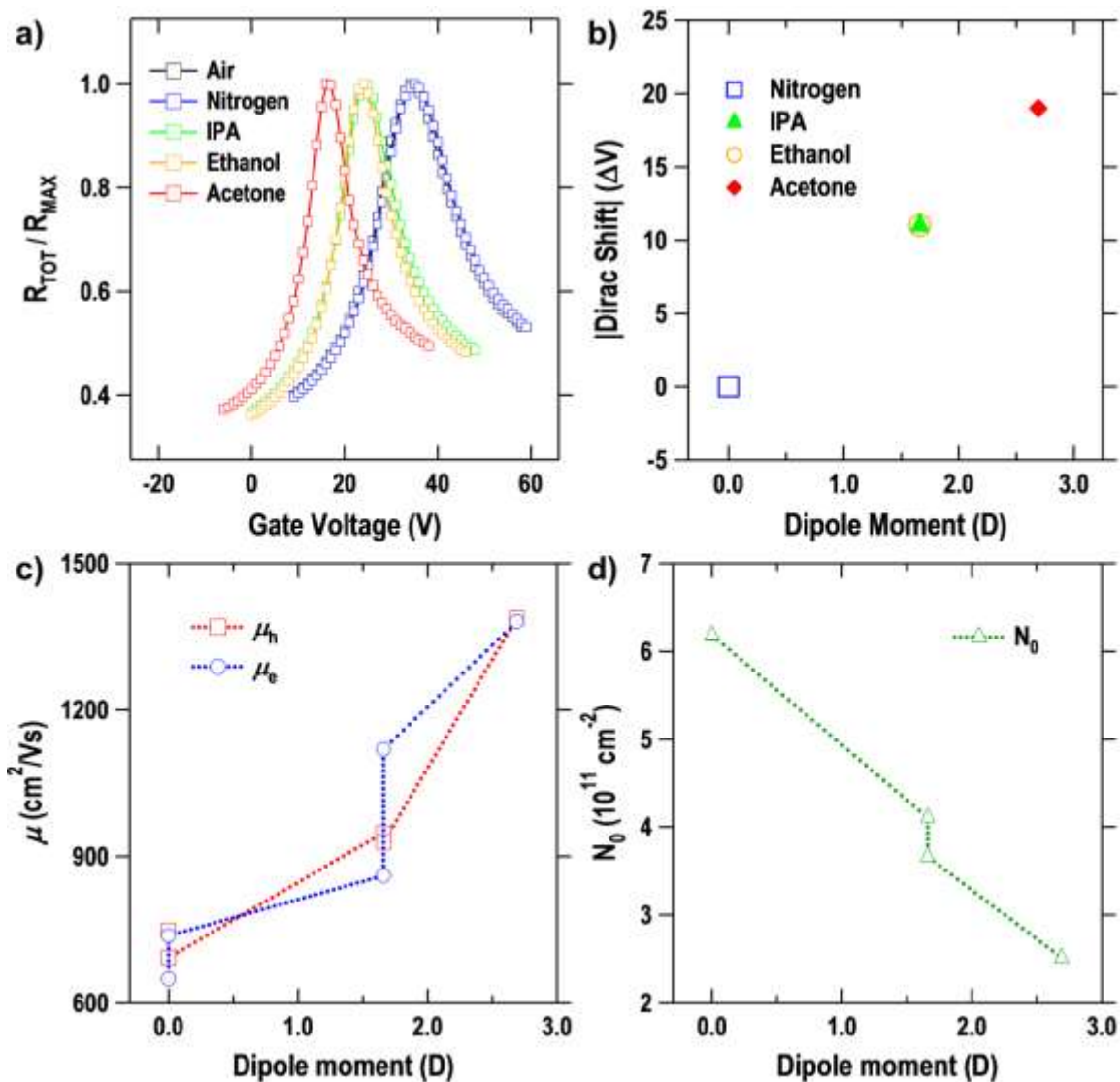


Figure 3.2: a) Plot of normalized resistance as a function of gate voltage for a graphene FET in ambient under various analyte exposure conditions. Plots of b) Dirac voltage shift, c) electron and hole mobilities, and d) residual carrier concentration as a function of theoretical dipole moment of each polar vapor.

On the other hand, Figure 3.2 and Figure 3.3 illustrate that molecules with no dipole moment, such as nitrogen ( $N_2$ ) and hexane, have no observable effect on measured device characteristics. While data shown in Figure 3.3 was measured on a different device

than that in Figure 3.2, it supports our hypothesis that the dipole moment of impinging vapor molecules is the distinguishing factor for improvement of graphene FET device characteristics. The graphene mobility values are observed to increase with increasing dipole moment of impinging solvent molecule. These results are shown alongside the initial mobilities in Figure 3.2c. Simultaneously,  $N_0$  is observed to decrease with increasing dipole moment. As discussed below, mobility and carrier concentration are directly influenced by charged impurities.

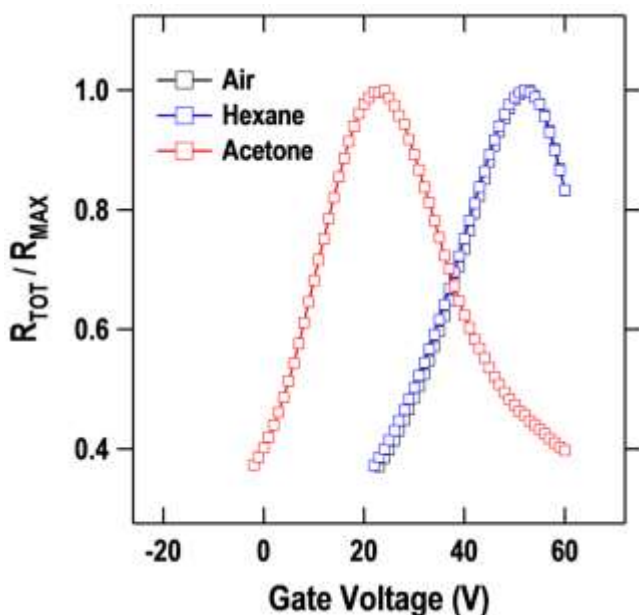


Figure 3.3: Plot of normalized resistance as a function of gate voltage for a graphene FET in ambient under exposure to air only, hexane, and acetone vapors.

It should be noted that, as shown in Figure 3.4, there is significant percent difference in measured values for graphene FETs exposed to various vapors. The significant percent difference shown here is not of great importance, given such factors as all devices having different initial Dirac voltages, different widths/lengths of graphene channels and different dielectric thicknesses. Indeed, significant variation in initial

measurements from device to device was also seen in Figure 2.5. Further, the small sample size (3-4 devices measured per data point) does not lend much statistical weight to the percent difference. However, our interpretation of these results is primarily a qualitative one, and remains consistent with previous results from work using fluoropolymers.

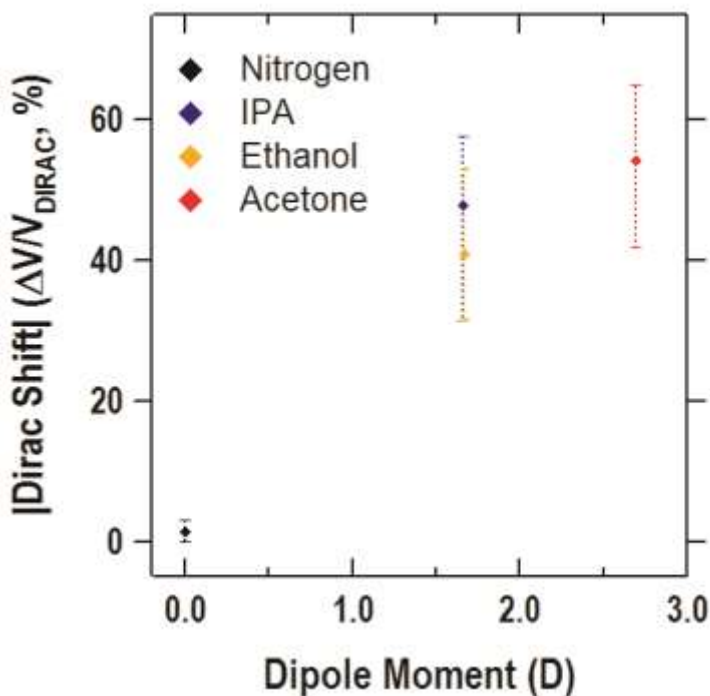


Figure 3.4: Plot of percent difference in Dirac voltage shifts due to exposure to various vapors, shown as error bars.

In a display of reversibility remarkably similar to that seen in previous work by our group on fluoropolymer coatings, Figure 3.5 shows that, after turning off the flow of acetone vapor, the Dirac voltage begins to shift back towards the positive value observed before polar analyte exposure. This behavior is consistent with the hypothesis that, after the flow of acetone to the graphene has stopped, acetone molecules previously adsorbed to the graphene surface gradually desorb as time passes, and cease to screen or neutralize

the fields from charged defects. (We would expect that, in comparison to acetone, other polar molecules would have varying rates of desorption from the defect and impurity sites in our graphene. This would be a diffusion-limited or electric field dependent behavior.) Thus, the electric fields of charged impurities and defects may again act to scatter charge carriers, and this is observed in the form of increasingly positive Dirac voltage shifts (Figure 3.5b), reduced mobilities (3.5c), and increased carrier concentration (3.5d). Nitrogen is shown to cause no significant shift in the measured graphene FET electrical characteristics. The apparent reversibility of the interaction between polar molecules and graphene indicates that the nature of this phenomenon is not one of electron transfer, but rather one of charge-screening or neutralization of charged impurities. The reversible charge-screening or neutralization effects of polar vapors are analogous to those brought about by the application and subsequent removal of a fluoropolymer thin film on graphene observed in previous work [43, 44].

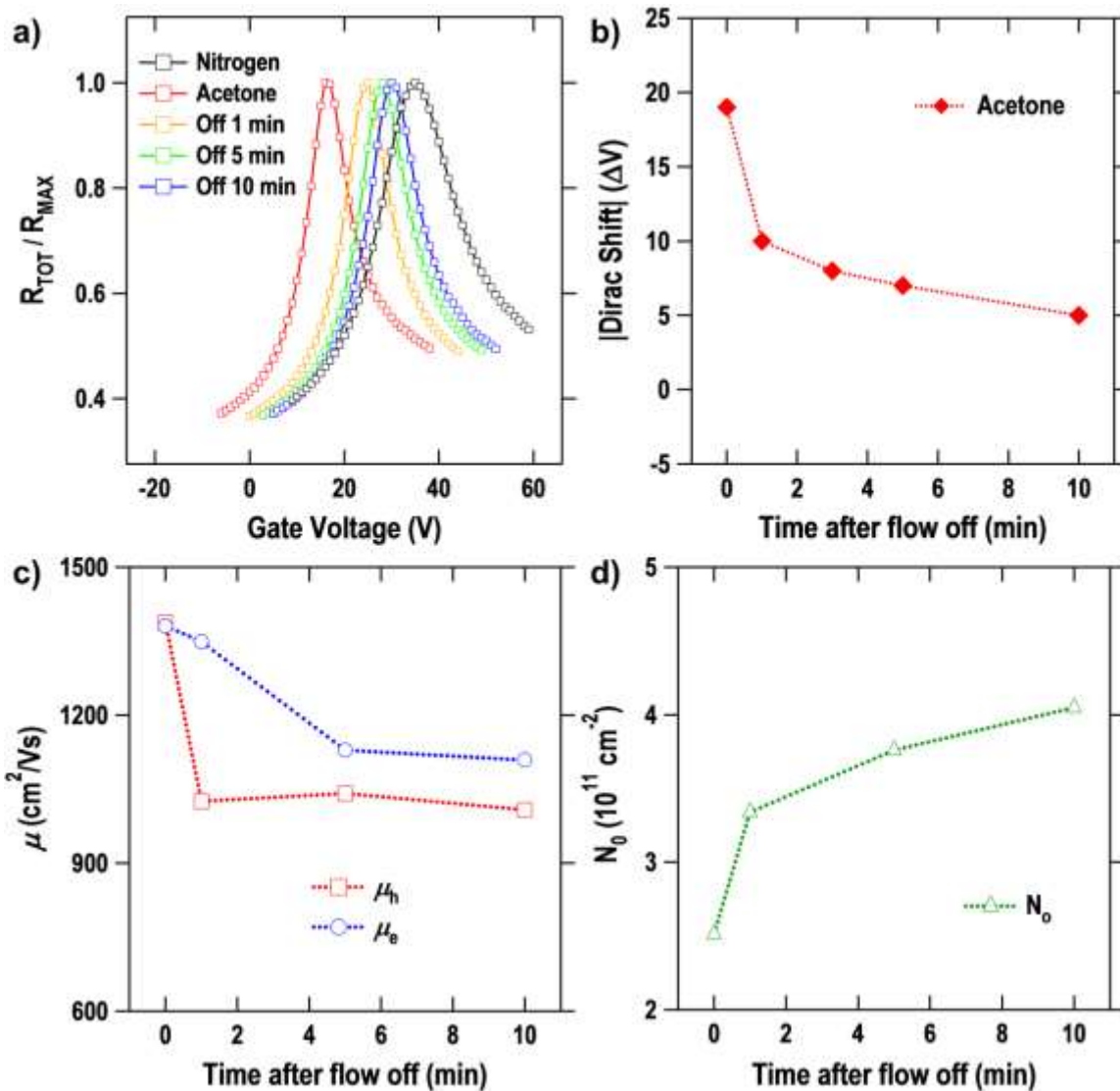


Figure 3.5: a) Plot of normalized resistance as a function of gate voltage showing return of Dirac peak to original position over time after stopping exposure to acetone vapor. Plots of b) Dirac shift magnitude, c) electron and hole mobilities, and d) residual carrier concentration as a function of total elapsed time after acetone vapor flow was stopped.

It is possible that the vapor-phase acetone molecules form a non-uniform layer atop the graphene, self-organizing into an inhomogeneous dielectric layer under the influence of the electric field generated by charged impurities and defects so as to

neutralize the charged impurities via electrostatic interaction. The present experiment does not provide insight on such a detailed extent of characterization, because we conducted these experiments in ambient air. Nevertheless, forming a much higher- $\kappa$  dielectric environment than that made up by the now-displaced ambient air, the acetone layer decreases the dimensionless coupling constant  $a$  as discussed by Jang, *et al* [39]. Others have also postulated that high- $\kappa$  dielectrics could play a role in screening Coulombic impurity scattering. Again, we point out the simple, but paramount difference in phase of media (liquid versus vapor) used to modify the graphene environment between our experiments and those described in Newaz, *et. al* [40]. Additional work is underway to confirm if indeed this dielectric mechanism is acting in conjunction with other impurity neutralization mechanisms to improve graphene FET characteristics. The evidence for impurity neutralization is, however, very clear. As mentioned above, the present vapor-phase experimental design is a simpler system than the fluoropolymer thin-film-capped graphene FET reported previously by our group. Instead of the multitude of C-F bonds oriented first, along the fluoropolymer backbone, and second, according to reorganization of the thin film during annealing, vapor phase molecules from analytes of high purity (99%+) and known dipole moment are expected to be free to adopt the optimal conformation atop the graphene so as to affect the greatest extent of charged impurity neutralization at room temperature (annealing being unnecessary). Additionally, “in situ” changes in relative local concentration/dissipation of polar analyte molecules from the graphene surface can be observed in real time, unlike the fluoropolymer capping method, which requires separate processes to deposit and remove the thin film. It should be noted, however, that the fluoropolymer capping method does hold great potential as a practical method for mitigating the detrimental effects of charged impurities on

graphene transistors, and has also been shown to improve the reliability and operating lifetime of graphene FETs [24, 64].

Similar results for vapor-phase modification of graphene were recently reported by Ago and co-workers, who used both vapor-deposition and spin-coating methods to adsorb polar piperidine molecules on the surface of graphene devices [123]. For both methods, the authors reported significant favorable shifts in the Dirac voltage peak and increased mobility. Figure 3.6a shows the significant shift in Dirac voltage peak position for a graphene FET in “pristine” condition, showing significant p-doping behavior. Figure 3.6b shows the greatly n-shifted Dirac peak position upon exposure to greatest tested concentration of piperidine. The blue and red curves are backward and forward sweeps, respectively. Dotted and solid lines in Figure 3.6b are data collected before and after vacuum anneal, respectively. They also attributed the interaction between piperidine and graphene to be a noncovalent one, just as we concluded in our own experiments.

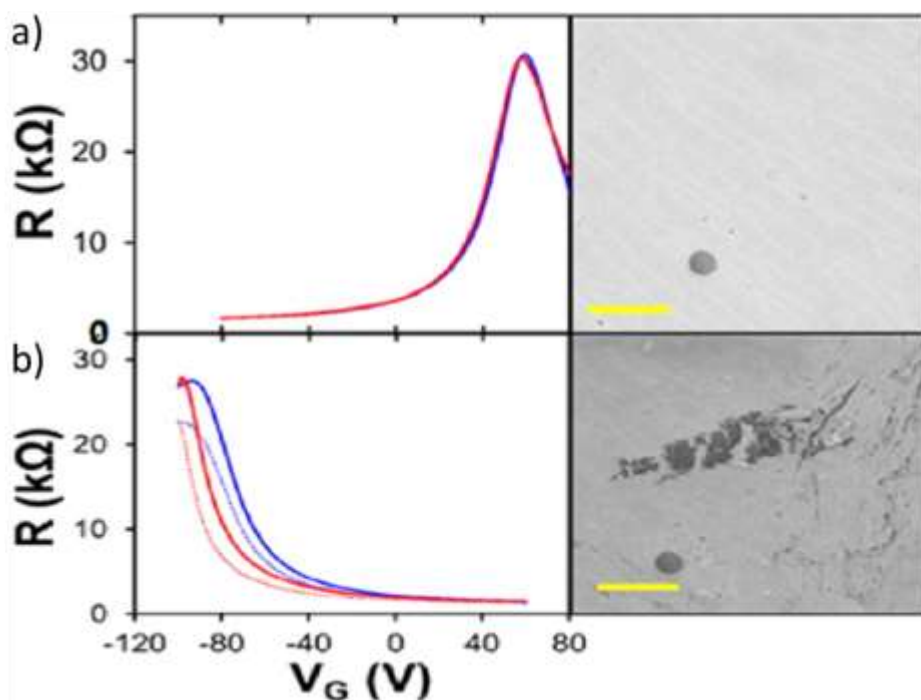


Figure 3.6: Plots of resistance as a function of gate voltage for a graphene FET in a) pristine condition and b) with exposure to piperidine. Right side images are SEM images of graphene area, showing darkening upon exposure to piperidine. From Ref. [123].

The clarity of our vapor-phase experimental results, supported by strong agreement with data gathered from previous work and vapor-phase work from Ago, *et al.*, affords strong evidence that the simple act of bringing polar molecules into contact with graphene and possibly other 2-D materials can act to improve the electrical characteristics of the system by their electrostatic or van Der Waals interaction with charged impurities and defects. The two principal mechanisms by which charged impurities affect graphene transport, long- and short-range scattering, are pivotal in understanding our experimental results. Long-range scattering of charge carriers by impurities is the dominant mechanism limiting mobility in graphene at high carrier

concentrations. Polar vapors evidently act to screen the Coulombic interaction between charged impurities and carriers, mitigating long-range scattering [33, 36, 39]. Simultaneously, polar vapors decrease both the minimum conductivity and  $N_0$ , which are determined by short-range scattering [39, 43, 72].

### 3.4 SUMMARY

In conclusion, we have shown that polar vapors delivered to graphene FETs result in favorable changes to the Dirac voltage, mobility, and residual carrier concentration. The magnitude of the Dirac voltage is greatly reduced, the mobilities of both holes and electrons are increased, and the residual carrier concentration is decreased. The magnitude of these changes tracks with the dipole moment of vapor molecule used. These changes, along with their reversibility upon vapor molecule desorption, are analogous to previous work on graphene FETs coated with films of various polar fluoropolymers. The evidence strongly suggests that polar groups significantly screen the fields of charged impurities (but, do not transfer electrons), which improves mobility due to a reduction in charged impurity scattering. Alteration of the dielectric environment surrounding the graphene monolayer may also reduce the fine structure constant of graphene, contributing to the observed improvements.

## Chapter 4: Computational Modeling of the Interactions of Pristine and Impure/Defective Graphene with Polar Molecules

### 4.1 INTRODUCTION

Graphene, graphene nanoribbons, and other emerging 2-D materials show great promise for use in a variety of microelectronics applications [6, 10, 12, 32, 36, 47, 72, 113, 124-127]. However, due to scattering effects from impurities and defects which incorporate in and around the materials during growth, handling, and device fabrication processes, graphene and similar materials exhibit transport metrics well below theoretical limits [9, 11, 26, 32-36, 38-45, 74, 128, 129]. Specifically, long-range, Coulombic scattering is the dominant scattering mechanism in the graphene layer of microelectronic devices fabricated via the popular CVD graphene growth and wet-transfer to substrate method [10, 28, 29, 33, 34, 40, 42, 43, 46, 47, 50, 116, 130]. Measured graphene device properties such as charge carrier mobilities, conductivity, and *on/off* ratios are much lower than predicted in theoretical calculations. Thus, it is imperative that we learn how best to mitigate the effects of charged impurities and defects on graphene and similar 2-D materials.

Previous work by our group has shown that fluoropolymer capping layers provide dramatic improvements to the electrical characteristics of graphene devices [26, 43, 44]. It was found that the fluoropolymers returned the Dirac voltage toward zero gate voltage, whether the Dirac peak was positively or negatively shifted. In many cases, the magnitude of the shift was large ( $>50$  V). At the same time, both electron and hole mobility values increase and residual carrier concentration decreased. It was hypothesized that these improvements were due both to the polar fluoropolymers' screening of charged impurities and defects at the graphene monolayer and to a change in the dielectric environment around graphene. We followed these experiments with model

experimental studies using polar, vapor-phase molecules delivered to a graphene device surface [45]. These molecules also acted to mitigate the effects of charged impurities present at the graphene/substrate or graphene/air interface(s), thus improving key electrical characteristics of the devices. We attributed this mitigation to electrostatic interaction between the dipoles of the polar vapor molecules and the charged impurities. The reversible nature of the improvements to the device upon removal of the fluoropolymers or dissipation of the polar molecules supported our hypothesis that the effect was caused by electrostatics, as opposed to covalent bond formation or some other electronic interaction.

## 4.2 QUANTUM MECHANICAL STUDIES

We sought to better understand how polar molecules interact with graphene, both pristine and with impurities and defects. To model the electronic interactions between these molecules, we used quantum mechanical chemistry Gaussian 09 [131] and GaussView [132] software on both our own simulation desktop computer and the Texas Advanced Computing Center Lonestar 4 cluster. We acknowledge the Texas Advanced Computing Center (TACC) at The University of Texas at Austin for providing HPC resources that have contributed to the research results reported within this dissertation. (URL: <http://www.tacc.utexas.edu>.) A number of papers in the literature concern the interactions of small molecules on various types of graphene, with a general consensus that density functional theory (DFT) methods offer a good compromise between computational accuracy and efficiency. DFT is a quantum mechanical method which uses functions of functions, also known as functionals, to compute the total energy of an atomic system given in terms of electron density [133]. Leenaerts, *et al.* used DFT methods to perform first-principles calculations for adsorption energy ( $E_a$ ) and charge

transfer ( $\Delta Q$ ) of NH<sub>3</sub>, NO<sub>2</sub>, nitric oxide (NO), CO, and H<sub>2</sub>O on a graphene sheet [98].

Table 4.1 provides a summary of their results.

Adsorbate	Theory	Expt.	$E_a$ (meV)	$\Delta Q$ ( $e$ )
H <sub>2</sub> O	Acceptor	Acceptor	47	-0.025
NH <sub>3</sub>	Donor	Donor	31	0.027
CO	Donor	Donor	14	0.012
NO <sub>2</sub>	Acceptor	Acceptor	67	-0.099
NO	Donor		29	0.018

Table 4.1: Summary of Leenaerts, *et al.* DFT results. From Ref. [98].

The theoretical results concerning the donor/acceptor relationship between the molecules and graphene are in good agreement with the experimental results of Schedin and coworkers [119]. NO<sub>2</sub> exhibits both the strongest adsorption on graphene and the greatest amount of charge transfer from graphene. The strongest donor of charge to graphene is NH<sub>3</sub>, which also shows the strongest adsorption on graphene among donor molecules. It should be noted that the generalized gradient approximation (GGA) of Perdew–Burke–Ernzerhof [134] used by Leenaerts, *et al.* tends to underestimate binding energies, so we would expect appreciably stronger adsorption of polar molecules on graphene in experimental results. Ray also used DFT to simulate adsorption of CO, carbon dioxide (CO<sub>2</sub>), NH<sub>3</sub> and NO<sub>2</sub> on a graphene [135]. However, he used the local density approximation (LDA) [136], which tends to overestimate binding energy, and simulated

adsorption on a graphene transistor. The results are summarized (approximately) in Table 4.2.

<b>Adsorbate</b>	<b>Theory</b>	<b><math>E_a</math> (meV)</b>
NH <sub>3</sub>	Donor	240
CO	Donor	130
CO <sub>2</sub>	-	320
NO <sub>2</sub>	-	320

Table 4.2: Summary of Ray DFT Results. From Ref. [135].

It is evident that LDA-calculated adsorption values of polar molecules on graphene are much greater than those calculated with GGA methods. According to Umadevi and Sastry, who also studied adsorption on graphene, adsorption strengths for small molecules below 5 kcal/mol (220 meV) can be classified as physisorption [104], where the electronic structure of the involved molecules is not greatly perturbed. They classify adsorption strengths for small molecules above 12 kcal/mol (520 meV) as indicative of chemisorption, where the electronic structure may be strongly perturbed as chemical bonds are formed. Polarizability and a variety of other effects must also be considered when describing adsorption process, but these two sets of adsorption energy values provide a range of values against which we may compare our own calculations for validity. From comparison of the adsorption energy values between these two tables, it is obvious that the computational methodology plays a significant role in the quantitative result of the system under study.

We used a variety of combinations of exchange-correlation functionals and basis sets available in Gaussian 09 to calculate optimized energies for single molecules. We calculated the results reported here using the functional known in Gaussian as PBE/PBE with the 6-31G(d,p) basis set. In the Gaussian 09 nomenclature shown here, keywords represent each functional and basis set, where the first three letters represent the exchange functional, the next three letters represent the correlation functional, and the number and letter keyword following the forward slash represents the basis set. For example: PBE/PBE/6-31G(d,p) represents the 1996 functional of Perdew, Burke and Ernzerhof for exchange [134], the 1996 gradient-corrected functional of Perdew, Burke and Ernzerhof also for correlation [134], and the split-valence basis set of Pople's notation [137], with additional polarization functionals. For further details and references on methods and basis sets, see Gaussian documentation.

While there has been much study of molecular adsorption on perfect graphene monolayers, such pristine graphene is never found in as-fabricated graphene devices due to scattering effects from impurities and defects which incorporate in and around graphene during growth, handling, and device fabrication processes. Thus, it is important to study molecular adsorption on both pristine graphene and graphene with impurities and defects. Early DFT simulation work by Ao, *et al.* showed that CO chemisorbs more strongly to Al-doped graphene than to pristine graphene [138]. They reported a large conductivity change in Al-doped graphene after CO adsorption. Zhang and coworkers also performed LDA DFT calculations of small gas molecules on pristine, B-doped, N-doped, and defective graphene sheets [139]. They reported that CO, NO, NO<sub>2</sub>, and NH<sub>3</sub> all adsorb more strongly on doped or defective graphene than pristine graphene. They also reported a B-doped graphene gas sensor to be two orders of magnitude more sensitive than a pristine graphene sensor.

We performed our own studies using Gaussian software on adsorption of small gas molecules on both pristine graphene and graphene with impurities (dopants) and defects. Figure 4.1 shows some of the graphene small molecules and periodic structures used in the simulations. Coronene has been described as the smallest molecule that reasonably approximates graphene [140-142], and is shown in Figure 4.1a. We used coronene as an abbreviated form of graphene (GA) that is computationally less expensive, as compared to a slightly larger graphene-like molecule (G70) shown in Figure 4.1b, and a graphene sheet with periodic boundary conditions (GPBC) shown in Figure 4.1c. Also shown are GA with a single carbon atom vacancy defect (GAV) in Figure 4.1d, and GA with a Boron atom dopant (GAB) in Figure 4.1e. Similar defective and B-doped variations of G70, and B-doped GPBC were also studied (not shown).

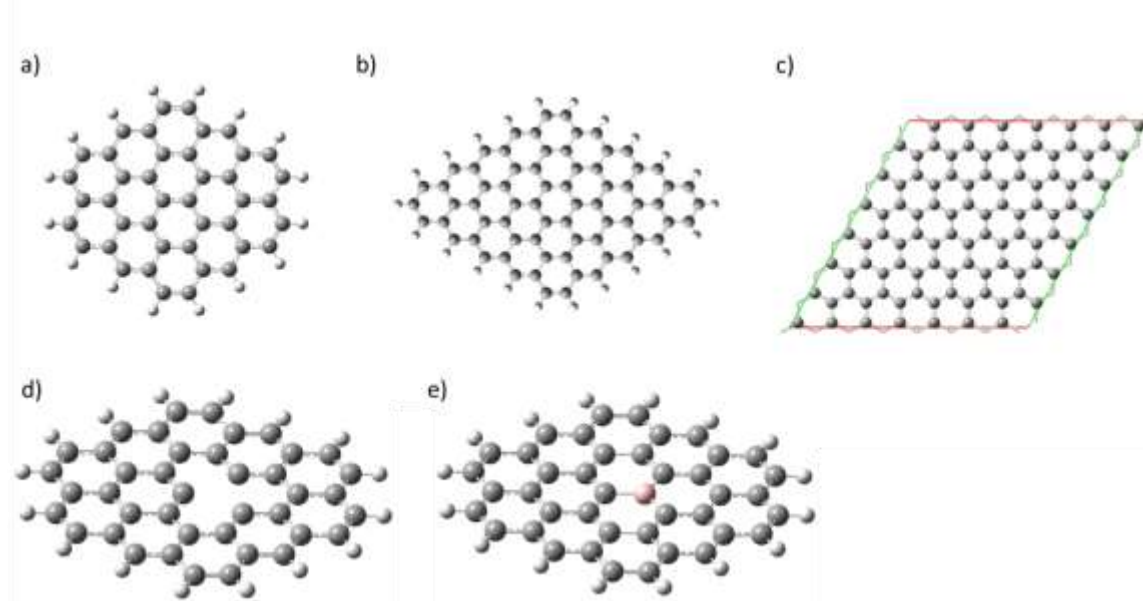


Figure 4.1: Graphene models used including a) coronene aka GA, b) G70, c) periodic boundary graphene sheet GPBC, d) GA with vacancy aka GAV, and e) GA with Boron dopant, aka GAB.

After calculating energies of various small molecules and graphene models alone, we placed the small molecules near each graphene model in GaussView, and optimized geometries to calculate binding energies (using the GGA DFT PBEPBE/6-31g(d,p) functional and basis set) according to Equation 4.1:

$$E_B = E_{(Graphene+Molecule)} - E_{Graphene} - E_{Molecule} \quad [4.1]$$

Where  $E_{(Graphene+Molecule)}$  is the total energy of the molecule atop the graphene model, and  $E_{Graphene}$  and  $E_{Molecule}$  are the separate energies of the graphene model and molecule, respectively.

Figures 4.2a and b show an example of fluoromethane ( $\text{CH}_3\text{F}$ ) atop GA and GAV in GaussView. Given our group's experimental results obtained using fluorinated molecules such as  $\text{F}_{16}\text{CuPC}$  and  $\text{CYTOP}^{\text{®}}$  on graphene, we considered the small  $\text{CH}_3\text{F}$  a good fluorinated molecule with which to begin our computational investigations. After optimization, the pristine GA molecule shows no visible structural change in reaction to  $\text{CH}_3\text{F}$ , and the binding energy is calculated at -0.07 eV. This energy is indicative of a very weak interaction. After optimization of  $\text{CH}_3\text{F}$  atop GA with a vacancy, however, the GAV molecule exhibits significant torsion in response to the  $\text{CH}_3\text{F}$  molecule, and one of the GAV carbon atom nearest the vacancy appears to have formed (presumably partial)  $\text{sp}^3$  bonds to its neighboring atoms. We calculated a binding energy of -1.1 eV for this system, which is over an order of magnitude greater in binding strength compared to  $\text{CH}_3\text{F}$  atop pristine GA.

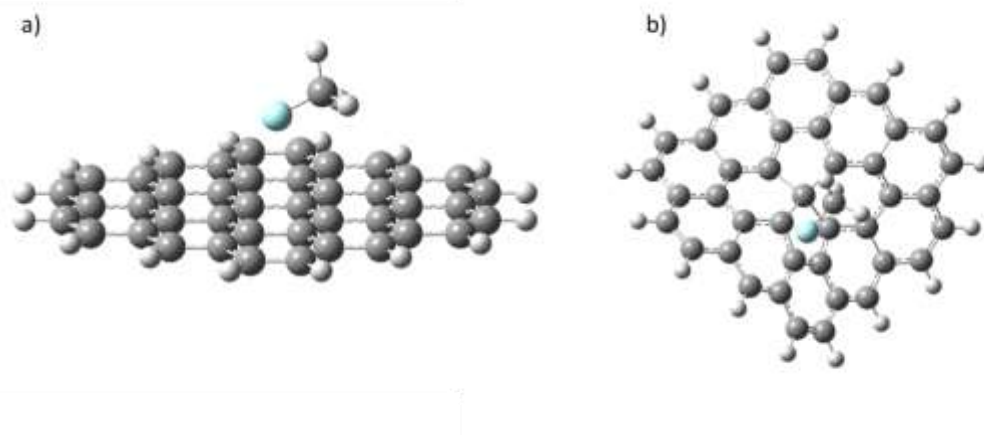


Figure 4.2: GaussView models of  $\text{CH}_3\text{F}$  on a) GA and b) GAV after optimization.

Another graphene impurity we considered was a Boron dopant in the GA lattice. Figures 4.3a and b show the GaussView models of ammonia ( $\text{NH}_3$ ) atop GA and GAB. After optimization, the Hydrogen atoms of  $\text{NH}_3$  are 3.10 Angstroms ( $\text{\AA}$ ) from the pristine GA molecule, the pristine GA molecule shows no visible structural change in reaction to  $\text{NH}_3$ , and the binding energy is calculated at -0.083 eV. Again, this energy is indicative of a weak interaction. After optimization of  $\text{NH}_3$  atop GAB, however, the Boron atom in the GAB molecule appears to be pulled out of the plane toward the Nitrogen atom of the  $\text{NH}_3$  molecule, the separation between these two atoms is 1.77  $\text{\AA}$ , and the binding energy is calculated at -0.288 eV. This is a significantly stronger binding energy for  $\text{NH}_3$  toward GAB than pristine GA.

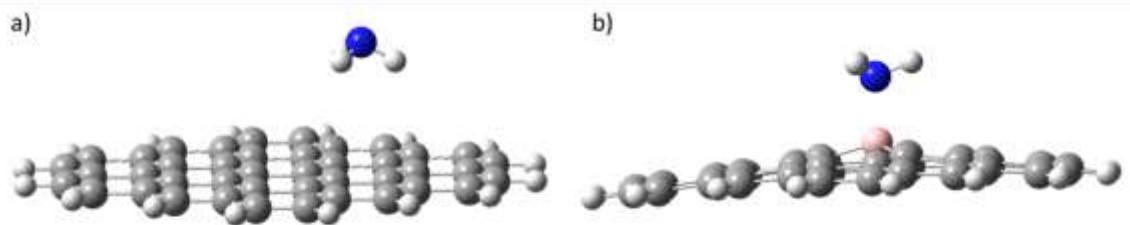


Figure 4.3: GaussView models of  $\text{NH}_3$  on a) GA and b) GAB after optimization.

The results of similar calculations of binding energies are shown in Figure 4.4. It is evident that polar small molecules have greater interaction strength with defective or impurity-containing graphene models than with pristine graphene models. Vacancy-containing graphene models have, by far, the strongest interactions with polar small molecules.

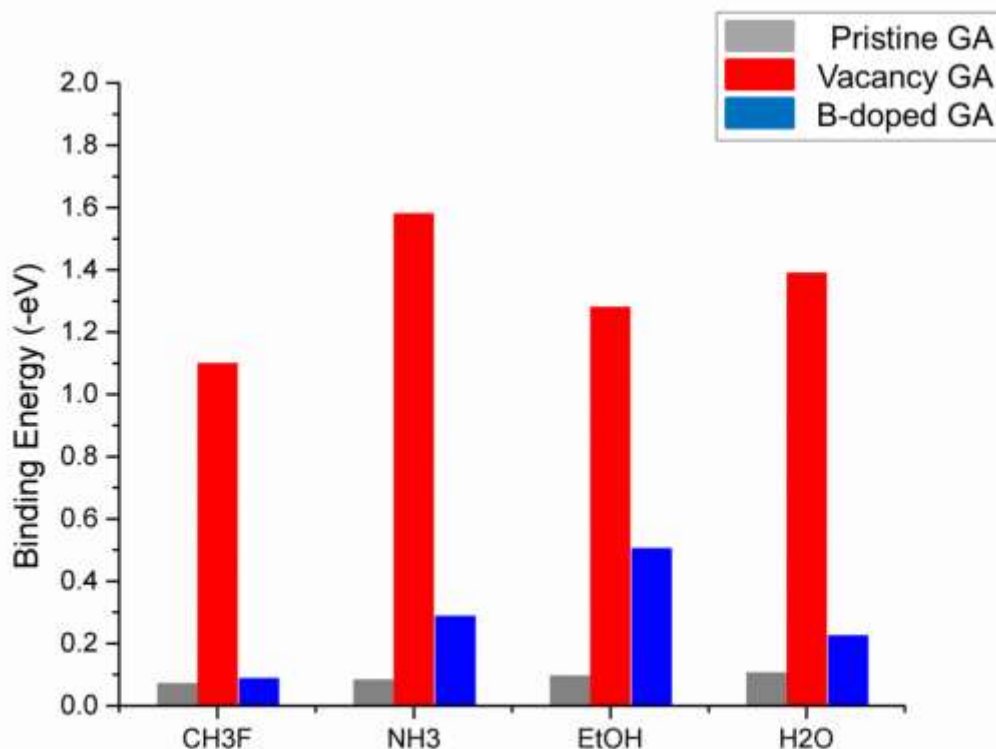


Figure 4.4: Binding energies calculated at PBEPBE/6-31G(d,p) level for various polar molecules and pristine, vacancy defective, and B-doped GA models.

While, for all cases, the strongest binding takes place between the various polar molecules and GAV, the structural changes observed in the graphene model varies with the type of polar molecule. CH<sub>3</sub>F and ethanol (EtOH) caused both apparent twisting and structural “repair,” in that the carbon atom nearest the vacancy of the GAV appears to have formed (presumably partial) sp<sup>3</sup> bonds to its neighboring atoms. On the other hand, molecules such as NH<sub>3</sub> and H<sub>2</sub>O did not appear to alter the structure of GAV aside from twisting. It should be noted that the electronic structure of graphene would not be ideal for graphene with a vacancy either present or repaired (sp<sup>3</sup> bonds formed), as compared

to the unperturbed, all- $sp^2$  structure of theoretical pristine graphene. Nevertheless, our calculations are in qualitative agreement with the literature that small, polar molecules have a greater strength of interaction with impure or defective graphene than with pristine graphene. The former is the state of graphene most likely to be found in fabricated graphene devices tested in air at room temperature, as is the case in most of our group's experiments.

In addition to interaction strengths and structural changes, the electronic interactions between polar molecules, impurity ions such as sodium, and graphene-like molecules such as GA are also of interest. First, a comparison of the highest occupied molecular orbital (HOMO) and lowest unoccupied molecular orbital (LUMO) energy levels between pristine GA, vacancy-containing GAV, and Boron-doped GAB is shown in Figure 4.5. Compared to pristine GA, GAV has significantly raised HOMO and lowered LUMO levels, giving it a much smaller bandgap of about 0.121 eV. The bandgap of GAB, 1.50 eV, is also smaller than that of GA. This data shows that the introduction of a vacancy-type defect into the GA lattice greatly changes the electrical characteristics of the GA molecule, which we use here to model, with computational efficiency, a much larger graphene sheet system.

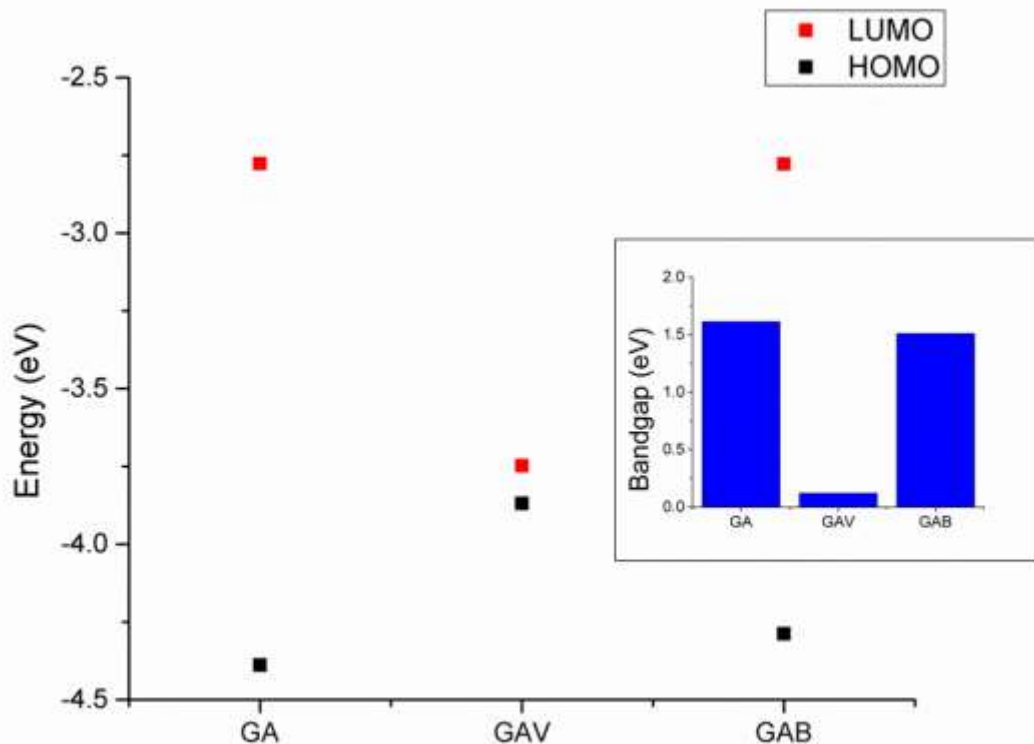


Figure 4.5: HOMO/LUMO energy levels for GA, GAV, and GAB. Inset: Respective bandgaps.

We also calculated the effects of a variety of polar molecules on the HOMO/LUMO levels for GA, as shown in Figure 4.6.  $\text{H}_2\text{O}$ ,  $\text{NH}_3$ , and  $\text{EtOH}$  all slightly lower both HOMO and LUMO levels for GA, while  $\text{CH}_3\text{F}$  slightly raises both. A sodium atom, on the other hand, significantly raises the HOMO and LUMO, with an increase of approximately 1.72 eV in the HOMO level. This change in the HOMO level is over an order of magnitude greater than that of the polar molecules, and helps to illustrate how metal ion-type impurities can greatly alter the electronic properties of graphene, just as they are known to do in traditional silicon microelectronics.

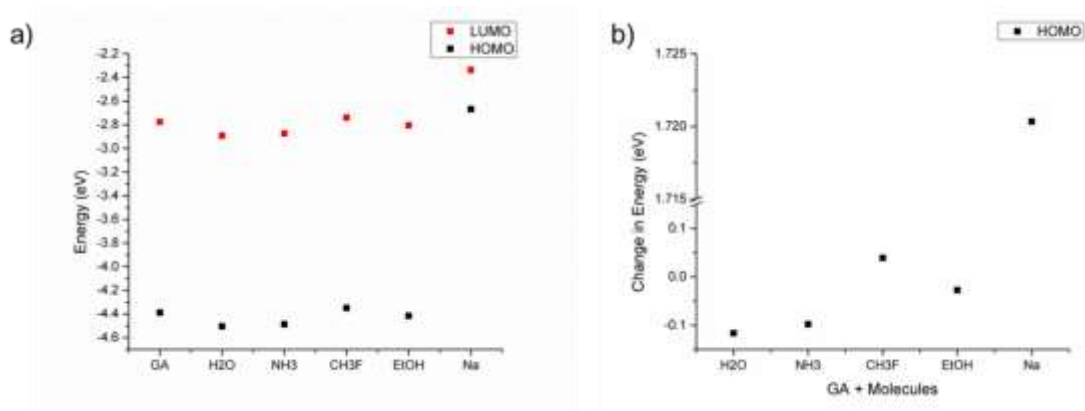
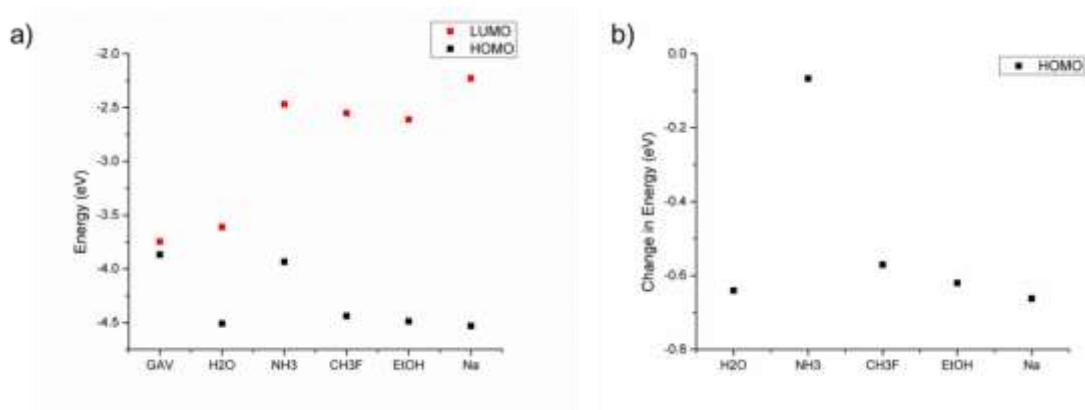


Figure 4.6: a) HOMO/LUMO energy levels for GA with various polar molecules. b) Plot of the change in HOMO level energy for GA with various polar molecules compared to that of pristine GA alone.

Similarly, we calculated the effects of the polar molecules on the HOMO/LUMO levels for GAV, as shown in Figure 4.7. While GAV alone has a very small bandgap, interactions with polar molecules or with a sodium atom significantly increase the bandgap. The sodium atom raises the LUMO level of GAV by the greatest amount, while also lowering the HOMO level to its lowest energy. These effects of the sodium atom result in the greatest bandgap for GAV, 2.30 eV.



### 4.3 MOLECULAR MECHANICAL STUDIES

Having learned both from our quantum mechanical computations that polar small molecules preferentially bind to impure or defective graphene, and from our experiments that such molecules cause favorable improvements to graphene device electrical characteristics, we sought to better understand the mechanism behind polar molecules' mitigation of charged impurities at a graphene surface by performing computational chemical simulations consisting of polar molecules interacting with impurities on a graphene sheet in vacuum. We performed molecular dynamics (MD) studies of a graphene sheet in a periodic unit cell, approximating an infinite graphene sheet. To represent both the charged ion and molecular dipole classes of impurity, we added a sodium cation and a single water molecule, respectively, above the graphene. These two impurities are ubiquitous in microelectronic fabrication, and there is much literature detailing attempts to minimize their effects on devices [50, 100, 143-145]. NVT simulations for each graphene/impurity system both with and without polar molecules gave an ensemble of structures from which to calculate the impurity's electrostatic potential profile in the plane of the graphene sheet. Figure 4.8 shows an example image of an acetone/sodium/graphene system. We then calculated the changes in potential between each system with and without polar molecules to study the mechanisms governing how polar molecules change the effects of impurities on graphene.

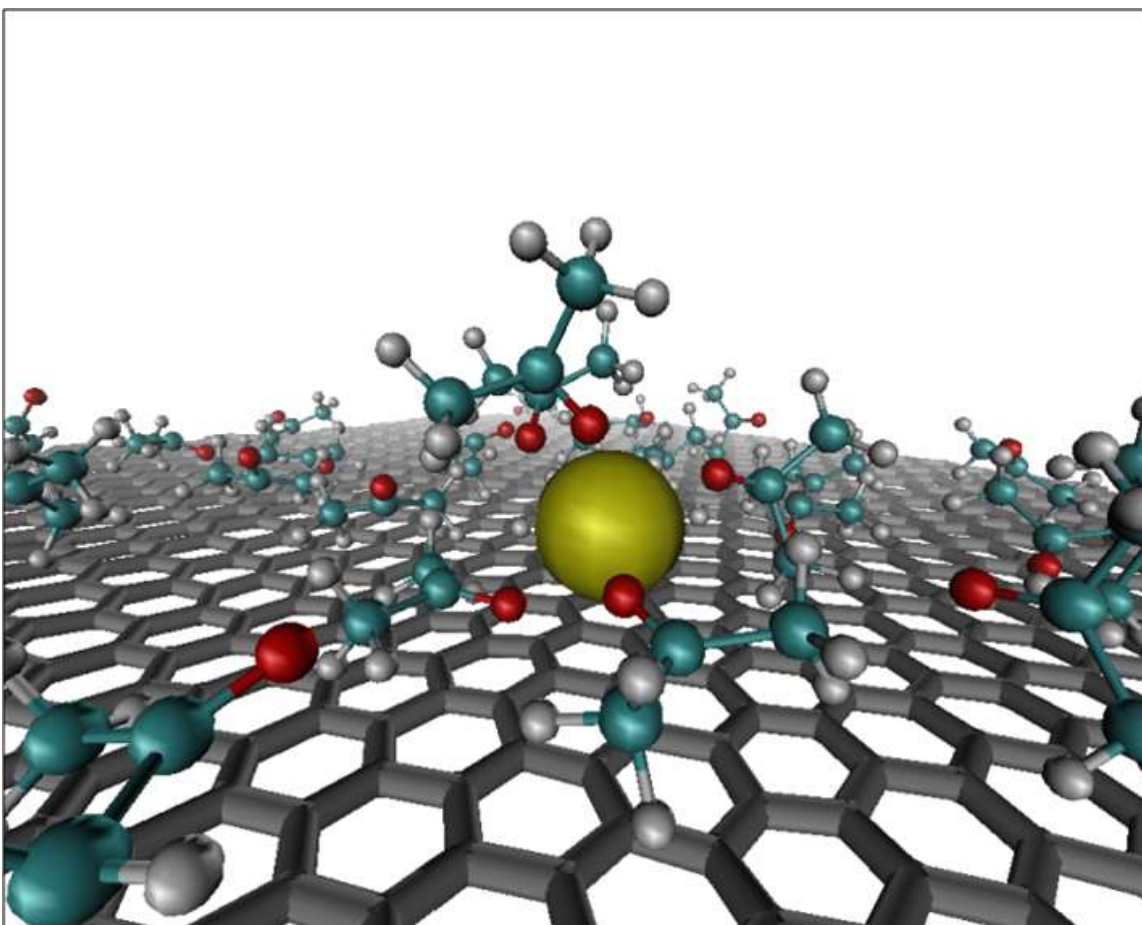


Figure 4.8: A system containing 50 acetone molecules, a sodium ion impurity, and a graphene sheet.

### 4.3.1 Methods

We used the Carbon Nanostructure Builder (version 1.2) extension in VMD software (version 1.9.1) [146-153] to construct a 5 nm by 5 nm graphene sheet consisting of 1008 carbon atoms. We carried out simulations using version 4.5.3 of the GROMACS molecular dynamics software package [154-160] with the OPLS-AA force field, starting with steep energy minimization of the graphene sheet to a maximum force of 10 kJ/mol\*nm [161-164]. Next, we ran a NVT (constant number of particles, volume, and temperature) statistical ensemble simulation for 1 nanosecond at 300 K to equilibrate the

sheet, followed by a production NVT simulation run for 10 nanoseconds at 300 K. In the final step of preparing the graphene sheet, we ran a NPT (constant number of particles, pressure, and temperature) simulation to optimize the size of the unit cell box around the sheet. With a stable system of a graphene sheet inside a periodic unit cell, we then added, separately, a sodium ion of charge positive 1e and a water molecule about 3.5 Angstroms above the sheet. We used the three-site SPC/E water model. While there is ongoing debate in the literature regarding the effects of different water models, polarizability, and other factors on the interaction of liquid water with a hydrophobic surface, such as graphene, we have not included such polarization effects in our calculations. We believe that such issues would be appropriate in a more detailed study specific to water/graphene interactions. Next, we treated each impurity/graphene system to successive steps of energy minimization down to a maximum residual force of 0.5 kJ mol/mol\*nm, NVT equilibration, and 10 nanosecond NVT production simulations. After collecting respective ensembles for each type of impurity, we added 50 molecules of each type of polar vapor. We chose to model the vapors used in our previous experimental work, specifically, acetone, ethanol, and IPA. We then collected respective ensembles for each polar vapor/impurity/graphene system by treating them to the same successive simulations as were done to the impurity/graphene systems. It is evident from viewing the simulation trajectories in VMD that, over the course of the NVT runs, the polar molecules both solvate each impurity and orient their dipoles so as to screen the electrostatic charge of the sodium ion or dipole moment of the water impurity, as expected.

After collecting ensembles from simulations, we calculated the average potentials from each impurity in the plane of the graphene, both with and without polar vapor molecules present. The code first evaluates the atomic coordinates in each simulation

time step, and then calculates the radial potential out to 1 nm from a point on the graphene plane directly beneath the centroid of the impurity atom(s). We can then extract data on the separation distance of the impurity from the graphene sheet, the electrostatic potential in the plane of the graphene sheet from each impurity alone, the potential after inclusion of polar molecules, and the potential when only the displacement of the impurity away from the sheet by polar molecules is considered. Further, we can calculate both the total magnitude of potential reduction by the polar molecules and the potential only from electrostatic screening of the impurity by polar molecules. All potentials are plotted as a function of distance on the sheet from the impurity. Next, we can measure the angles of the water molecule bisector from the z-axis, to observe the orientation(s) of the water impurity over the ensemble, both with and without the presence of polar molecules. The cosines of the measured angles range from -1 to 1, where -1 represents both hydrogens of the water molecule pointing down toward the graphene sheet, 0 represents the water parallel to the sheet, and 1 represents both hydrogens pointing up, away from the sheet. We plotted the probability distributions for these angle data for both the water impurity alone on graphene and with various polar molecules. Finally, we can calculate the range of dipole moments of the various polar molecules, using the charges and positions of their respective atoms averaged over each ensemble of our simulations, and plot these as probability distributions as well.

### **4.3.2 Results with Sodium Impurity**

A plot of the average radial electrostatic potential in the plane of the graphene sheet from a sodium ion impurity is shown in Figure 4.9a. The potential is plotted in two dimensions from the point on the sheet directly below the impurity, and extends radially to a distance of one nanometer (nm). Figure 4.9b shows a “slice” of the radial potential

plot, with the potential as a function of distance in one direction. The potential in the plane of the graphene directly under the sodium ion in the absence of polar molecules is large, and rapidly decays over distance away from the ion. However, inclusion of polar molecules, such as acetone, solvates the sodium ion and significantly reduces the potential at the graphene sheet. Figure 4.9c shows the impurity potential on graphene as a function of distance after inclusion of 50 of each type of polar molecule in separate simulations. Acetone (ACE), ethanol (ETOH), and isopropyl alcohol (IPA) were chosen because they were also used in our experimental work. The observation that polar molecules with greater dipole moments cause greater reduction of calculated impurity potentials (Figure 4.9c and Figure 4.10) correlates well with the similar trend for device characteristic improvements observed in previous work [45].

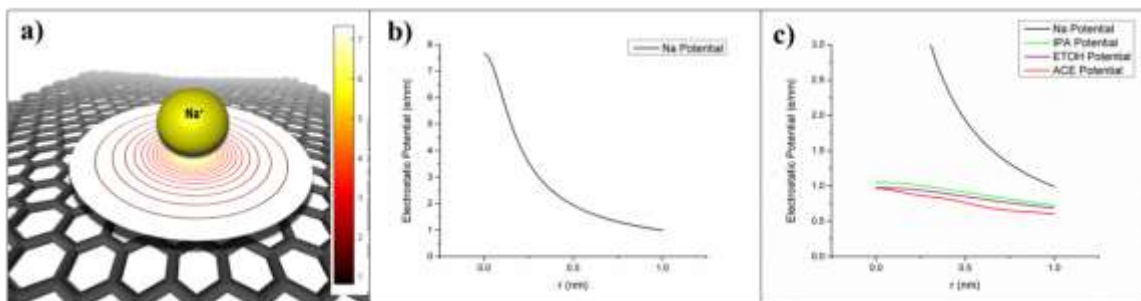


Figure 4.9: a) A sodium ion atop graphene, with radial electrostatic potential distribution shown by colored circles. b) Electrostatic potential in the plane of the graphene sheet from the sodium ion as a function of distance. c) Potential plots after inclusion of polar molecules in the simulation, showing dramatic reduction of the potential at graphene by polar molecules.

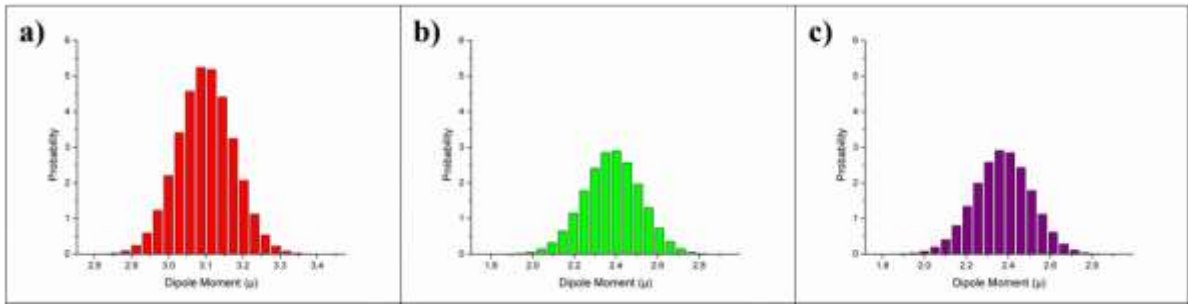


Figure 4.10: Normalized probability distributions of calculated dipole moment values of a) acetone, b) IPA, and c) ethanol molecules in our simulations.

Taking the acetone/sodium ion/graphene case as a general example of the interaction of polar molecules with impurities on graphene, we first calculated the difference in potential between the system with and without acetone molecules. The magnitude by which the acetone molecules reduced the potential is shown as the solid line in Figure 4.11a. We identified two mechanisms by which the polar acetone molecules act to mitigate the potential profile in the plane of the graphene sheet from the sodium ion, as indicated in Figure 4.11a. The first mechanism involves physical displacement of the sodium ion away from the sheet upon solvation by acetone molecules. The second mechanism is the electrostatic screening of the sodium ion's charge by orientation of the acetone dipoles around the cation. These two are distinct effects, although not completely separable, since the screening would be quantitatively affected by the ion position. The average contribution of each of these mechanisms to the potential reduction varies with distance and is shown as a percentage in Figure 4.11b. While displacement is the dominant mechanism at short range from the impurity, screening is increasingly the primary contributor to potential reduction at distances beyond about 0.26 nm, as expected since the ion displacement from the surface is small. Figure 4.12 illustrates physical displacement of the sodium ion away from the sheet upon solvation by acetone molecules.

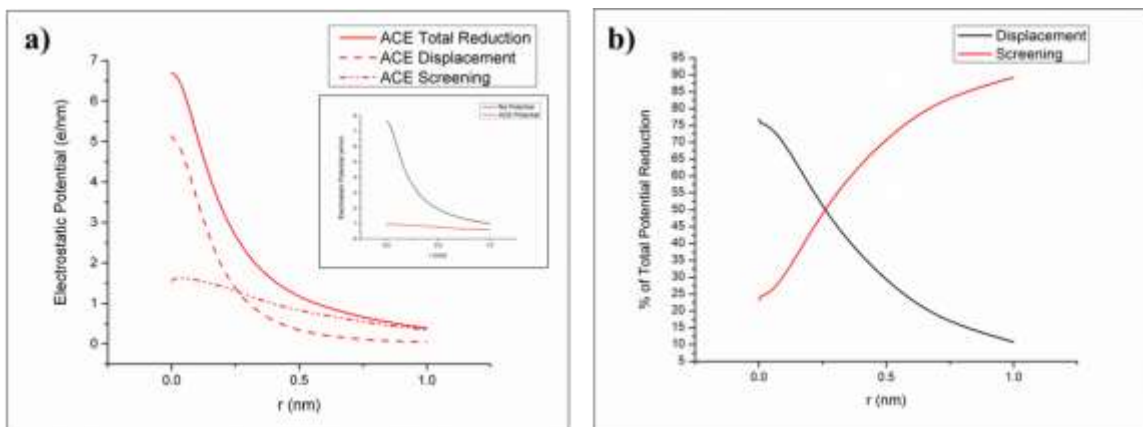


Figure 4.11: Potential plot showing the magnitude of potential reduction by acetone molecules (solid line), contribution of displacement mechanism to this potential reduction (dashed line), and contribution of screening mechanism (dot-dot-dashed line). The inset shows the two potential plots of sodium on graphene with (red) and without (black) acetone molecules. b) Percentage contribution of each mechanism to the potential reduction.

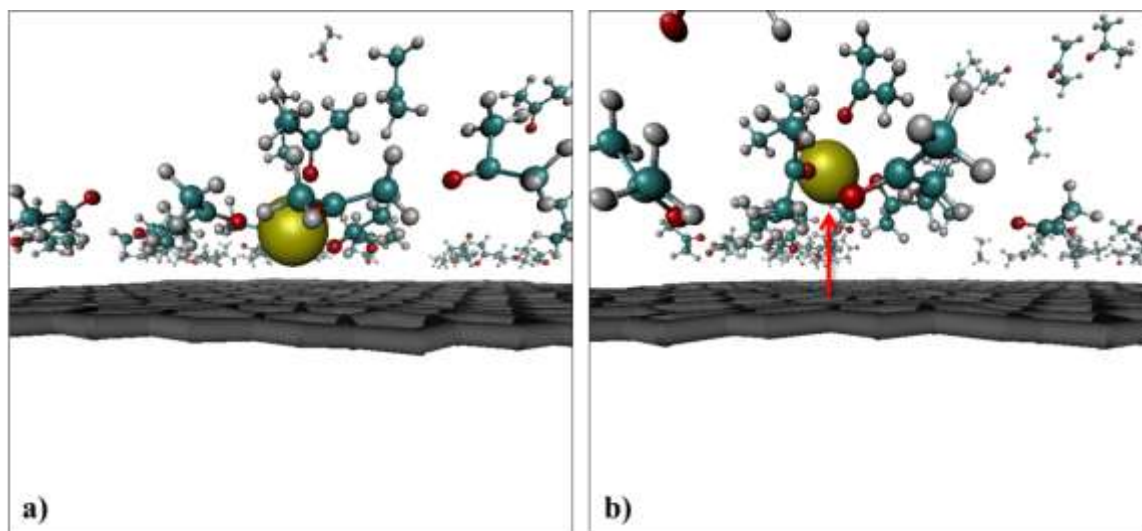


Figure 4.12: Snapshots of graphene/sodium ion system a) before and b) after solvation by acetone molecules.

Additionally, we studied the effects of varying the number of polar molecules per impurity on potential reduction by repeating the 50-molecule acetone simulation with 10 and 25 molecules per unit cell, as shown in Figure 4.13.

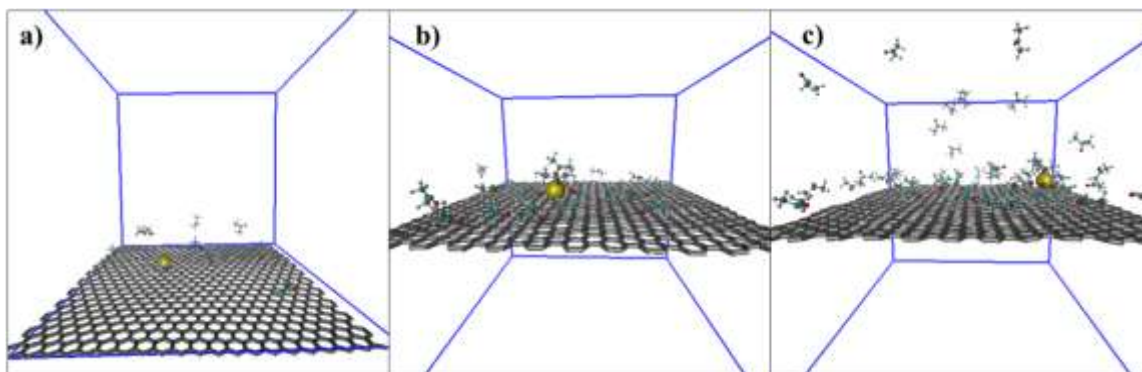


Figure 4.13: Snapshots of graphene/sodium ion system with a) 10, b) 25, and c) 50 acetone molecules.

We observed that greater numbers of polar molecules such as acetone provide both greater magnitudes of potential reduction (Figure 4.14a), and greater displacement of the sodium impurity (Figure 4.14b). Figure 4.14c lends insight into the dependence on the number of molecules for formation of solvation shells around the sodium ion. For only ten acetone molecules present, the distribution of distances between sodium ion and graphene plane is roughly Gaussian with a center at  $\sim 3.5$  Angstroms, representing a single solvation shell of acetone molecules around the sodium ion. This distribution becomes bimodal as more acetone molecules are introduced to the simulation box, representing the formation of a second shell.

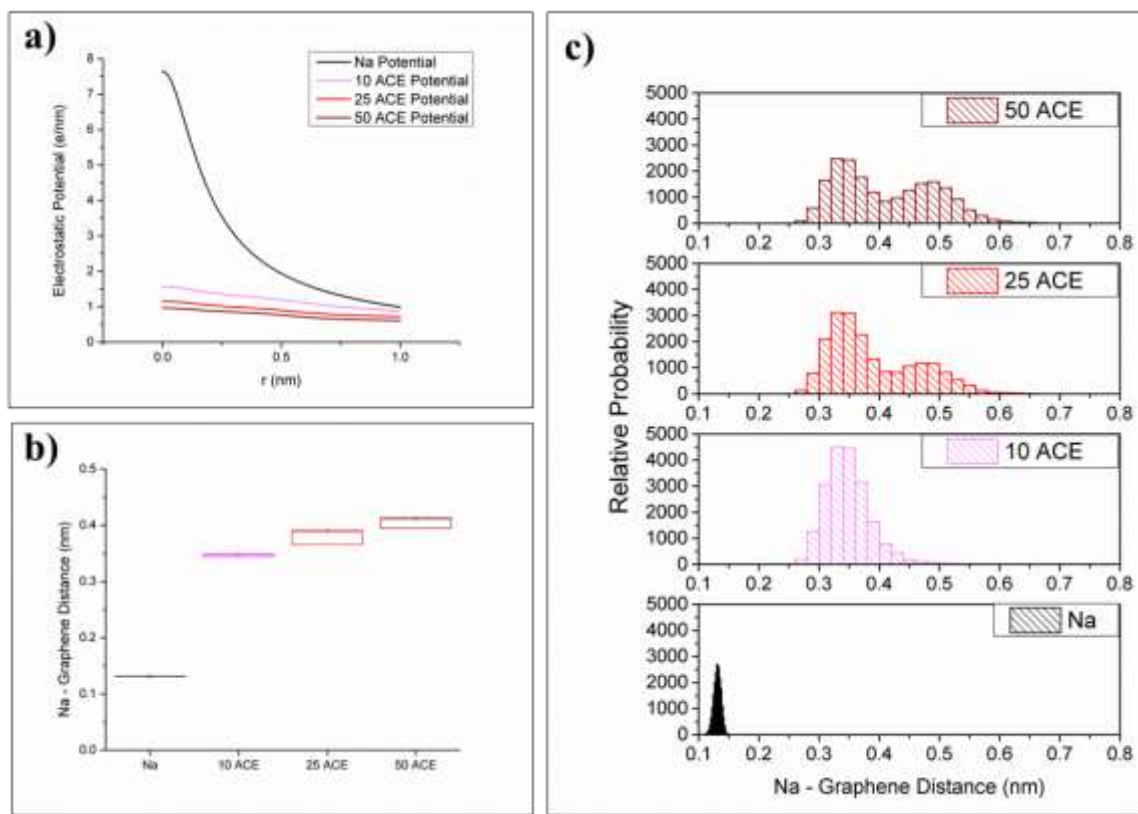


Figure 4.14: a) Potential plots for sodium both alone and with various numbers of acetone molecules. b) Box plots showing mean displacement (small square) of sodium ion away from graphene as a function of number of acetone molecules, with standard error (larger box boundaries). c) Distributions of values of sodium ion displacement by acetones, revealing formation of a second solvation shell with greater numbers of acetone molecules.

Other polar molecules, including a variety of alcohols, simulated with sodium gave results similar to those shown for acetone (Figure 4.15). One important conclusion from this analysis is that the great majority of the screening can be achieved with adsorption of only a few polar molecules.

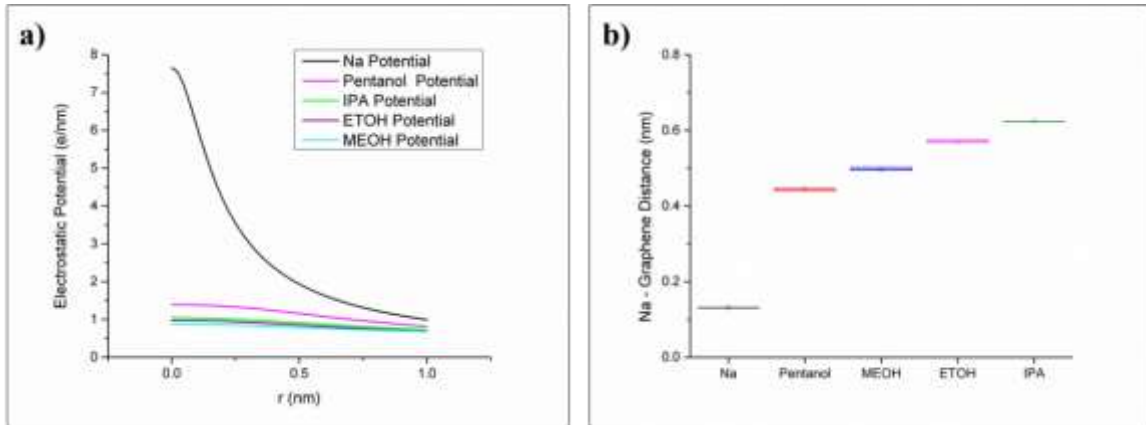


Figure 4.15: a) Electrostatic potential in the plane of the graphene sheet from sodium ion both before and after inclusion of alcohol molecules in the simulation, showing dramatic reduction of the potential at graphene by polar molecules. b) Box plots showing mean displacement (small square) of sodium ion away from graphene as a function of the number of alcohol molecules, with standard error (larger box boundaries).

### 4.3.3 Results with Water Impurity

Water, either adsorbed on top of graphene or trapped between graphene and substrate, may be observed to affect graphene's electrical properties in shifts of the Dirac voltage peak or charge neutral point and hysteresis in graphene FET transfer curves [2, 97, 100, 123, 165]. There is much literature covering extensive calculations of the orientation-dependent water-graphene interaction. For our simulations, we chose two orientations of greatest interaction energy: the “one-leg” orientation, with one hydrogen-oxygen bond vector pointing down toward the graphene; and the “two-leg” orientation, where both hydrogens point toward graphene [98, 166, 167]. As shown in Figures 4.16a and 4.16b, these two orientations of water dipoles cause relatively similar radial potentials in the plane of the graphene in our simulations. The greatest difference in potential between the one-leg orientation and the two-leg orientation is about 0.075 e/nm at 0.2 nm distance on the graphene plane from the point directly below the water molecule (Figure 4.16c). We did not observe significant qualitative differences between

our results for each orientation, so, for the remainder of this discussion, we will consider results from the on-leg simulations.

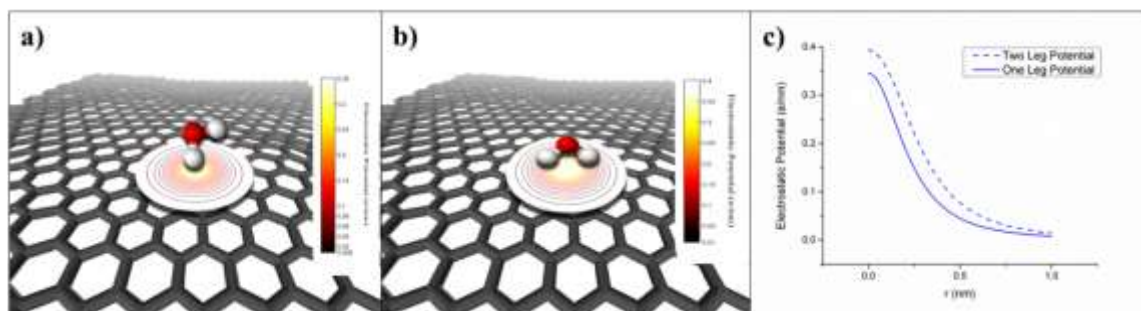


Figure 4.16: Schematics showing potential profile in the plane of the graphene sheet from one water molecule with a) one-leg and b) two-leg water orientations. c) Electrostatic potential as a function of distance on graphene from one-leg and two-leg water orientations.

When polar molecules are added, they act to solvate the water impurity, as shown with acetone molecules in Figure 4.17a. For acetone and other polar molecules, this results in a reduction of the potential magnitude in the graphene plane caused by water (Figure 4.17b). Figure 4.17c reveals that the polar molecules actually change the potential in the graphene plane induced by the water from positive to negative potential.

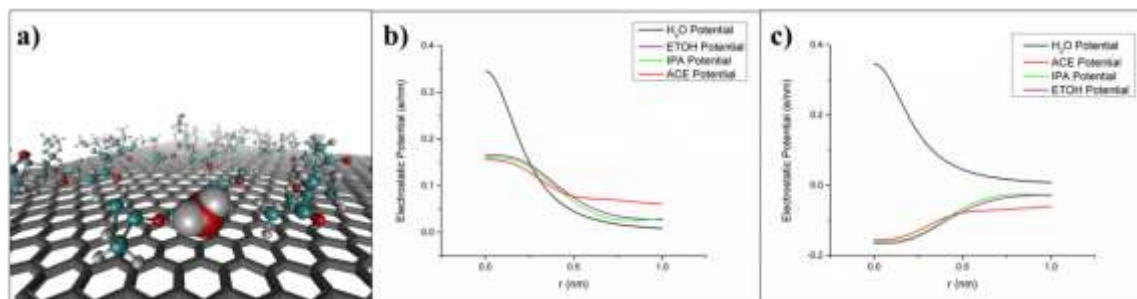


Figure 4.17: a) A system containing 50 acetone molecules, a water molecule impurity, and a graphene sheet. b) Absolute value of potential from one-leg water orientation both alone and with various polar molecules. c) Change in potential caused by polar molecules for water.

Nevertheless, the magnitude of potential reduction by polar molecules does correlate with their respective calculated dipole moments (Figure 4.17c and Figure 4.18), and thus supports both our previous experimental data and hypothesis that it is the polar nature of these molecules which acts to mitigate charge scattering effects of impurities on graphene via a reduction of their electrostatic potential [45]. However, the reversal in potential sign from positive to negative indicates a more complex process, which we will discuss later.

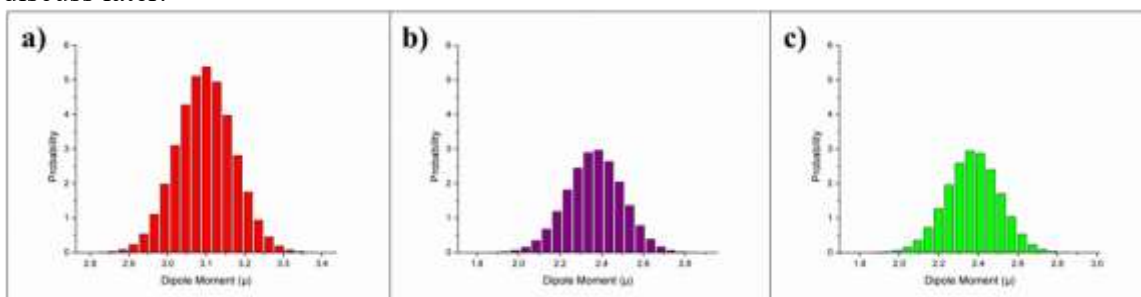


Figure 4.18: Normalized probability distributions of calculated dipole moment values for a) methanol, b) ethanol, and c) IPA molecules.

As was the case with polar molecules and a sodium ion impurity on graphene, we observed two mechanisms apparently governing the polar molecules' reduction in water impurity electrostatic potential in the plane of the graphene sheet. For acetone molecules, the magnitude of potential reduction, along with the contribution of both water displacement and electrostatic screening mechanisms, is shown in Figure 4.19a. The percentage contribution that each mechanism makes to the total potential reduction is shown as a function of distance in Figure 4.19b. Displacement of the water impurity appears to be a significant mechanism for potential reduction at short range, and screening becomes the dominant mechanism at distance beyond about 0.26 nm. However, we note that, as compared to displacement and screening mechanism percentage contributions for potential reduction in the case of acetone molecules and a sodium ion

impurity, the percentage contributions of the mechanisms for potential reduction in the case of acetone molecules and a water impurity are significantly more balanced at close range. So, while screening remains the dominant mechanism at long range, displacement of a water impurity is not as dominant at short range.

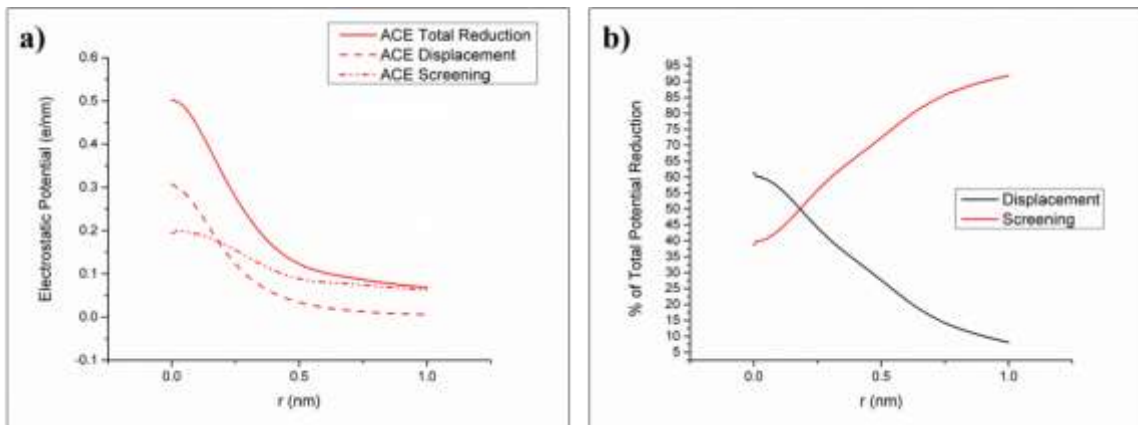


Figure 4.19: a) Potential plot showing the magnitude of potential reduction for an adsorbed water molecule impurity by acetone molecules (solid line), contribution of displacement mechanism to this potential reduction (dashed line), and contribution of screening mechanism (dot-dot-dashed line). b) Percentage contribution of each mechanism to the potential reduction.

To investigate why displacement of a water impurity appears to have reduced impact as compared with displacement of a sodium ion by the same acetone molecules, we varied the number of acetone molecules used in the simulation. We repeated the 50-molecule acetone simulation with numbers of 10 and 25 molecules per unit cell. As shown in Figure 4.20a, greater numbers of acetone molecules provide greater magnitudes of potential reduction. However, there is not an apparent trend in effects of the number of acetone molecules on displacement of water (Figure 4.20b), and acetone molecules do not appear to form distinct, successive solvation shells beyond the first one (Figure 4.20c). This difference in displacement trends for acetone with a water impurity versus

with a sodium ion impurity further hints at greater complexity in the mechanisms behind water impurity potential reduction.

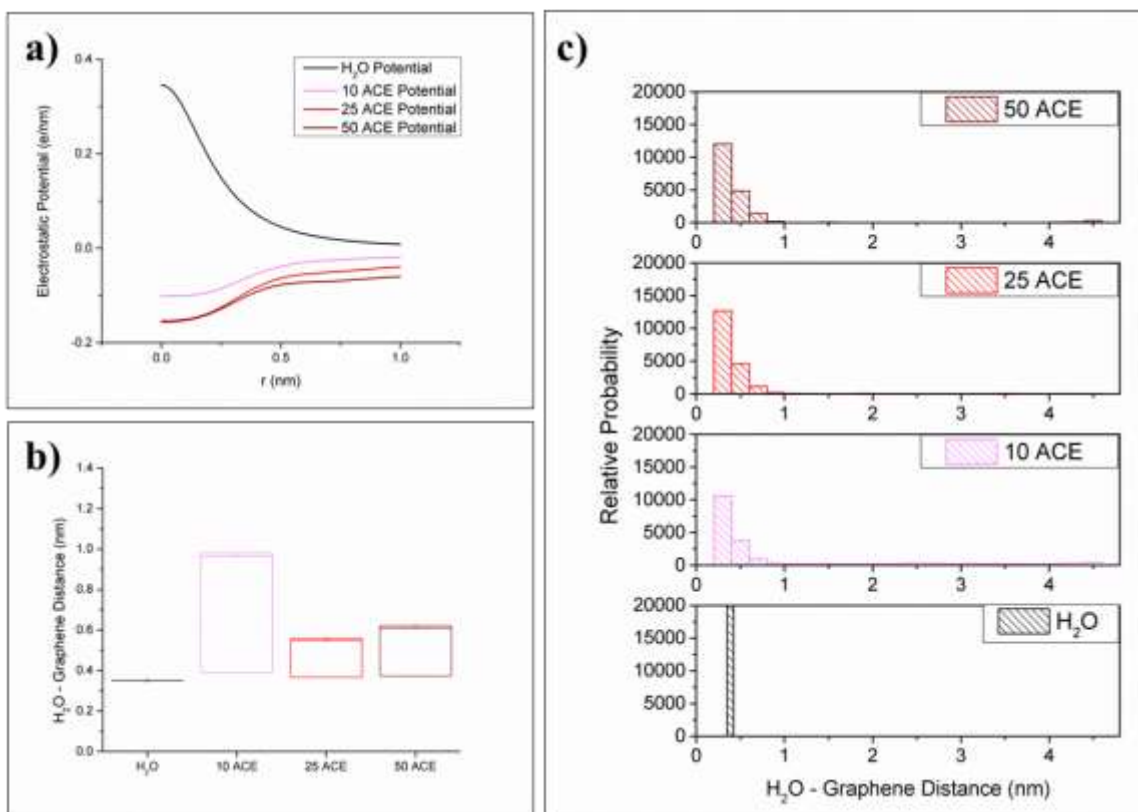


Figure 4.20: a) Potential plots for water alone and with various numbers of acetone molecules. b) Box plots showing mean displacement (small square) of water away from graphene as a function number of acetone molecules, with standard error (larger box boundaries). c) Distributions of values of water displacement by acetone molecules, indicating formation of only one solvation shell around water.

For similar data with ethanol molecules, see Figure 4.21. As with acetone molecules, greater numbers of ethanol molecules provide greater magnitudes of water potential profile reduction (Figure 4.21a). Again, there is not an apparent trend in effects of the number of ethanol molecules on displacement of water (Figure 4.21b). Figure

4.21c shows that the ethanol molecules do not appear to form distinct, successive solvation shells beyond the first shell. The results are qualitatively similar to those results with acetone molecules around a water impurity. This similarity does lend support to our assertion that these effects are due to the general polar nature of the molecules, and are not unique to acetone molecules alone.

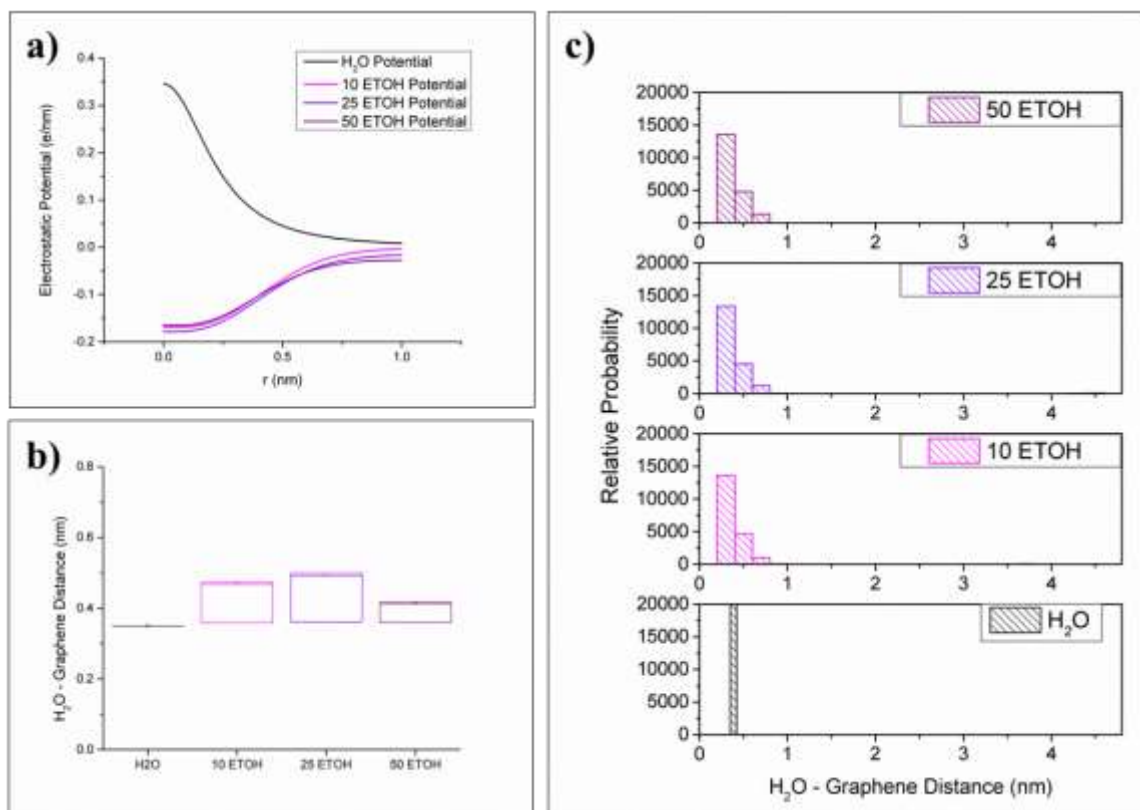


Figure 4.21: a) Electrostatic potential in the plane of the graphene sheet from water both alone and with various numbers of ethanol molecules. b) Box plots showing mean displacement (small square) of water away from graphene as a function of the number of ethanol molecules, with standard error (larger box boundaries). c) Distributions of values of water displacement by ethanol molecules, indicating formation of only one solvation shell around water.

When considering both the change in sign of the potential and limited displacement of the water impurity upon introduction of polar molecules, the strict, two-mechanism hypothesis is not sufficient to explain the impurity potential change. Hence, it is instructive to consider the dipolar nature of the water molecule (and, by extension, the molecular dipole class of impurity on graphene), and observe how the orientation of the water molecule changes in the presence of polar molecules. Thus far, our data considered the water molecule to be locked into the preferred one-leg orientation atop graphene, as it is in the solvent-free reference geometry. However, Figure 4.22a, a plot of the cosine of the angle between the water molecule bisector, or dipole vector, and the z-axis above the x-y graphene plane, illustrates how acetone molecules change the preferred orientation of the water molecule atop graphene. Where the angle cosine is -1, the water hydrogen atoms are pointed down toward the graphene. At angle cosine 0, the water has hydrogen atoms and oxygen atom parallel to the graphene sheet, and, at angle cosine +1, the hydrogens are pointing away from the sheet. We note that the simulation ensemble shows that the acetone molecules orient the water such that it is most probable to have the oxygen atom pointing more toward (and hydrogens pointing away from) the graphene sheet. This orientation is more likely to cause a negative potential in the plane of the graphene sheet, as is seen in Figure 4.22c. Additionally, ethanol (Figure 4.22b) and IPA (Figure 4.22c) molecules tend to orient the water molecule parallel to the sheet, with some skew toward oxygen facing down, and this helps explain the less negative potential observed for alcohols versus acetone plots in Figure 4.17c.

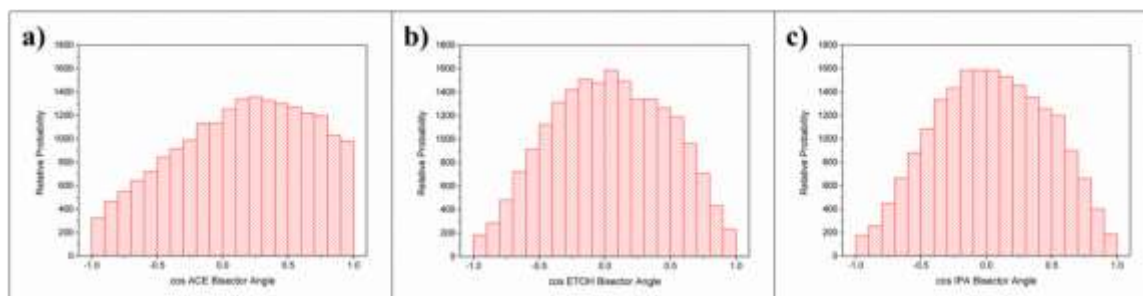


Figure 4.22: Distributions of values of the angle between water dipole vector and z-axis above graphene sheet in the presence of a) acetone b) ethanol c) IPA molecules. Angle cosine -1: water hydrogens are pointed down toward the graphene. Angle cosine 0: the water hydrogens and oxygen atoms parallel to graphene. Angle cosine +1: hydrogens are pointing away from the graphene.

As mentioned earlier, all of these simulations and calculations performed with the one-leg water molecule orientation were also performed with the two-leg water orientation and various additional polar molecules. As numerous groups have discussed, the orientation of the water molecule is an important factor to consider [97, 98, 103, 166-168]. Thus, the extents to which polar molecules cause reduction of the potential profile magnitude in the graphene plane caused by the two-leg orientation of water is shown in Figure 4.23a. Figure 4.23b reveals that the polar molecules actually change the potential in the graphene plane induced by the water from positive to negative potential. The magnitude of potential reduction, along with the contribution of both water displacement and electrostatic screening mechanisms, is shown in Figure 4.23c. The percentage contribution that each mechanism makes to the total potential reduction is shown as a function of distance in Figure 4.23d. These results are qualitatively similar to those for the one-leg water orientation discussed above.

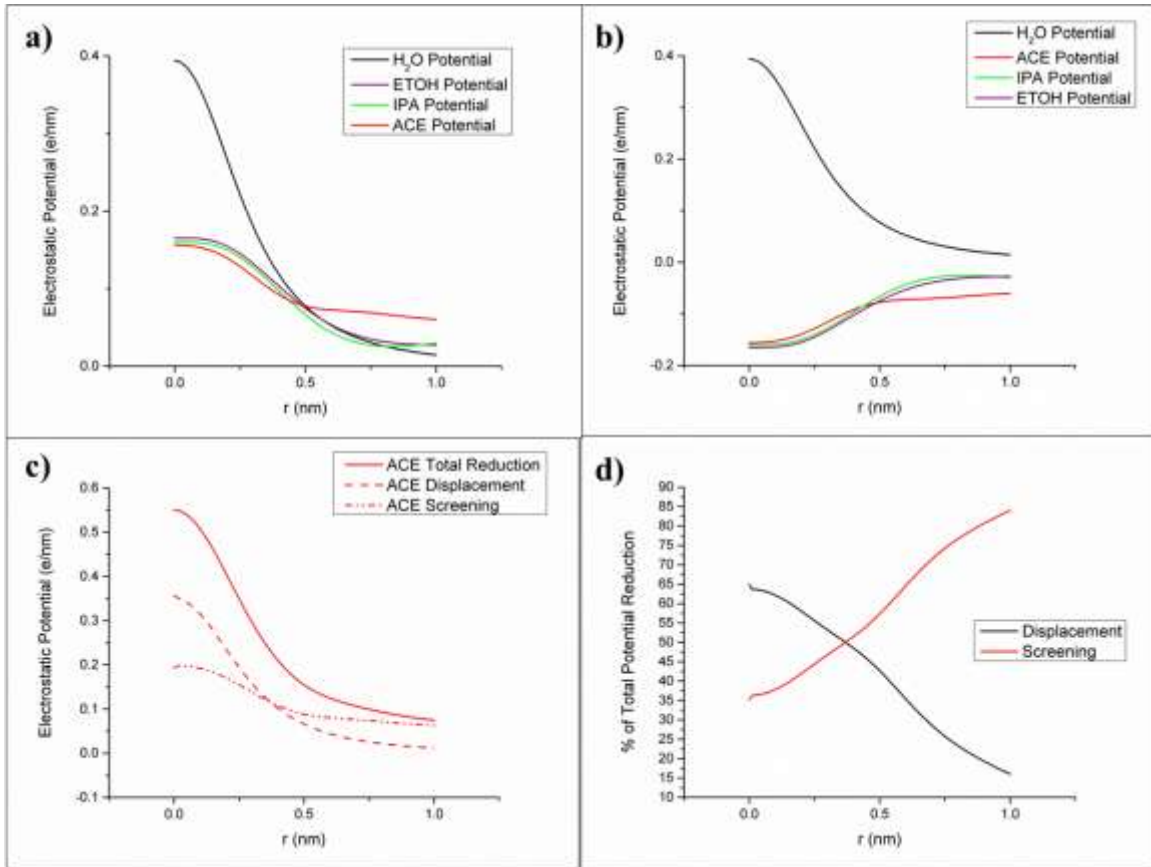


Figure 4.23: a) Absolute value of potential from two-leg water orientation both alone and with various polar molecules. b) Change in potential caused by polar molecules for water. c) Electrostatic potential in the plane of the graphene sheet from water impurity showing the magnitude of potential reduction by acetone molecules (solid line), contribution of displacement mechanism to this potential reduction (dashed line), and contribution of screening mechanism (dot-dot-dashed line). d) Percentage contribution of each mechanism to the potential reduction.

This theoretical work strongly supports our previous experimental efforts to show that it is not difficult to both access the impurities/defects in 2-D monolayer graphene and manipulate them in order to improve transport characteristics. Access to these 2-D material impurities/defects presents a distinct advantage for such materials over

comparable bulk conductive materials. While manipulation of impurities/defects with polar molecules is a good method for graphene, there may be other modification methods more appropriate for other 2-D materials such as MoS<sub>2</sub>.

#### **4.4 SUMMARY OF MOLECULAR DYNAMICS SIMULATIONS**

We have used both a sodium ion near graphene as a general model for a point charge impurity, and a water molecule near graphene as representative of any type of molecular dipole impurity. Such impurities in real graphene samples scatter charge carriers moving through the graphene, to the detriment of graphene electrical properties. It follows from our simulations that the magnitude of such impurity scattering should scale with the magnitude of the electrostatic potential in the graphene plane from that impurity. As we have demonstrated theoretically, polar molecules reduce that electrostatic potential via simple mechanisms. In the case of a point charge, physical displacement and electrostatic screening are sufficient mechanisms to greatly reduce the potential. While displacement is more important for potential reduction at short range, screening dominates at long range from the impurity. For a molecular dipole, displacement, screening, and reorientation of the impurity are responsible for potential reduction. Despite the added complexity of the displacement and reorientation mechanisms, electrostatic screening of the water impurity by polar molecules does dominate the potential reduction at longer range from the impurity. This reduction in impurity potential on graphene strongly supports our previous experimental observations that polar molecules mitigate the effects of charged impurities on graphene, which was observed as improvement in graphene device characteristics.

## Chapter 5: Future Work

We have studied methods to improve the electrical properties of graphene which could be more easily interfaced with existing semiconductor industry processes, and performed model experiments and simulations to improve our understanding of the chemical interactions governing the improvements. Contamination of or damage to graphene is difficult to avoid in graphene growth and processing. The charged impurities and defects which incorporate in/around graphene as a result of this processing degrade the electrical properties by scattering of charge carriers. We attribute the improvements to graphene device electrical properties to mitigation of charged impurities and defects by polar molecules, both in thin-film and vapor-phase forms. Our simulations indicate that polar gas molecules favor interaction with impure or defective graphene over pristine graphene. We also found that charged impurities such as sodium ions or water molecules create an electrostatic potential profile in the plane of a graphene sheet with which they are in contact. Polar molecules such as acetone act to reduce this potential profile by two mechanisms: First, the polar molecules physically displace the impurities away from the graphene sheet. Second, the dipoles of the polar molecules orient the molecules around the impurities to electrostatically mitigate the impurities' charges or dipoles.

### 5.1 EXPERIMENTAL

We have demonstrated that testing of graphene devices with polar vapor molecules is a good system for qualitative determination of the polar molecules impact on the general class of charge scatterers on and around graphene. Future experiments with graphene devices and polar vapor molecules which both take place in a temperature-controlled vacuum chamber and involve a range of specific concentrations of polar vapor molecules with a broad range of dipole moments would allow for more quantitative

determination of how the degree of polarity of various vapor molecules mitigates charge scattering in graphene. Such an experimental setup would also allow for addressing specific groups of charged impurities and defects on graphene. Various groups have reported removal of adsorbed water and oxygen from graphene upon temperature and vacuum treatment [41, 95, 119, 169]. Eliminating adsorbed impurities would narrow down the possible sources of charge scattering to substrate impurities, substrate defects, and graphene defects. Suspension of graphene has been demonstrated to improve its electrical properties due to removal of the substrate charge scattering effects [10, 40, 115, 124].

These experiments could also be applied to other 2D materials, including MoS<sub>2</sub> and graphene nanoribbons. MoS<sub>2</sub> is an interesting 2D material to study, due to the prevalence of sulphur atom vacancies, which result in lower-than-expected mobility and n-doped electrical characteristics [170, 171]. Yu, *et al.* used SAMs of (3-mercaptopropyl) trimethoxysilane, with thiol end groups, to repair such vacancies and reduce charged impurity scattering effects [172]. Further study of SAMs with specific dipole moments and end groups could allow precise tuning of MoS<sub>2</sub> properties. Graphene nanoribbons are also of interest due to their band gap advantage over graphene, and their higher concentrations of charged defects and impurities due to edge roughness [126, 173, 174]. The greater numbers of charged impurities and defects present per given area of graphene nanoribbon versus graphene sheets would allow for quantitative comparison of the extent to which various polar molecules mitigate charge scattering on different concentrations of charged impurities and defects per area.

## 5.2 COMPUTATIONAL

In conjunction with the experiments above, computational studies of molecular dipole moments, polarizabilities, and binding strengths with various forms of graphene and other 2D materials would help understand qualitatively the chemical interactions. We have used Gaussian software to calculate molecule dipole moments and binding strengths with GGA DFT methods. However, DFT is a constantly evolving field, and newer functionals and basis sets have been developed which may provide more accurate calculations. In 2013, Lazar and coworkers studied adsorption of organic molecules on graphene using DFT, wave-functional theory, and empirical calculations [141]. They found that the optB88-vdW functional used in ab initio molecular dynamics calculated adsorption enthalpies in the best agreement with experimental data. Recently, Cavallucci and Tozzini found that proper modeling of graphene on a SiC substrate must include van der Waals (vdW) corrections in DFT calculations [175]. However, the empirical dispersion correction to the traditional PBE exchange/correlation functional, PBE-D2 [176], used by the authors was found to become less accurate at predicting room temperature energies. Okamoto used DFT to study insertion and adsorption of lithium in graphene with and without carbon vacancies [177]. The author asserted that, where vdW forces are less important, as in strong ionic adsorption without a substrate under graphene, the GGA PBE methods were sufficient. Many computational researchers of graphene use software other than Gaussian, including Quantum Espresso [178], GAMESS [179], and CASTEP [180]. Such programs may better take into account the solid-state (as opposed to molecular) properties of graphene including periodicity, electronic band structure, and density of states. Our molecular dynamics studies using GROMACS could also be applied to MoS<sub>2</sub> and other 2D materials to better understand

the mechanisms governing mitigation of the effects of charged impurities and defects by polar molecules and SAMs on those materials.

## References

1. Wallace, P.R., *The Band Theory of Graphite*. Physical Review, 1947. **71**(9): p. 622-634.
2. Novoselov, K.S., et al., *Electric Field Effect in Atomically Thin Carbon Films*. Science, 2004. **306**(5696): p. 666-669.
3. Novoselov, K.S., et al., *Two-Dimensional Atomic Crystals*. Proceedings of the National Academy of Sciences of the United States of America, 2005. **102**(30): p. 10451-10453.
4. Novoselov, K.S., et al., *Two-Dimensional Gas of Massless Dirac Fermions in Graphene*. Nature, 2005. **438**(7065): p. 197-200.
5. Ferrari, A.C., et al., *Raman Spectrum of Graphene and Graphene Layers*. Physical Review Letters, 2006. **97**(18): p. 187401.
6. Geim, A.K. and K.S. Novoselov, *The Rise of Graphene*. Nature Materials, 2007. **6**(3): p. 183-191.
7. Morozov, S.V., et al., *Giant Intrinsic Carrier Mobilities in Graphene and Its Bilayer*. Physical Review Letters, 2008. **100**(1): p. 016602.
8. Zhang, Y., et al., *Experimental Observation of the Quantum Hall Effect and Berry's Phase in Graphene*. Nature, 2005. **438**(7065): p. 201-204.
9. Tan, Y.W., et al., *Measurement of Scattering Rate and Minimum Conductivity in Graphene*. Physical Review Letters, 2007. **99**(24): p. 246803.
10. Bolotin, K.I., et al., *Ultrahigh Electron Mobility in Suspended Graphene*. Solid State Communications, 2008. **146**(9-10): p. 351-355.
11. Ando, T., *Screening Effect and Impurity Scattering in Monolayer Graphene*. Journal of the Physical Society of Japan, 2006. **75**(7): p. 074716.
12. Castro Neto, A.H., et al., *The Electronic Properties of Graphene*. Reviews of Modern Physics, 2009. **81**(1): p. 109-162.
13. Lee, J., et al., *Embedded-Gate Graphene Transistors for High-Mobility Detachable Flexible Nanoelectronics*. Applied Physics Letters, 2012. **100**(15): p. 152104.
14. Lin, Y.M., et al., *100-GHz Transistors from Wafer-Scale Epitaxial Graphene*. Science, 2010. **327**(5966): p. 662-662.

15. Meric, I., et al., *Current Saturation in Zero-Bandgap, Top-Gated Graphene Field-Effect Transistors*. Nature Nanotechnology, 2008. **3**(11): p. 654-659.
16. Xia, F., et al., *Graphene Field-Effect Transistors with High On/Off Current Ratio and Large Transport Band Gap at Room Temperature*. Nano Letters, 2010. **10**(2): p. 715-718.
17. Banerjee, S.K., et al., *Graphene for CMOS and Beyond CMOS Applications*. Proceedings of the IEEE, 2010. **98**(12): p. 2032-2046.
18. Chen, P.Y., et al., *Graphene-Based Plasmonic Platform for Reconfigurable Terahertz Nanodevices*. ACS Photonics, 2014. **1**(8): p. 647-654.
19. Wang, L., et al., *Highly Sensitive and Wide-Band Tunable Terahertz Response of Plasma Waves Based on Graphene Field Effect Transistors*. Scientific Reports, 2014. **4**.
20. Lemme, M.C., et al., *Mobility in Graphene Double Gate Field Effect Transistors*. Solid-State Electronics, 2008. **52**(4): p. 514-518.
21. Wu, Y., et al., *State-of-the-Art Graphene High-Frequency Electronics*. Nano Letters, 2012. **12**(6): p. 3062-3067.
22. Jongho, L., et al. *State-of-the-art Graphene Transistors on Hexagonal Boron Nitride, High-k, and Polymeric Films for GHz Flexible Analog Nanoelectronics*. in *Electron Devices Meeting (IEDM), 2012 IEEE International*. 2012.
23. Ha, T.-J., D. Akinwande, and A. Dodabalapur, *Hybrid Graphene/organic Semiconductor Field-Effect Transistors*. Applied Physics Letters, 2012. **101**: p. 033309-1 - 033309-3.
24. Lee, J., et al., *25 GHz Embedded-Gate Graphene Transistors with High-K Dielectrics on Extremely Flexible Plastic Sheets*. ACS Nano, 2013. **7**(9): p. 7744-7750.
25. Lee, J., et al., *High-Performance Current Saturating Graphene Field-Effect Transistor With Hexagonal Boron Nitride Dielectric on Flexible Polymeric Substrates*. IEEE Electron Device Letters, 2013. **34**(2): p. 172-174.
26. Ha, T.J., et al., *Graphene/fluoropolymer Hybrid Materials with Enhancement of All Device Properties for Improved Field-Effect Transistors*. 2013 IEEE International Electron Devices Meeting (IEDM), 2013.

27. Lee, J., et al., *High-Performance Flexible Nanoelectronics: 2D Atomic Channel Materials for Low-Power Digital and High-Frequency Analog Devices*. 2013 Ieee International Electron Devices Meeting (Iedm), 2013.
28. Rahimi, S., et al., *Toward 300 mm Wafer-Scalable High-Performance Polycrystalline Chemical Vapor Deposited Graphene Transistors*. ACS Nano, 2014.
29. Yogeesh, M.N., et al., *Towards the Realization of Graphene Based Flexible Radio Frequency Receiver*. Electronics, 2015. **4**(4): p. 933-946.
30. Zhu, Y., et al., *Graphene and Graphene Oxide: Synthesis, Properties, and Applications*. Advanced Materials, 2010. **22**(35): p. 3906-3924.
31. Cooper, D.R., et al., *Experimental Review of Graphene*. International Scholarly Research Notices, International Scholarly Research Notices, 2012. **2012**, **2012**: p. e501686.
32. Chan, J., et al., *Reducing Extrinsic Performance-Limiting Factors in Graphene Grown by Chemical Vapor Deposition*. ACS Nano, 2012. **6**(4): p. 3224-3229.
33. Chen, J.-H., et al., *Intrinsic and Extrinsic Performance Limits of Graphene Devices on SiO<sub>2</sub>*. Nature Nanotechnology, 2008. **3**(4): p. 206-209.
34. Chen, J.H., et al., *Charged-Impurity Scattering in Graphene*. Nature Physics, 2008. **4**(5): p. 377-381.
35. Chen, F., et al., *Dielectric Screening Enhanced Performance in Graphene FET*. Nano Letters, 2009. **9**(7): p. 2571-2574.
36. Chen, J.H., et al., *Diffusive Charge Transport in Graphene on SiO<sub>2</sub>*. Solid State Communications, 2009. **149**(27-28): p. 1080-1086.
37. Chen, J.H., et al., *Defect Scattering in Graphene*. Physical Review Letters, 2009. **102**(23).
38. Fratini, S. and F. Guinea, *Substrate Limited Electron Dynamics in Graphene*. Physical Review B, 2008. **77**(19).
39. Jang, C., et al., *Tuning the Effective Fine Structure Constant in Graphene: Opposing Effects of Dielectric Screening on Short- and Long-Range Potential Scattering*. Physical Review Letters, 2008. **101**(14): p. 146805.

40. Newaz, A.K.M., et al., *Probing Charge Scattering Mechanisms in Suspended Graphene by Varying Its Dielectric Environment*. Nature Communications, 2012. **3**: p. 734.
41. Wang, H., et al., *Hysteresis of Electronic Transport in Graphene Transistors*. ACS Nano, 2010. **4**(12): p. 7221-7228.
42. Zhu, W., et al., *Carrier Scattering, Mobilities, and Electrostatic Potential in Monolayer, Bilayer, and Trilayer Graphene*. Physical Review B, 2009. **80**(23): p. 235402.
43. Ha, T.-J., et al., *Transformation of the Electrical Characteristics of Graphene Field-Effect Transistors with Fluoropolymer*. ACS Applied Materials & Interfaces, 2013. **5**(1): p. 16-20.
44. Ha, T.J., et al., *The Restorative Effect of Fluoropolymer Coating on Electrical Characteristics of Graphene Field-Effect Transistors*. IEEE Electron Device Letters, 2013. **34**(4): p. 559-561.
45. Worley, B.C., et al., *Dramatic Vapor-Phase Modulation of the Characteristics of Graphene Field-Effect Transistors*. Physical Chemistry Chemical Physics, 2015. **17**(28): p. 18426-18430.
46. Hwang, E.H., S. Adam, and S. Das Sarma, *Carrier Transport in Two-Dimensional Graphene Layers*. Physical Review Letters, 2007. **98**(18): p. 186806.
47. Adam, S., et al., *A Self-Consistent Theory for Graphene Transport*. Proceedings of the National Academy of Sciences, 2007. **104**(47): p. 18392-18397.
48. Suk, J.W., et al., *Enhancement of the Electrical Properties of Graphene Grown by Chemical Vapor Deposition via Controlling the Effects of Polymer Residue*. Nano Letters, 2013. **13**(4): p. 1462-1467.
49. Chowdhury, S.F., et al., *Improvement of Graphene Field-Effect Transistors by Hexamethyldisilazane Surface Treatment*. Applied Physics Letters, 2014. **105**(3): p. 033117.
50. Lupina, G., et al., *Residual Metallic Contamination of Transferred Chemical Vapor Deposited Graphene*. ACS Nano, 2015. **9**(5): p. 4776-4785.
51. Ambrosi, A. and M. Pumera, *The CVD Graphene Transfer Procedure Introduces Metallic Impurities which Alter the Graphene Electrochemical Properties*. Nanoscale, 2013. **6**(1): p. 472-476.

52. Dean, C.R., et al., *Boron Nitride Substrates for High-Quality Graphene Electronics*. Nature Nanotechnology, 2010. **5**(10): p. 722-726.
53. Yokota, K., K. Takai, and T. Enoki, *Carrier Control of Graphene Driven by the Proximity Effect of Functionalized Self-assembled Monolayers*. Nano Letters, 2011. **11**(9): p. 3669-3675.
54. Guo, B., et al., *Controllable N-Doping of Graphene*. Nano Letters, 2010. **10**(12): p. 4975-4980.
55. Yan, Z., et al., *Controlled Modulation of Electronic Properties of Graphene by Self-Assembled Monolayers on SiO<sub>2</sub> Substrates*. ACS Nano, 2011. **5**(2): p. 1535-1540.
56. Wang, X.H., et al., *Direct Delamination of Graphene for High-Performance Plastic Electronics*. Small, 2014. **10**(4): p. 694-698.
57. Cernetic, N., et al., *Influence of Self-Assembled Monolayer Binding Group on Graphene Transistors*. Applied Physics Letters, 2015. **106**(2): p. 021603.
58. Liu, Z., A.A. Bol, and W. Haensch, *Large-Scale Graphene Transistors with Enhanced Performance and Reliability Based on Interface Engineering by Phenylsilane Self-Assembled Monolayers*. Nano Letters, 2011. **11**(2): p. 523-528.
59. Robinson, J.T., et al., *Properties of Fluorinated Graphene Films*. Nano Letters, 2010. **10**(8): p. 3001-3005.
60. Lee, W.H., et al., *Selective-Area Fluorination of Graphene with Fluoropolymer and Laser Irradiation*. Nano Letters, 2012. **12**(5): p. 2374-2378.
61. Newton, L., et al., *Self Assembled Monolayers (SAMs) on Metallic Surfaces (Gold and Graphene) for Electronic Applications*. Journal of Materials Chemistry C, 2012. **1**(3): p. 376-393.
62. Wang, B., et al., *Support-Free Transfer of Ultrasoother Graphene Films Facilitated by Self-Assembled Monolayers for Electronic Devices and Patterns*. ACS Nano, 2016. **10**(1): p. 1404-10.
63. Cernetic, N., et al., *Systematic Doping Control of CVD Graphene Transistors with Functionalized Aromatic Self-Assembled Monolayers*. Advanced Functional Materials, 2014. **24**(22): p. 3464-3470.
64. Lee, W.H., et al., *Simultaneous Transfer and Doping of CVD-Grown Graphene by Fluoropolymer for Transparent Conductive Films on Plastic*. ACS Nano, 2012. **6**(2): p. 1284-1290.

65. Worley, B.C., et al., *Chemical Understanding of the Mechanisms Involved in Mitigation of Charged Impurity Effects by Polar Molecules on Graphene*. Journal of Physical Chemistry C, 2016. **120**(23): p. 12909 - 12916.
66. Heyrovska, R., *Atomic Structures of Graphene, Benzene and Methane with Bond Lengths as Sums of the Single, Double and Resonance Bond Radii of Carbon*. arXiv:0804.4086 [physics], 2008.
67. Wong, H.S.P. and D. Akinwande, *Carbon Nanotube and Graphene Device Physics* 2011: Cambridge University Press. 263.
68. Klymkowsky, M.M.C.M.W. *Chemistry, Life, the Universe & Everything*. 2016 [cited 2016 6-20-2016]; Available from: <http://virtuallaboratory.colorado.edu/CLUE-Chemistry/readings/CLUE.pdf>.
69. Phillip. *Why does the energy gap for  $\pi - \pi^*$  transitions shrink with the size of the  $\pi$ -conjugated system?* 2014 [cited 2016 6-20-2016]; Available from: <http://chemistry.stackexchange.com/questions/8910/why-does-the-energy-gap-for-%CF%80-%CF%80-transitions-shrink-with-the-size-of-the-pi-co>.
70. Ishii, H., et al., *Energy Level Alignment and Interfacial Electronic Structures at Organic/Metal and Organic/Organic Interfaces*. Advanced Materials, 1999. **11**(8): p. 605-625.
71. Ando, T., *The Electronic Properties of Graphene and Carbon Nanotubes*. NPG Asia Materials, 2009. **1**(1): p. 17-21.
72. Das Sarma, S., et al., *Electronic Transport in Two-Dimensional Graphene*. Reviews of Modern Physics, 2011. **83**(2): p. 407-470.
73. Andrei, E.Y., G. Li, and X. Du, *Electronic Properties of Graphene: A Perspective from Scanning Tunneling Microscopy and Magnetotransport*. Reports on Progress in Physics, 2012. **75**(5): p. 056501.
74. Nomura, K. and A.H. MacDonald, *Quantum Transport of Massless Dirac Fermions*. Physical Review Letters, 2007. **98**(7): p. 076602.
75. Bostwick, A., et al., *Quasiparticle Dynamics in Graphene*. Nature Physics, 2007. **3**(1): p. 36-40.
76. Peres, N.M.R., *Colloquium: The Transport Properties of Graphene: An Introduction*. Reviews of Modern Physics, 2010. **82**(3): p. 2673-2700.
77. Schwierz, F., *Graphene Transistors*. Nature Nanotechnology, 2010. **5**(7): p. 487-496.

78. Lin, Y.-M., et al., *Dual-Gate Graphene FETs With of 50 GHz*. IEEE Electron Device Letters, 2010. **31**(1): p. 68-70.
79. Ganwani, N., *FM Embedded Antennas*, 2010, University of Texas: Austin, Tex. p. 1 online resource (xi, 36 leaves).
80. Han, S.-J., et al., *Graphene Radio Frequency Receiver Integrated Circuit*. Nature Communications, 2014. **5**: p. 3086.
81. Parrish, K.N., *Nanoscale Graphene for RF Circuits and Systems*. 1 online resource (xxvi, 140 leaves).
82. Lin, Y.-M., et al., *Operation of Graphene Transistors at Gigahertz Frequencies*. Nano Letters, 2009. **9**(1): p. 422-426.
83. Long, M.-Q., et al., *Theoretical Predictions of Size-Dependent Carrier Mobility and Polarity in Graphene*. Journal of the American Chemical Society, 2009. **131**(49): p. 17728-17729.
84. Banszerus, L., et al., *Ultrahigh-Mobility Graphene Devices from Chemical Vapor Deposition on Reusable Copper*. Science Advances, 2015. **1**(6): p. e1500222.
85. Li, X., et al., *Large-Area Synthesis of High-Quality and Uniform Graphene Films on Copper Foils*. Science, 2009. **324**(5932): p. 1312-1314.
86. Tao, L., et al., *Synthesis of High Quality Monolayer Graphene at Reduced Temperature on Hydrogen-Enriched Evaporated Copper (111) Films*. ACS Nano, 2012. **6**(3): p. 2319-2325.
87. Wang, D.-Y., et al., *Clean-Lifting Transfer of Large-area Residual-Free Graphene Films*. Advanced Materials, 2013. **25**(32): p. 4521-4526.
88. Lin, Y.-C., et al., *Clean Transfer of Graphene for Isolation and Suspension*. ACS Nano, 2011. **5**(3): p. 2362-2368.
89. Wang, Y., et al., *Electrochemical Delamination of CVD-Grown Graphene Film: Toward the Recyclable Use of Copper Catalyst*. ACS Nano, 2011. **5**(12): p. 9927-9933.
90. Chandrashekar, B.N., et al., *Roll-to-Roll Green Transfer of CVD Graphene onto Plastic for a Transparent and Flexible Triboelectric Nanogenerator*. Advanced Materials, 2015. **27**(35): p. 5210-5216.
91. Gao, L., et al., *Face-to-face transfer of wafer-scale graphene films*. Nature, 2014. **505**(7482): p. 190-194.

92. Pantelides, S.T., et al., *Defects and Doping and Their Role in Functionalizing Graphene*. MRS Bulletin, 2012. **37**(12): p. 1187-1194.
93. Cabrera-Sanfelix, P., *Adsorption and Reactivity of CO<sub>2</sub> on Defective Graphene Sheets*. The Journal of Physical Chemistry A, 2009. **113**(2): p. 493-498.
94. Xu, H., et al., *Investigating the Mechanism of Hysteresis Effect in Graphene Electrical Field Device Fabricated on SiO<sub>2</sub> Substrates using Raman Spectroscopy*. Small, 2012. **8**(18): p. 2833-2840.
95. Park, J., et al., *Work-Function Engineering of Graphene Electrodes by Self-Assembled Monolayers for High-Performance Organic Field-Effect Transistors*. The Journal of Physical Chemistry Letters, 2011. **2**(8): p. 841-845.
96. Wehling, T.O., et al., *Molecular doping of graphene*. Nano Letters, 2008. **8**(1): p. 173-177.
97. Wehling, T.O., A.I. Lichtenstein, and M.I. Katsnelson, *First-Principles Studies of Water Adsorption on Graphene: The Role of the Substrate*. Applied Physics Letters, 2008. **93**(20): p. 202110.
98. Leenaerts, O., B. Partoens, and F.M. Peeters, *Adsorption of H<sub>2</sub>O, NH<sub>3</sub>, CO, NO<sub>2</sub>, and NO on Graphene: A First-Principles Study*. Physical Review B, 2008. **77**(12): p. 125416.
99. Sabio, J., et al., *Electrostatic Interactions between Graphene Layers and Their Environment*. Physical Review B, 2008. **77**(19): p. 195409.
100. Lafkioti, M., et al., *Graphene on a Hydrophobic Substrate: Doping Reduction and Hysteresis Suppression under Ambient Conditions*. Nano Letters, 2010. **10**(4): p. 1149-1153.
101. Lee, B., et al., *Modification of Electronic Properties of Graphene with Self-Assembled Monolayers*. Nano Letters, 2010. **10**(7): p. 2427-2432.
102. Moser, J., et al., *The Environment of Graphene Probed by Electrostatic Force Microscopy*. Applied Physics Letters, 2008. **92**(12): p. 123507.
103. Leenaerts, O., B. Partoens, and F.M. Peeters, *Water on Graphene: Hydrophobicity and Dipole Moment Using Density Functional Theory*. Physical Review B, 2009. **79**(23): p. 235440.

104. Umadevi, D. and G.N. Sastry, *Molecular and Ionic Interaction with Graphene Nanoflakes: A Computational Investigation of CO<sub>2</sub>, H<sub>2</sub>O, Li, Mg, Li<sup>+</sup>, and Mg<sup>2+</sup> Interaction with Polycyclic Aromatic Hydrocarbons*. The Journal of Physical Chemistry C, 2011. **115**(19): p. 9656-9667.
105. Wunsch, B., et al., *Dynamical Polarization of Graphene at Finite Doping*. New Journal of Physics, 2006. **8**(12): p. 318.
106. Hwang, E.H. and S. Das Sarma, *Dielectric Function, Screening, and Plasmons in Two-Dimensional Graphene*. Physical Review B, 2007. **75**(20): p. 205418.
107. Ho, T.A. and A. Striolo, *Polarizability Effects in Molecular Dynamics Simulations of the Graphene-Water Interface*. The Journal of Chemical Physics, 2013. **138**(5): p. 054117.
108. Chen, S., et al., *Adsorption/Desorption and Electrically Controlled Flipping of Ammonia Molecules on Graphene*. New Journal of Physics, 2010. **12**(12): p. 125011.
109. Lin, X., J. Ni, and C. Fang, *Adsorption capacity of H<sub>2</sub>O, NH<sub>3</sub>, CO, and NO<sub>2</sub> on the pristine graphene*. Journal of Applied Physics, 2013. **113**(3).
110. Srivastava, P.K. and S. Ghosh, *Defect Engineering as a Versatile Route to Estimate Various Scattering Mechanisms in Monolayer Graphene on Solid Substrates*. Nanoscale, 2015. **7**(38): p. 16079-16086.
111. Kim, J.S., et al., *Toward Air-Stable Multilayer Phosphorene Thin-Films and Transistors*. Scientific Reports, 2015. **5**.
112. Wang, X., et al., *High-Performance Graphene Devices on SiO<sub>2</sub>/Si Substrate Modified by Highly Ordered Self-Assembled Monolayers*. Advanced Materials, 2011. **23**(21): p. 2464-2468.
113. Avouris, P., *Graphene: Electronic and Photonic Properties and Devices*. Nano Letters, 2010. **10**(11): p. 4285-4294.
114. Kim, S., et al., *Realization of a High Mobility Dual-Gated Graphene Field-Effect Transistor with Al<sub>2</sub>O<sub>3</sub> Dielectric*. Applied Physics Letters, 2009. **94**(6): p. 062107.
115. Du, X., et al., *Approaching Ballistic Transport in Suspended Graphene*. Nature Nanotechnology, 2008. **3**(8): p. 491-495.
116. Fallahazad, B., et al., *Dielectric Thickness Dependence of Carrier Mobility in Graphene with HfO<sub>2</sub> Top Dielectric*. Applied Physics Letters, 2010. **97**(12): p. 1-3.

117. Mann, J.A. and W.R. Dichtel, *Noncovalent Functionalization of Graphene by Molecular and Polymeric Adsorbates*. The Journal of Physical Chemistry Letters, 2013. **4**(16): p. 2649-2657.
118. Duarte, D. and A. Dodabalapur, *Investigation of the Physics of Sensing in Organic Field Effect Transistor Based Sensors*. Journal of Applied Physics, 2012. **111**(4): p. 044509.
119. Schedin, F., et al., *Detection of Individual Gas Molecules Adsorbed on Graphene*. Nature Materials, 2007. **6**(9): p. 652-655.
120. Romero, H.E., et al., *Adsorption of Ammonia on Graphene*. Nanotechnology, 2009. **20**(24).
121. Duarte, D., A. Dodabalapur, and B.J. Holliday. *Sensing Mechanism in Receptor-Modified Organic Field Effect Transistor Based Vapor Sensors*. in *2011 IEEE Sensors*. 2011.
122. Nelson, R.D., D.R. Lide, and A.A. Maryott, *Selected Values of Electric Dipole Moments for Molecules in the Gas Phase*. NSRDS-NBS1967, Washington, D.C: U.S. Dept. of Commerce, National Bureau of Standards : For sale by the Supt. of Docs., U.S. G.P.O. 49.
123. Solís-Fernández, P., et al., *Gate-Tunable Dirac Point of Molecular Doped Graphene*. ACS Nano, 2016. **10**(2): p. 2930-2939.
124. Bolotin, K.I., et al., *Temperature-Dependent Transport in Suspended Graphene*. Physical Review Letters, 2008. **101**(9): p. 096802.
125. Dreyer, D.R., R.S. Ruoff, and C.W. Bielawski, *From Conception to Realization: An Historical Account of Graphene and Some Perspectives for Its Future*. Angewandte Chemie International Edition, 2010. **49**(49): p. 9336-9344.
126. Fang, T., et al., *Carrier Statistics and Quantum Capacitance of Graphene Sheets and Ribbons*. Applied Physics Letters, 2007. **91**(9): p. 092109.
127. Geim, A.K., *Graphene: Status and Prospects*. Science, 2009. **324**(5934): p. 1530-1534.
128. Ostrovsky, P.M., I.V. Gornyi, and A.D. Mirlin, *Electron Transport in Disordered Graphene*. Physical Review B, 2006. **74**(23): p. 235443.
129. Katsnelson, M.I., *Nonlinear Screening of Charge Impurities in Graphene*. Physical Review B, 2006. **74**(20): p. 201401.

130. Katsnelson, M.I. and A.K. Geim, *Electron Scattering on Microscopic Corrugations in Graphene*. Philosophical Transactions of the Royal Society of London A: Mathematical, Physical and Engineering Sciences, 2008. **366**(1863): p. 195-204.
131. Frisch, M.J., et al., *Gaussian 09*, 2009, Gaussian, Inc.: Wallingford, CT, USA.
132. Dennington, R.K., Todd; Millam, John., *GaussView*, 2009, Semichem Inc.: Shawnee Mission, KS.
133. Jensen, F., *Introduction to Computational Chemistry*. 2nd ed2007: Wiley. 599.
134. Perdew, J.P., K. Burke, and M. Ernzerhof, *Generalized Gradient Approximation Made Simple*. Physical Review Letters, 1996. **77**(18): p. 3865-3868.
135. Ray, S.J., *First-Principles Study of MoS<sub>2</sub>, Phosphorene and Graphene Based Single Electron Transistor for Gas Sensing Applications*. Sensors and Actuators B: Chemical, 2016. **222**: p. 492-498.
136. Perdew, J.P. and A. Zunger, *Self-Interaction Correction to Density-Functional Approximations for Many-Electron Systems*. Physical Review B, 1981. **23**(10): p. 5048-5079.
137. Ditchfield, R., W.J. Hehre, and J.A. Pople, *Self-Consistent Molecular-Orbital Methods. IX. An Extended Gaussian-Type Basis for Molecular-Orbital Studies of Organic Molecules*. The Journal of Chemical Physics, 1971. **54**(2): p. 724-728.
138. Ao, Z.M., et al., *Enhancement of CO Detection in Al Doped Graphene*. Chemical Physics Letters, 2008. **461**(4-6): p. 276-279.
139. Zhang, Y.-H., et al., *Improving Gas Sensing Properties of Graphene by Introducing Dopants and Defects: A First-Principles Study*. Nanotechnology, 2009. **20**(18): p. 185504.
140. Popov, I.A., K.V. Bozhenko, and A.I. Boldyrev, *Is Graphene Aromatic?* Nano Research, 2011. **5**(2): p. 117-123.
141. Lazar, P., et al., *Adsorption of Small Organic Molecules on Graphene*. Journal of the American Chemical Society, 2013. **135**(16): p. 6372-6377.
142. Schyman, P. and W.L. Jorgensen, *Exploring Adsorption of Water and Ions on Carbon Surfaces Using a Polarizable Force Field*. The Journal of Physical Chemistry Letters, 2013. **4**(3): p. 468-474.

143. Ishigami, M., et al., *Atomic Structure of Graphene on SiO<sub>2</sub>*. Nano Letters, 2007. 7(6): p. 1643-1648.
144. Hwang, E.H., S. Adam, and S. Das Sarma, *Transport in Chemically Doped Graphene in the Presence of Adsorbed Molecules*. Physical Review B, 2007. 76(19): p. 195421.
145. Ferrari, A.C., et al., *Science and Technology Roadmap for Graphene, Related Two-Dimensional Crystals, and Hybrid Systems*. Nanoscale, 2015. 7(11): p. 4598-4810.
146. Varshney, A., F.P. Brooks, and W.V. Wright, *Linearly Scalable Computation of Smooth Molecular Surfaces*. IEEE Computer Graphics and Applications, 1994. 14: p. 19-25.
147. Frishman, D. and P. Argos, *Knowledge-Based Secondary Structure Assignment*. Proteins: structure, function and genetics, 1995. 23: p. 566-579.
148. Sanner, M., A. Olsen, and J.-C. Spohner. *Fast and Robust Computation of Molecular Surfaces*. in *Proceedings of the 11th ACM Symposium on Computational Geometry*. 1995. ACM.
149. Humphrey, W., A. Dalke, and K. Schulten, *VMD -- Visual Molecular Dynamics*. Journal of Molecular Graphics, 1996. 14: p. 33-38.
150. Stone, J., *An Efficient Library for Parallel Ray Tracing and Animation*, 1998, Computer Science Department, University of Missouri-Rolla.
151. Sharma, R., et al., *Speech/Gesture Interface to a Visual-Computing Environment*. #IEEECGA#, 2000. 20: p. 29-37.
152. Stone, J., et al. *A System for Interactive Molecular Dynamics Simulation*. in *2001 ACM Symposium on Interactive 3D Graphics*. 2001. ACM SIGGRAPH.
153. Eargle, J., D. Wright, and Z. Luthey-Schulten, *Multiple Alignment of Protein Structures and Sequences for VMD*. Bioinformatics, 2006. 22(4): p. 504-506.
154. Berendsen, H.J.C., D. Vandespoel, and R. Vandrunen, *Gromacs - a Message-Passing Parallel Molecular-Dynamics Implementation*. Computer Physics Communications, 1995. 91(1-3): p. 43-56.
155. Hess, B., et al., *GROMACS 4: Algorithms for Highly Efficient, Load-Balanced, and Scalable Molecular Simulation*. Journal of Chemical Theory and Computation, 2008. 4(3): p. 435-447.

156. Lindahl, E., B. Hess, and D. van der Spoel, *GROMACS 3.0: a package for molecular simulation and trajectory analysis*. Journal of Molecular Modeling, 2001. **7**(8): p. 306-317.
157. Pall, S., et al., *Tackling Exascale Software Challenges in Molecular Dynamics Simulations with GROMACS*. Solving Software Challenges for Exascale, 2015. **8759**: p. 3-27.
158. Pronk, S., et al., *GROMACS 4.5: A High-Throughput and Highly Parallel Open Source Molecular Simulation Toolkit*. Bioinformatics, 2013. **29**(7): p. 845-854.
159. van der Spoel, D., et al., *GROMACS: Fast, Flexible, and Free*. Journal of Computational Chemistry, 2005. **26**(16): p. 1701-1718.
160. van Drunen, R., D. van der Spoel, and H.J.C. Berendsen, *Gromacs - a Software Package and a Parallel Computer for Molecular-Dynamics*. Abstracts of Papers of the American Chemical Society, 1995. **209**: p. 49-Comp.
161. Jorgensen, W.L., D.S. Maxwell, and J. Tirado-Rives, *Development and Testing of the OPLS All-Atom Force Field on Conformational Energetics and Properties of Organic Liquids*. Journal of the American Chemical Society, 1996. **118**(45): p. 11225-11236.
162. Mahoney, M.W. and W.L. Jorgensen, *A Five-Site Model for Liquid Water and the Reproduction of the Density Anomaly by Rigid, Nonpolarizable Potential Functions*. The Journal of Chemical Physics, 2000. **112**(20): p. 8910-8922.
163. Price, M.L.P., D. Ostrovsky, and W.L. Jorgensen, *Gas-Phase and Liquid-State Properties of Esters, Nitriles, and Nitro Compounds with the OPLS-AA Force Field*. Journal of Computational Chemistry, 2001. **22**(13): p. 1340-1352.
164. Watkins, E.K. and W.L. Jorgensen, *Perfluoroalkanes: Conformational Analysis and Liquid-State Properties from ab Initio and Monte Carlo Calculations*. The Journal of Physical Chemistry A, 2001. **105**(16): p. 4118-4125.
165. Wehling, T.O., M.I. Katsnelson, and A.I. Lichtenstein, *Adsorbates on Graphene: Impurity States and Electron Scattering*. Chemical Physics Letters, 2009. **476**(4-6): p. 125-134.
166. Ma, J., et al., *Adsorption and Diffusion of Water on Graphene from First Principles*. Physical Review B, 2011. **84**(3): p. 033402.
167. Hamada, I., *Adsorption of Water on Graphene: A van der Waals Density Functional Study*. Physical Review B, 2012. **86**(19): p. 195436.

168. Voloshina, E., et al., *On the Physisorption of Water on Graphene: A CCSD(T) Study*. Physical Chemistry Chemical Physics, 2011. **13**(25): p. 12041-12047.
169. Lohmann, T., K. von Klitzing, and J.H. Smet, *Four-Terminal Magneto-Transport in Graphene p-n Junctions Created by Spatially Selective Doping*. Nano Letters, 2009. **9**(5): p. 1973-1979.
170. Qiu, H., et al., *Hopping Transport through Defect-Induced Localized States in Molybdenum Disulfide*. Nature Communications, 2013. **4**: p. 2642.
171. Zhou, W., et al., *Intrinsic Structural Defects in Monolayer Molybdenum Disulfide*. Nano Letters, 2013. **13**(6): p. 2615-2622.
172. Yu, Z., et al., *Towards Intrinsic Charge Transport in Monolayer Molybdenum Disulfide by Defect and Interface Engineering*. Nature Communications, 2014. **5**: p. 5290.
173. Li, T.C. and S.-P. Lu, *Quantum Conductance of Graphene Nanoribbons with Edge Defects*. Physical Review B, 2008. **77**(8): p. 085408.
174. Wang, X., et al., *Room-Temperature All-Semiconducting Sub-10-nm Graphene Nanoribbon Field-Effect Transistors*. Physical Review Letters, 2008. **100**(20): p. 206803.
175. Cavallucci, T. and V. Tozzini, *Multistable Rippling of Graphene on SiC: A Density Functional Theory Study*. The Journal of Physical Chemistry C, 2016. **120**(14): p. 7670-7677.
176. Grimme, S., *Semiempirical GGA-Type Density Functional Constructed with a Long-Range Dispersion Correction*. Journal of Computational Chemistry, 2006. **27**(15): p. 1787-1799.
177. Okamoto, Y., *Density Functional Theory Calculations of Lithium Adsorption and Insertion to Defect-Free and Defective Graphene*. The Journal of Physical Chemistry C, 2016.
178. Giannozzi, P., et al., *QUANTUM ESPRESSO: A Modular and Open-Source Software Project for Quantum Simulations of Materials*. Journal of Physics: Condensed Matter, 2009. **21**(39): p. 395502.
179. Schmidt, M.W., et al., *General Atomic and Molecular Electronic Structure System*. Journal of Computational Chemistry, 1993. **14**(11): p. 1347-1363.
180. Clark, S.J., et al., *First Principles Methods Using CASTEP*. Zeitschrift für Kristallographie - Crystalline Materials, 2009. **220**(5/6): p. 567-570.



## **Vita**

Barrett Worley was born in Montgomery, Alabama in 1989. After graduating from Houston Academy in Dothan, Alabama in 2007, he attended Samford University in Birmingham, Alabama with a National Merit Scholarship. He earned a Bachelor of Science in Chemistry with a minor in Philosophy, after which, he began his doctoral work in Chemistry at The University of Texas at Austin in 2011. His doctoral research on the chemical interactions of polar molecules with graphene has been supervised by Professor Ananth Dodabalapur.

Permanent email address: [worley.barrett@gmail.com](mailto:worley.barrett@gmail.com)

This dissertation was typed by the author.